BIOMECHANICS OF DORSAL CLOSURE STUDIED USING HOLOGRAPHIC LASER MICROSURGERY

By

Aroshan Kaushalya Jayasinghe

Dissertation

Submitted to the Faculty of the

Graduate School of Vanderbilt University

in partial fulfillment of the requirements

for the degree of

DOCTOR OF PHILOSOPHY

in

Physics

December, 2012

Nashville, Tennessee

Approved

Professor M Shane Hutson

Professor Richard F Haglund, Jr.

Professor E Duco Jansen

Professor Kalman Varga

Dr. Andre Zavalin

Copyright © 2012 by Aroshan Kaushalya Jayasinghe
All Rights Reserved.

To my family,

Without whom none of this would be possible

ACKNOWLEDGEMENTS

First, and above all, I would like to thank Prof. Shane Hutson. He has been wonderful advisor and an inspirational teacher. He has taught me much about working as a researcher, both independently and as part of a varied group. Most of all he has been an inspirational example as a scientist and a teacher.

I would also like to thank the other members of my committee – Professors Richard F Haglund, Jr., E Duco Jansen, Kalman Varga, and Andre Zavalin, for their time and patient guidance. I am very grateful to Dr. Zavalin for working with me at the FEL during the early part of my time here at Vanderbilt.

I thank all my past and present friends and colleagues in the Hutson Lab – Xiaoyan Ma, Holley Lynch, David Mashburn, Sarah Crews, Ty McCleery, Monica Lacy, Tomas Yan and Jason Rohner. They have made the past few years very pleasant, with lively discussions and lots of support.

I am very grateful to Charlie Adams, Jed Zeigler, Borislav Ivanov, John Kozub, Ron Reiserer, Bob Patchin and others too numerous to mention here, for their help during my years at Vanderbilt.

Last, but not least, I thank my incredibly supportive parents and sister. They made me the person who I am today.

TABLE OF CONTENTS

Page

LIST OF TABLES

LIST OF FIGURES

CHAPTER 1

INTRODUCTION

1.1. Overview

1.1.1 Motivation and significance

Laser microsurgery is widely used for studying inter- and intra-cellular forces that drive morphogenesis. Often a single hole is "drilled" in the tissue, and the recoil and reshaping of the wound is studied [1–3]. More complex incisions are formed by ablating a sequence of points in tissue, one at a time. With this serial multi-pulse technique, only the first pulse ablates unaltered tissue; the following pulses ablate tissue retracting from the earlier ablations. For this reason, this method is not suitable for a variety of experiments, such as measuring the instantaneous retraction velocity of tissue after extended incisions, accurately isolating single cells or small patches of cells, and making multiple precise incisions on tissue under high tension. For these experiments a system capable of ablating multiple targeted points using a single laser pulse is more suitable. This dissertation describes the development of such a single-pulse, multi-point laser ablation system, and its application in studying the *in vivo* mechanics of dorsal closure in *Drosophila melanogaster* embryos.

Dorsal closure is an important morphogenetic event in the embryogenesis of *Drosophila melanogaster* and serves as a useful model system for studying wound healing, palatogenesis, and neural tube closure in vertebrates. During this stage of development, the amnioserosa – a tissue that fills a gap left in the epithelium of the embryo as a result of germband retraction – is engulfed by the surrounding lateral epidermis [4,5]. This process is driven by a number of

cooperative processes [6], the separation of which is difficult when studied from a tissue-scale perspective. By isolating single cells and studying their post-ablation dynamics, we hope to gain some insight into the forces driving this morphogenetic process. Furthermore, data gathered from these experiments can be used to inform computer models of morphogenesis.

With multiple simultaneous ablations occurring in close proximity, the interactions between ablation points is an additional important consideration [7–10]. Laser ablation of tissue is accompanied by shockwave generation and cavitation with possible subsequent jet formation [11–14]. In most cases, these secondary effects may be safely ignored as they occur on smaller length and time scales compared to the biological processes under study, but the action of multiple cavitation bubbles and shockwaves can have unexpected and noticeable effects. In a few cases, it may be possible to utilize these interactions to maximize "cutting" efficiency [15], but in general these secondary effects are hard to predict, and need to be minimized. To study the effects of cavitation in tissue, we built a high-speed bright-field imaging system, capable of taking images of bubbles in tissue with exposure times as short as 15 ns. This system was attached to a confocal microscope along with the multi-point ablation system.

1.1.2 Outline

This dissertation is based upon experimental techniques and data published or prepared for publication in peer-reviewed journals.

Chapter 1 is a brief review of the physical and biological processes dealt with in this research project.

Chapter 2 details the methods and equipment used in data collection and analysis, including experimental layouts, software design, and sample preparation.

Chapter 3 is summary of the multi-point ablation technique and includes preliminary data and notes on the performance of the system. This manuscript was published in *Biomedical Optics Express* [16].

Chapter 4 deals with an application of the ablation system, namely the study of isolated amnioserosa cells *in vivo*. This work, which has been prepared for submission, looks at the dynamics of single cells post-isolation and compares two possible two-dimensional computer models for simulating the dynamics of the amnioserosa tissue.

Chapter 5 looks at the secondary effects of laser ablation in tissue, and considers the limitations they impose on the multi-point ablation system.

Chapter 6 provides a summary of the work done and considers some possible future directions.

1.2 Background

1.2.1 Laser-tissue interaction

Laser surgery has been an active area of research for several decades, both as a clinical and as a research tool [17–20]. Research into laser ablation of biological tissues started in the 1960s, soon after the development of the first ruby laser [17]. The promise of better surgical and medical techniques attracted many researchers into this field, and by the 1980s the use of lasers in medicine and surgery was widespread. The mechanisms of laser ablation and methods to reduce collateral damage remain important areas of research to this day.

Early work in laser surgery and microsurgery was done using both continuous wave (CW) and pulsed lasers operating in the visible spectral range. Pulsed lasers have been used successfully in medicine from the start ,and particularly since the mid-1980s, have become widespread in biophysical research [1,2,5,6,18,19,21,22]. Pulsed lasers create very high energy densities for short periods of time, resulting in ablation and vaporization of a region of tissue while minimizing thermal damage to the surrounding material, making these the instruments of choice for many surgical applications.

Pulsed lasers, with pulse durations in the femtosecond to nanosecond range, are widely used for probing tissue mechanics [1,2,5,6,21–23]. These lasers can be used to precisely ablate cellular and sub-cellular structures *in vivo* and *in vitro*, as well as other tasks that may be difficult to accomplish using mechanical probes. Higher-powered lasers operating in the mid-IR (λ = 2-9 μm) spectral range have shown promise as surgical tools [24–27]; lasers operating at these wavelengths avoid some of the medical side effects associated with UV exposure and have a useful penetration depth in tissue.

1.2.1.1 Chromophores

Understanding the mechanisms by which energy is absorbed by tissue is important for selecting the proper laser for a specific application. Different components of the irradiated tissue absorb energy at different wavelengths. In most cases, a laser is chosen such that the biological system of interest has a high absorption coefficient at the laser's wavelength. Often more than one chromophore is excited at any given wavelength and complementary or competitive physical processes can occur. In addition, physical changes in the system during the ablation process can dynamically change the chromophores' absorption coefficient.

Proteins and water are the main chromophores at infrared wavelengths (Figure 1.1). Vibrational modes in these molecules absorb energy at many wavelengths in this spectral region. Melanin, a pigment found in tissues like skin and hair, is an important chromophore for wavelengths in the visible and ultraviolet ranges. Hemoglobin is another significant chromophore, particularly at the violet end of the visible spectrum.

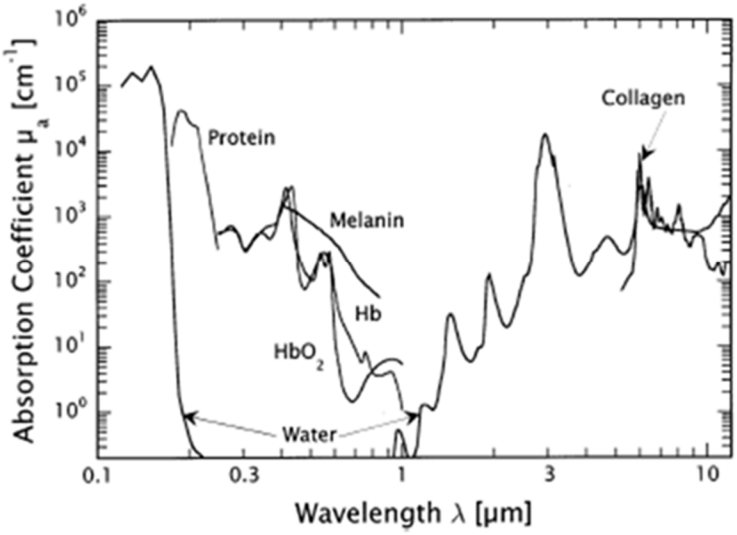

Figure 1.1: Optical absorption coefficient for different biological chromophores. (Reproduced from [28]).

In the ultraviolet spectral range (λ = 150~400nm) energy absorption is often due to excitation of electronic states leading to plasma formation and photo-decomposition [18]. Proteins, melanin, and DNA all absorb energy in this range. Water is also a good chromophore at far UV (λ < 170 nm) wavelengths, with an absorption coefficient an order of magnitude greater than that of proteins.

1.2.1.2 Plasma formation

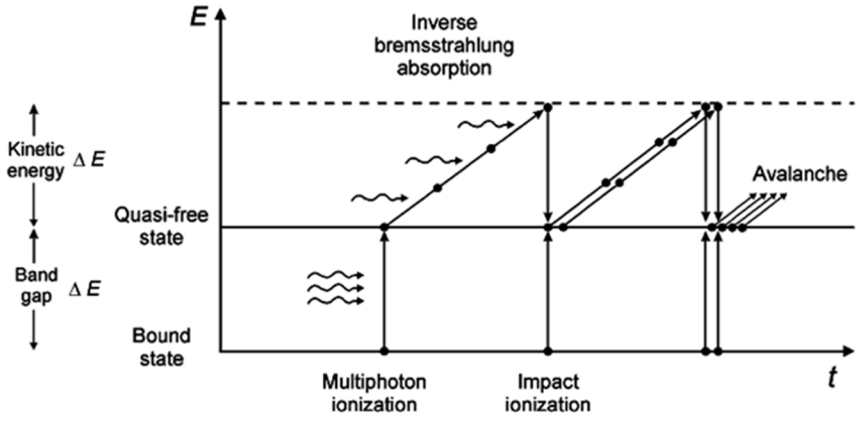

Figure 1.2: Energy level diagram of multi-photon and avalanche/cascade ionization. A high energy electron creates another quasi-free electron by impact ionization. Avalanche refers to the rapid increase in the number of electrons as two electrons are left after each impact ionization event. (Reproduced from [28]).

The energy level diagram presented above shows how energy is absorbed in the linear, low-intensity regime. At higher intensities, energy absorption is largely due to laser induced plasma formation or optical breakdown inside the biological tissue [29,30]. Laser beams with high fluence can create quasi-free electrons in the medium through thermionic and/or multi-photon processes. These quasi-free electrons can gain energy from the electric field and transfer energy to surrounding molecules, creating a cascade of quasi-free electrons (Figure 1.2), rapidly ionizing a region of tissue. In material which is transparent at the incident laser wavelength, optical breakdown is the dominant mechanism for energy absorption and subsequent ablation.

The laser-induced plasma has a number of effects over different time and length scales. Initially the high temperature plasma vaporizes material in its immediate vicinity. This volume containing high-pressure vapor and energetic ions expands explosively, generating a pressure wave and forming a cavitation bubble [28,29]. This bubble can oscillate several times, with each compression of the bubble possibly resulting in new pressure waves [8], and jet formation. The mechanical stresses (cavitation, pressure wave and jet formation) last far longer and affect a greater volume than the original laser pulse or plasma. Figure 1.3 shows the approximate time scales during which the different processes and effects of ablation may be active. The actual duration of these effects are energy dependent.

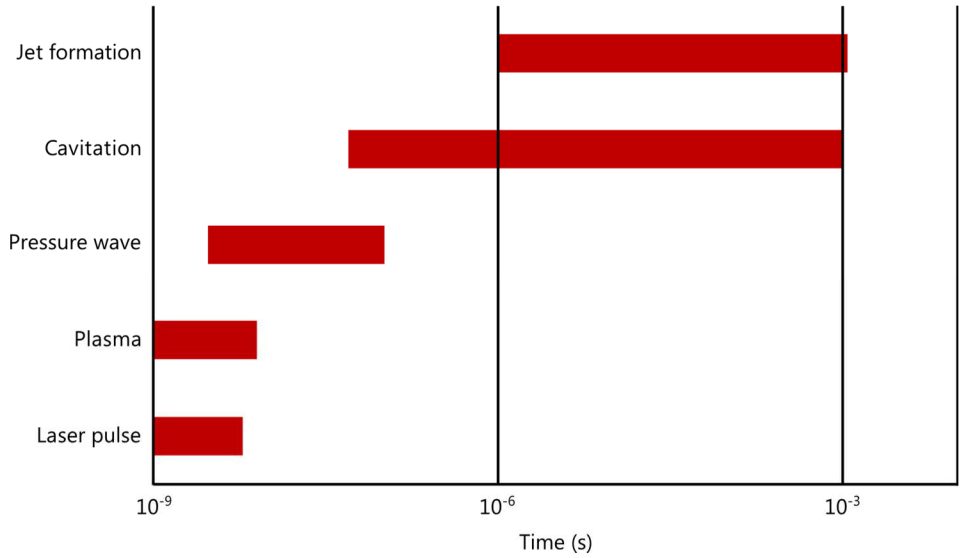

Figure 1.3: Approximate time scales of the different processes involved in laser ablation within a transparent material. A nanosecond laser pulse is assumed. A jet may not always be present.

Plasma formation can be both a boon and a hindrance to ablation. As most of the beam energy is absorbed in the plasma, high energy densities can be achieved, even in transparent material. Therefore, precise removal of tissue from a surface is possible with carefully chosen laser parameters [31]. The opaque plasma can be a problem as it effectively shields tissue beyond it from the ablating laser pulse, and can thus reduce ablation depth. Furthermore, high energy

plasmas can cause shockwave and cavitation bubble formation, which in turn can result in collateral damage over large areas of tissue.

Optical breakdown initiates at points along the laser beam where the energy density exceeds the required threshold. This can be quite deep within the bulk for transparent materials, rather than at the surface as in materials with larger absorption coefficients. Plasma is formed initially at the focus of the beam, and as the intensity of the pulse increases toward its maximum, material in front of the focal volume (closer to the laser) may be ionized as well (Figure 1.4a) [28,31].

The shape of the plasma depends on the duration, energy, and focusing angle of the laser pulse [32]. The focusing angle helps determine the shape of the focal volume, and how the energy density varies along the beam path (Figure 1.4b). Higher energies and longer pulse durations will result in larger plasmas. For nanosecond pulses, thermionic emission of quasi-free electrons, and hence plasma formation, occurs within most of the cross-section of the beam (Figure 1.4c) close to the focal plane. This relatively large plasma enables the single-pulse ablation of cellular and multi-cellular biological structures [1,2,14,22].

Multi-photon ionization, the dominant mechanism for optical breakdown at the near-infrared wavelengths used in picosecond and femtosecond lasers, is only significant close to the axis of the Gaussian laser beam and the plasma created tends to be elongated with smaller cross-section than the incident laser beam (Figure 1.4d). For this reason, femtosecond lasers are ideal for performing sub-cellular surgery [23,33,34], but need multiple pulses to ablate larger structures such as a cell wall.

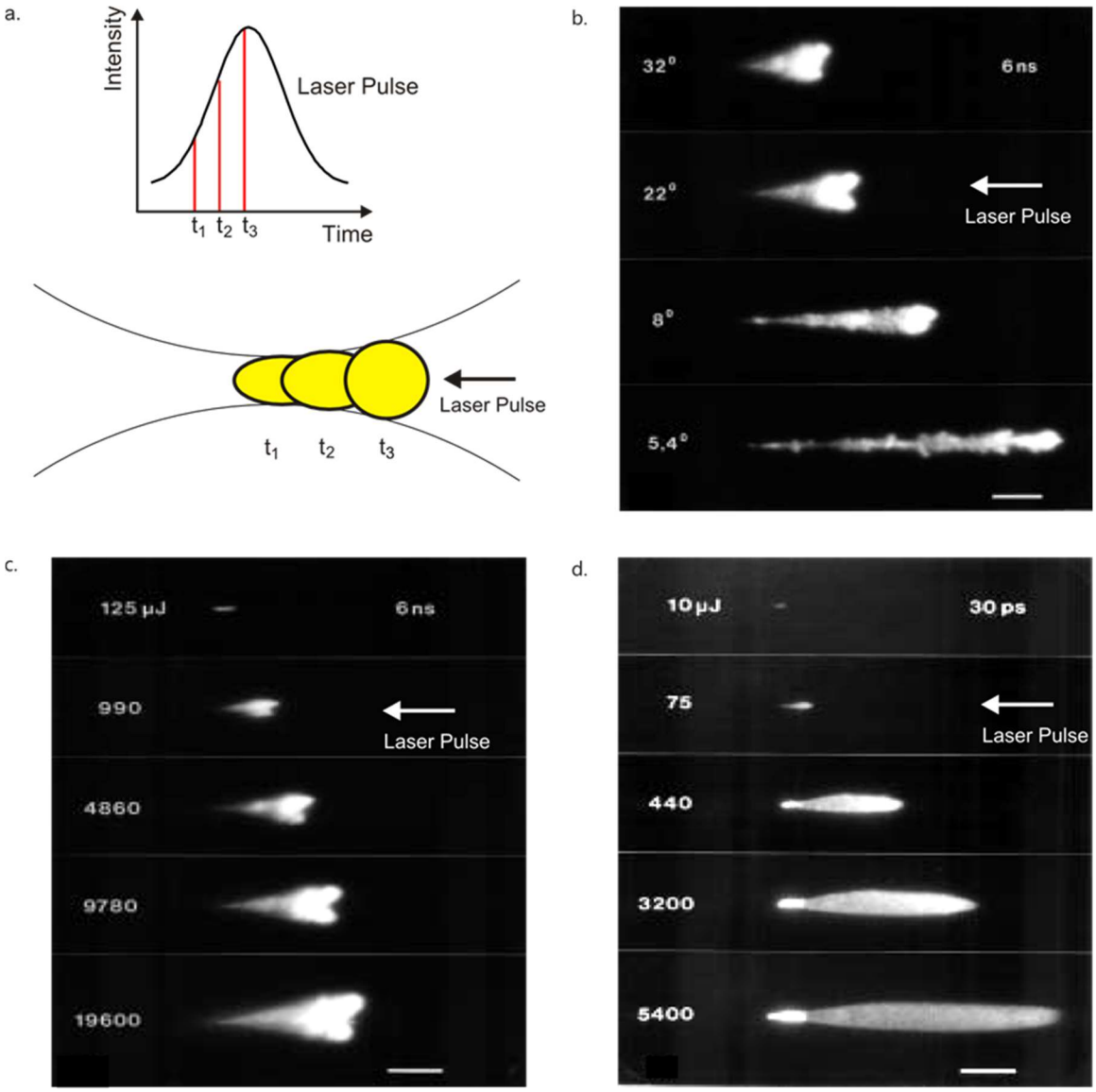

Figure 1.4: The variation in the shape of plasmas resulting from different laser parameters. **a.** Schematic of plasma shape change during ablation. As the pulse intensity increases from t_1 to t_3 the plasma moves towards the laser and increases in volume. **b.** Plasma shape changes with focusing angle. The pulse is incident from the right with 6-ns duration and 10-mJ energy. Variation in shape and size for **c.** 6-ns and **d.** 30-ps pulses at different pulse energies. The scale bar in b, c and d represent a length of 100 µm. (Photographs reproduced from [32].)

1.2.1.3 Wavelength selection

The wavelength of the ablating laser plays an important part in the formation and the energy density of plasmas. The rate of multi-photon ionization and the rate of cascade ionization increase with decreasing wavelength. This is because fewer photons are required to reach the ionization energy.

The absorption of the plasma varies with wavelength as well. The plasma absorption coefficient, α_{pl}, is given by

$$\alpha_{pl} = \frac{\nu_{ei}}{nc}\frac{\omega_{pl}^2}{\omega^2 + \nu_{ei}^2} \quad ; \quad \text{with } \omega_{pl}^2 = \frac{Ne^2}{\varepsilon_0 m_e} \tag{1.1}$$

where ω is the angular frequency of the incident electromagnetic field, ω_{pl} is the plasma frequency, e is the charge of an electron, N is the free electron density, ν_{ei} is the mean collision rate of the free electrons and ions, n is the index of refraction [31].

If $\nu_{ei} \ll \omega$ (cold laser plasma, *i.e.*, the energy deposited by the electric field is not thermalized by collisions), α_{pl} simplifies to

$$\alpha_{pl} = \frac{\nu_{ei}}{nc}\frac{\omega_{pl}^2}{\omega^2} \propto \frac{N^2}{\omega^2} \tag{1.2}$$

as both ν_{ei} and ω_{pl}^2 are proportional to N. As UV radiation is more efficient at creating free electrons (and thus increasing N), the absorption of plasmas created by UV lasers increases rapidly until $\omega_{pl}^2 = \omega$ and a critical electron density is reached. At this point the plasma stops absorbing and only scattering is left. Longer wavelengths (with smaller ω) require higher irradiances to generate plasma, but for a given α_{pl} these lasers are better at injecting energy into the plasma. Plasmas created at these wavelengths are larger and have higher energy densities than those created at shorter wavelengths.

Venugopalan *et al.* [30] compared plasmas created in water at wavelengths of 532 nm and 1064 nm (Table 1.1), and found that both the irradiance required for optical breakdown, and the size of the plasma was significantly greater at the longer wavelength.

Table 1.1: Required pulse energy and plasma dimension variation with wavelength. (Data from [30]).

Wavelength λ (nm)	Normalized pulse energy $\beta = (E_P/E_{TH})$	Pulse energy E_P (μJ)	Plasma length (μm)	Plasma diameter (μm)	Plasma volume (μm)
1064	1	18.0 ± 0.1	14.0	8.9	581
1064	2	36.4 ± 0.2	25.0	15.5	3140
1064	5	90.9 ± 0.3	37.9	21.0	8750
1064	10	182.2 ± 0.9	47.3	27.5	18700
532	1	1.89 ± 0.10	3.6	2.3	9.97
532	2	3.78 ± 0.13	3.8	2.9	16.7
532	5	9.19 ± 0.30	8.4	5.1	114
532	10	19.15 ± 0.60	12.6	7.6	381

1.2.2 Secondary effects of plasma formation

A laser-generated plasma will expand out of its initial volume for a number of reasons. First, UV radiation emitted from the plasma can ionize the surrounding material, increasing the size of the plasma. Second, superheated material will expand beyond the laser beam path. Finally, free electrons will diffuse away from the plasma carrying energy into the surrounding material. Unlike ablation at a surface, plasma created inside a material remains confined to a small region, and heat diffusing from the plasma and the expansion of the plasma create large mechanical and thermal stresses in the surrounding material. The resulting pressure waves and cavitation bubbles cause collateral damage over a volume much larger than the original plasma.

1.2.2.1 Pressure waves

The temperature of a laser-induced plasma will quickly rise to ~10^4 K as it absorbs energy from the incident laser beam [32]. High kinetic energy electrons contained in the plasma diffuse out of the initial volume, followed shortly by the more massive ions. This movement of mass creates a shockwave which expands outwards from the ablation point [31]. The wave initially has a hypersonic velocity of up to 5000 m/s and carries away a significant fraction of the energy contained in the plasma. The energy of the shockwave dissipates as it expands, and it eventually slows down to the speed of sound in the material. Although the wave is properly referred to as a shockwave only at hypersonic velocities, it is often referred to interchangeably as a pressure wave or shockwave in the far field.

Vogel and Busch reported extensively on shockwave generation for picosecond and nanosecond pulses [11]. They showed that the delay between plasma formation and shockwave formation depends on the pulse width of the incident beam, with shockwaves forming 100 ps and 6 ns after the start of the ablating pulse, for 30-ps and 6-ns pulsewidths respectively.

Quick passage of the pressure wave through a targeted material means that actual displacement of material is small and damage is usually slight at distances away from the ablation site; however, the rarefaction wave created when a pressure wave intersects a free surface can cause cavitation over longer distances [35].

Venugopalan *et al.* [30] measured pressure as a function of time for a 6 ns pulse from a Nd:YAG laser at both 532-nm and 1064-nm wavelengths. They showed that at threshold energies, the pressure wave energy is higher at λ = 1064 nm, but a larger percentage of the pulse energy is taken up by the wave at λ = 532 nm. This is consistent with the data presented earlier (Table 1.1) showing that greater irradiances are needed for creating plasmas using longer wavelengths. At higher pulse energies, shockwave pressure, measured at a given distance, was higher but dropped away rapidly (Figure 1.5a), and the shockwave width remained small even for large energies (Figure 1.5b). The inset in Figure 1.5a shows a side view of plasma, which appears elongated from this perspective.

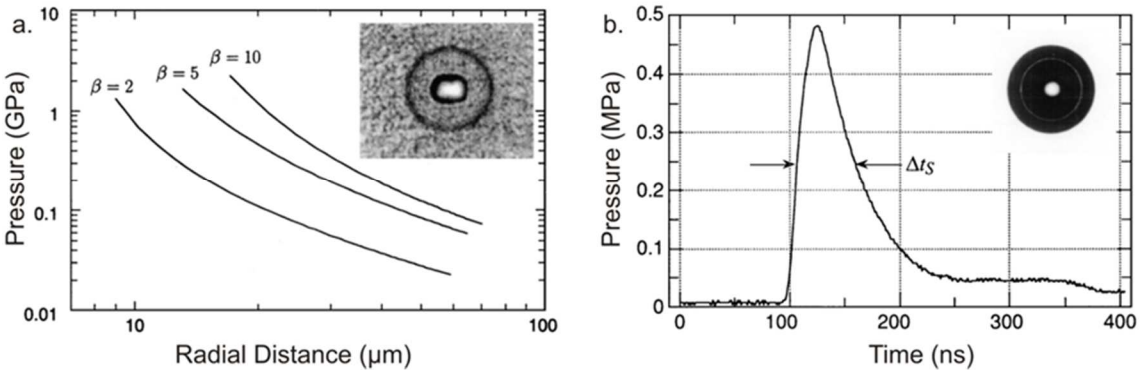

Figure 1.5: Pulse-energy dependence of pressure waves. **a.** Shockwave pressure vs. propagation distance generated by 1064-nm irradiation for pulse energies 2×, 5×, and 10× threshold. Inset: plasma, shockwave, and cavitation bubble photographed 30-ns after delivery of a 1064 nm pump pulse at 10× threshold energy. **b.** Temporal profile of shockwave pressure generated by 1064-nm irradiation at 5× threshold energy measured 10 mm from the optical breakdown site. Inset: 720-μm diameter cavitation bubble formed by a 1064 nm pump pulse at 5× threshold energy. (Reproduced from [30].)

1.2.2.2 Cavitation bubbles and jet formation.

The high temperatures and mechanical stresses caused by a laser-induced plasma can result in cavitation bubbles being formed inside the material. Although distinction is usually made between "cavitation", which is caused by mechanical rupture of material, and "boiling" which is due to high temperatures, it is not possible to distinguish between the two for bubbles formed by a plasma as both the required temperature and mechanical stresses are often present [28].

A portion of the energy (as much as 25%) contained in a plasma is transferred to the cavitation bubble [11,12]. As plasmas created by long wavelength lasers have more energy, the resulting cavitation bubbles can cause a lot more damage. Hutson and Ma [14] compared the tissue damage caused by lasers with wavelengths of 355 nm (Figure 1.6a) and 532 nm (Figure 1.6b) and found that collateral damage increased significantly at the longer wavelength. The pulse duration is also a factor in the efficiency of energy transfer from the plasma to the bubble. Cavitation bubbles formed by picosecond and femtosecond pulses consume a smaller fraction of the pulse energy [28], as compared to nanosecond and longer pulses. This can be explained by the lower plasma energy density for these pulses and a larger fraction being used for vaporization.

The energy imparted to the bubble by the plasma drives the bubble wall outwards. As the bubble expands, its internal pressure drops below that of the surrounding fluid [36]. Within a millisecond, the bubble implodes, succumbing to the difference between internal and external pressures [31]. This implosion compresses the vapor and gasses contained inside the bubble, generating a second pressure wave. The increase in pressure and temperature of the compressed vapor can

lead to a second expansion of the bubble. In this way, the bubble radius can oscillate several times until the energy contained in the bubble is dissipated, and the vapor reabsorbed by the surrounding fluid.

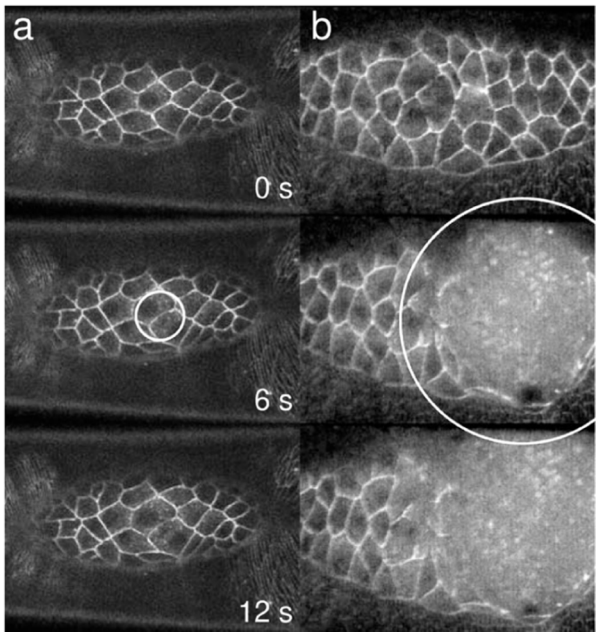

Figure 1.6: Three sequential confocal images of fruit fly embryos before and after ablation. **a.** λ = 355 nm and E_P = 1.22 μJ (5× threshold). **b.** λ = 532 nm and E_P = 8.26 μJ (1× threshold). Ablation occurred between the first two images. Each white circle is centered on the ablation site with a radius equal to the calculated R_{max} = 12.9 μm in *a* and 65.6 μm in *b*. (Reproduced from [14]).

The large bubble can damage material in a wide area and on relatively long time scales. The maximum bubble radius depends on the mechanical strength of the tissue. Hutson and Ma [14] demonstrated that for a given set of pulse parameters, cavitation bubbles formed *in vivo* are much smaller and have shorter oscillation periods than bubbles created in water, suggesting that the biological matrix constrains the growth of these bubbles. Therefore, the damage caused in tissue by cavitation is significantly less than what might be expected from studies of bubbles in water. Despite this difference, studying cavitation in liquids is useful for understanding the behavior of bubbles formed in tissue. Venugopalan *et al.* [30] measured shockwave and cavitation

bubble energies created in water at wavelengths of 532 nm and 1064 nm. The data from that paper is reproduced below (Table 1.2).

Table 1.2: Shockwave and cavitation bubble dynamics parameters in water for 532-nm and 1064-nm irradiation. These include the pump pulse energy (EP), shockwave energy measured 10 mm from the optical breakdown site (ES), cavitation bubble oscillation period (T_{osc}), maximum bubble radius (R_{max}), and bubble energy (EB). (Data from [30]).

λ (nm)	β = (E_P/E_{TH})	E_P (μJ)	E_S (μJ)	E_S/E_P (%)	T_{osc} (μs)	R_{max} (μm)	E_B (μJ)	E_B/E_P (%)
1064	1	18.0 ± 0.1	0.64	3.6	27.7	151.3	1.45	9.1
1064	2	36.4 ± 0.2	2.33	6.4	45.3	247.6	6.35	17.3
1064	5	90.9 ± 0.3	7.32	8.1	65.9	360.1	19.57	21.5
1064	10	182.2 ± 0.9	15.69	8.6	86.6	473.3	44.41	24.4
532	1	1.89 ± 0.10	.023	1.2	8.3	45.4	0.039	2.1
532	2	3.78 ± 0.13	.157	4.2	13.8	75.4	0.180	4.2
532	5	9.19 ± 0.30	.90	9.8	26.9	147.0	1.33	14.3
532	10	19.15 ± 0.60	2.53	13.2	37.5	205.0	3.60	19.3

Lord Rayleigh in 1917 modeled the collapse of a spherical bubble in an infinite incompressible liquid [37]. This model is also applicable for cavitation bubbles [7,11,31]. The energy contained in the bubble is equal to its potential energy at its maximum expansion. The maximum potential energy of the bubble is equal to its maximum volume times the pressure difference between the contents of the bubble and the exterior liquid,

$$E_B = \frac{4}{3}\pi\left(p_0 - p_{vap}\right)R_{max}^3 \tag{1.3}$$

where p_0 is the hydrostatic pressure of the liquid and p_{vap} is the vapor pressure inside the bubble. The relationship between the bubble oscillation time, T_{osc}, and maximum radius, R_{max}, is given by;

$$R_{max} = \frac{T_{osc}}{1.83\sqrt{\rho/(p_0 - p_{vap})}} \tag{1.4}$$

where ρ is the density of the liquid.

Using these formulae, we can infer the maximum radius and energy of a cavitation bubble from its oscillation period, using hydrophone measurements of pressure waves generated during plasma formation and bubble collapse [14,35]. The Rayleigh formula is valid for large bubbles in a spherically symmetric fluid, for which effects of surface tension may be safely ignored. Although it is less accurate for describing the dynamics of small bubbles created in vivo - because surface tension becomes important for bubbles with small radii and embryonic tissue lacks spherical symmetry - it still provides reasonable estimates of maximum bubble radius based on bubble lifetime [14].

The bubble may collapse and rebound several times. Bubbles formed in water lose over 80% of their initial energy during the first cycle [31], and subsequent bubbles are of much smaller radius (Figure 1.7a). Pressure waves are radiated upon each collapse (Figure 1.7b). In higher viscosity material, for example, silicone oil, bubbles may rebound several times [38] (Figure 1.7c).

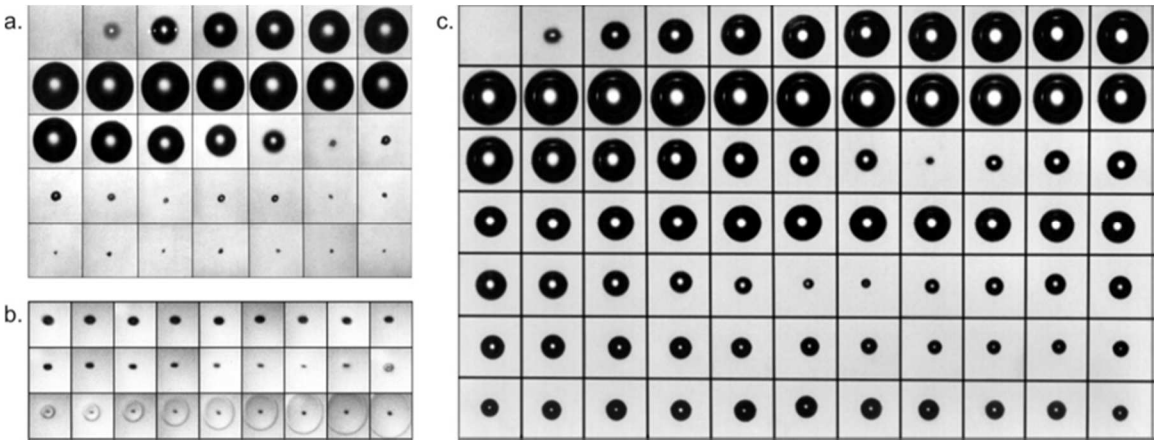

Figure 1.7: Cavitation bubble oscillation and collapse. **a.** Dynamics of a laser-produced spherical bubble in water observed at 75,000 frames per second (fps). Maximum bubble radius is ~1.3 mm. **b.** Collapse of a laser-produced spherical bubble in water observed at 20.8 million fps (48 ns inter-frame time). The size of each individual image is 1.5×1.8 mm. **c.** Cavitation bubble in silicone oil (viscosity = 0.485 Pa·s) observed at 75,000 fps. Maximum bubble radius is ~2 mm. (Reproduced from [38].)

Cavitation bubble oscillation requires spherical symmetry. Any asymmetry in the pressure of the fluid surrounding the bubble will cause the bubble to collapse in such way that a jet is formed. In the case of a bubble formed close to a rigid wall, the fluid pressure between the bubble and the wall will be reduced slightly during bubble collapse. This will slow down the collapse of the bubble wall closest to the rigid boundary. The difference in velocity between the bubble walls closest to and furthest away from the rigid boundary will result in a jet towards the boundary (Figure 1.8).

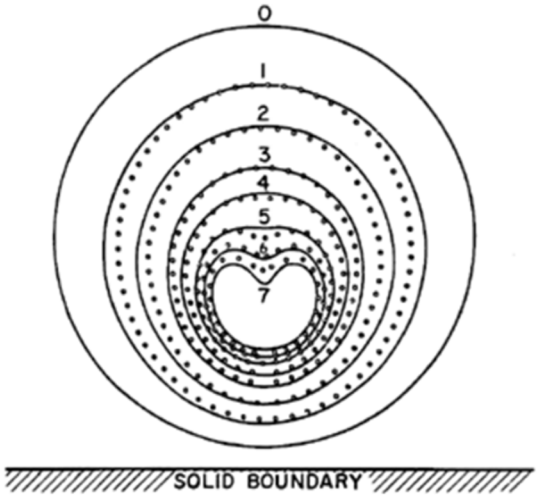

Figure 1.8: The collapse of a cavitation bubble close to a solid boundary. The theoretical shape is represented by the solid lines and the points show experimental curves. (Reproduced from [7].)

If the bubble is formed within a few mm of an elastic boundary, a second jet may be created going away from the boundary [5,8,11]. The elastic boundary, *e.g.*, a cell wall in tissue, would be deformed during bubble expansion and will rebound during bubble collapse. This increases the pressure between the bubble and the boundary and creates a jet away from the boundary [8].

If two bubbles are formed in close proximity, each will form a jet towards the other [38]. The pressure in the fluid between pairs of bubbles is reduced during bubble collapse. This reduction in

pressure on one side of each bubble produces jets much like those formed between bubbles and rigid boundaries (Figure 1.9).

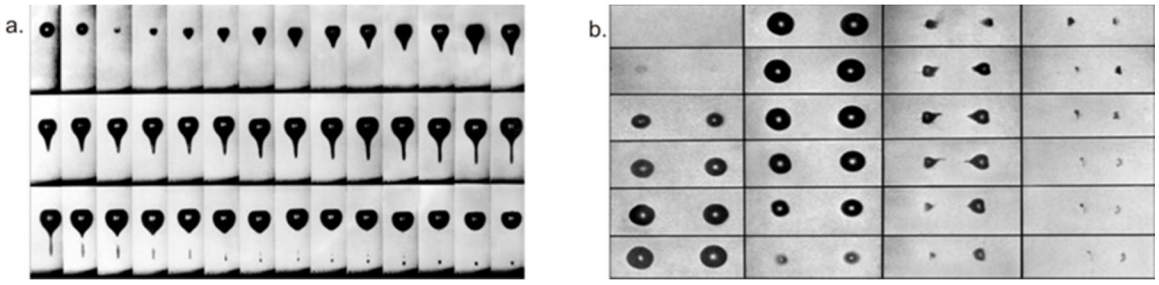

Figure 1.9: Jet formation. **a.** Dynamics of a laser-produced spherical bubble in water of reduced surface tension in the neighborhood of a plane solid boundary observed at 300,000 fps. Each individual frame is 2.7×6.7 mm in size. **b.** Jet formation upon interaction of two laser-produced cavitation bubbles observed at 58,000 fps. The initial bubble distance is 3.6 mm. Frame size is 7mm×3mm. (Reproduced from [38].)

1.2.2.3 Interaction between ablation points

When multiple, simultaneous ablation events occur in close proximity to each other, the cavitation bubbles and pressure waves can interact with effects that are difficult to extrapolate from studying a single ablation. Toytman *et al.* demonstrated, using a collagen analogue, that precisely positioned pairs of ablation points can enhance the cutting efficiency for laser surgery beyond that of a serial single-point ablation system [15]. This relies on jets formed during bubble collapse "cracking" the material between the ablation points; however, in the dynamic environment of living tissue, with multiple elastic membranes in the vicinity of the cavitation bubbles, it would be difficult to predict the behavior of any jets formed.

Another possible effect is the formation of secondary cavitation bubbles some distance away from the ablation point. If the interactions between multiple pressure waves (acoustic diffraction), or between pressure waves and a free surface or other cavitation bubbles have created multiple rarefaction (or tensile) waves that intersect, the pressure at these intersections may drop

sufficiently to form new voids (cavitation bubbles) (Figure 1.10) [9,35,39]. In addition, the interaction between a laser-generated cavitation bubble and a pressure wave can result in deformation of the bubble and a change in lifetime [40].

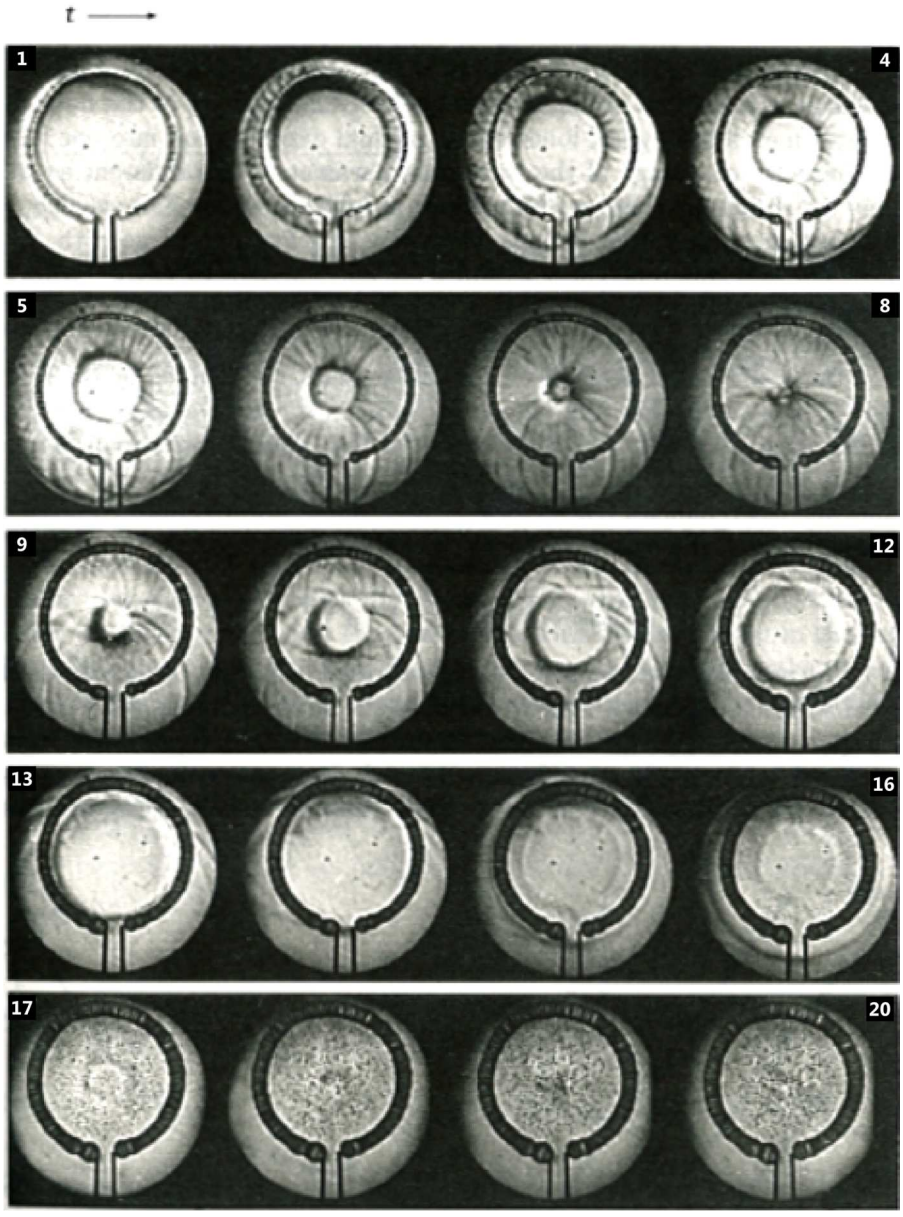

Figure 1.10: Secondary cavitation caused by a converging rarefaction wave. In this experiment the explosion of a conductor creates a ring of cavitation bubbles. The advancing pressure wave can be seen in frames 1-12. A cloud of new cavitation bubbles is visible in frames 17-20. (Reproduced from [9].)

1.2.3 Dorsal closure in Drosophila melanogaster

Dorsal closure (DC) is an important morphogenetic process that starts approximately ten hours into the 22- to 24-hour long embryogenesis of *Drosophila* and takes about two hours to complete [4,5,22,41,42]. During DC, the amnioserosa (AS), an extraembryonic epithelium, is engulfed by the lateral epidermis (LE) (Figure 1.11). This process is of wide interest for a number reasons, including its similarity to wound healing [43,44], the number of biological processes involved [6], and its robustness [45,46].

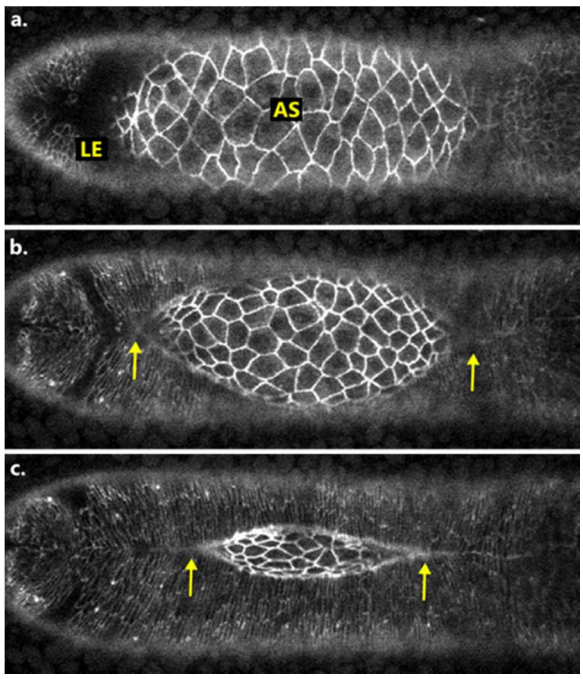

Figure 1.11: Confocal images of the amnioserosa during dorsal closure. **a.** Early, **b.** mid and **c.** late dorsal closure. The amnioserosa and lateral epidermis tissue sheets are labeled in a. The arrows in b. and c. point to the canthi. The "seam" as the two epidermal sheets merge can be seen in c.

In early DC, the boundary between AS and LE cells is scalloped and disorganized (Figure 1.12a-b). At this stage, the AS cells are large and irregular and undergo periodic contractions of their apical surface area. By mid DC, the outer boundary is better defined and significantly smoother with a supracellular actin cable along the boundary [5]. The AS cells are on average smaller and are more

regular in shape than at earlier stages of development (Figure 1.12c-d). The AS tissue is eye-shaped, with canthi at the anterior and posterior ends. The advancing LE meet at the canthi and fuse along the midline of the dorsal side of the embryo. Towards the end of DC, the pulsations in individual AS cells cease in an ordered manner, with cells closer to the boundary "freezing" in their pulsation cycle first.

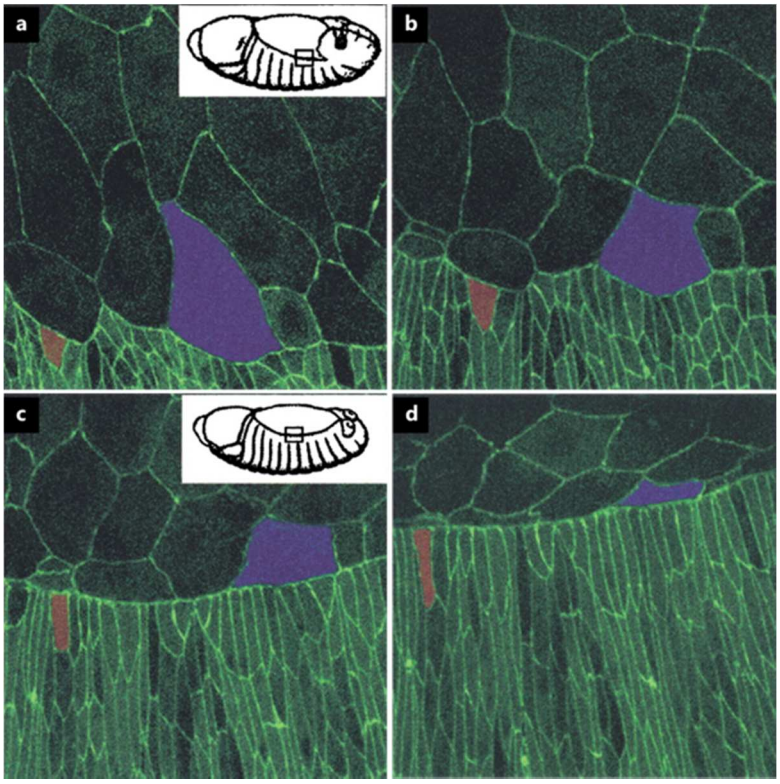

Figure 1.12: The smoothness of the boundary between the amnioserosa and lateral epidermis increases with time. An AS cell is shown filled in purple, and a LE cell in red. The insets show the overall shape of amniosera tissue, and the approximate position of the scan within the tissue. (Reproduced from [5].)

The presence of a reasonably intact AS tissue is necessary for DC to succeed [47]. The process will proceed, albeit slowly, if the AS is damaged. The contraction cycle of the AS cells may play an important part in shrinking the area of tissue, by allowing the surrounding purse string to decrease its circumference without an excessive amount of tension [3]. Tension on the actin purse string does provide a significant fraction of the force required to maintain a uniform advance of

the leading edge of the LE [1,48,49]. The combination of pulsed contraction in the apical area of AS cells, elongation of lateral epidermal cells, "zippering" at the canthi, and tension in the "purse string" actin cable combine to drive dorsal closure with surprising robustness [1,5,42,48,49].

The interplay of different biomechanical processes involved in dorsal closure, as well as the large, thin, and countably few cells comprising the AS tissue, make it an attractive candidate system for computational modeling [3,45]. These models can then be tested by introducing either genetic [5,46,50] or physical perturbations [1,6,45]. It is difficult to isolate different mechanisms from each other and from the side effects of the introduced perturbation to obtain absolute values for physical parameters in the models. Nonetheless, we can infer some necessary minimum attributes for dorsal closure, as well as the relative strengths of different processes and parameters.

1.3 References

[1] M. S. Hutson, Y. Tokutake, M. S. Chang, J. W. Bloor, S. Venakides, D. P. Kiehart, and G. S. Edwards, Science **300**, 145 (2003).
[2] X. Ma, H. E. Lynch, P. C. Scully, and M. S. Hutson, Phys. Biol. **6**, 036004 (2009).
[3] J. Solon, A. Kaya-Çopur, J. Colombelli, and D. Brunner, Cell **137**, 1331 (2009).
[4] J. Campos-Ortega and V. Hartenstein, *The Embryonic Development of Drosophila Melanogaster*, 2nd ed. (Springer, 1997).
[5] A. Jacinto, S. Woolner, and P. Martin, Developmental Cell **3**, 9 (2002).
[6] D. P. Kiehart, The Journal of Cell Biology **149**, 471 (2000).
[7] C. E. Brennen, *Cavitation and bubble dynamics* (Oxford University Press, New York, 1995).
[8] E. A. Brujan, K. Nahen, P. Schmidt, and A. Vogel, Journal of Fluid Mechanics **433**, 251–282 (2001).
[9] V. Kedrinskii, *Hydrodynamics of Explosions. Experiments and Models* (Springer, Berlin;Heidelberg;New York, 2005).
[10] K. Y. Lim, P. A. Quinto-Su, E. Klaseboer, B. C. Khoo, V. Venugopalan, and C.-D. Ohl, Phys. Rev. E **81**, (2010).
[11] A. Vogel, S. Busch, and U. Parlitz, The Journal of the Acoustical Society of America **100**, 148 (1996).
[12] A. Vogel, R. Engelhardt, U. Behnle, and U. Parlitz, Applied Physics B Lasers and Optics **62**, 173 (1996).
[13] T. Kodama and Y. Tomita, Applied Physics B: Lasers and Optics **70**, 139 (2000).
[14] M. S. Hutson and X. Ma, Phys. Rev. Lett. **99**, 158104 (2007).
[15] I. Toytman, A. Silbergleit, D. Simanovski, and D. Palanker, Phys. Rev. E **82**, (2010).
[16] A. K. Jayasinghe, J. Rohner, and M. S. Hutson, Biomedical Optics Express **2**, 2590 (2011).
[17] L. R. Solon, R. Aronson, and G. Gould, Science **134**, 1506 (1961).
[18] R. Srinivasan, Science **234**, 559 (1986).
[19] S. L. Trokel, R. Srinivasan, and B. Braren, Am. J. Ophthalmol. **96**, 710 (1983).
[20] M. M. Zaret, G. M. Breinin, H. Schmidt, H. Ripps, I. M. Siegel, and L. R. Solon, Science **134**, 1525 (1961).
[21] M. W. Berns, J. Aist, J. Edwards, K. Strahs, J. Girton, P. McNeill, J. B. Rattner, M. Kitzes, M. Hammer-Wilson, L. H. Liaw, A. Siemens, M. Koonce, S. Peterson, S. Brenner, J. Burt, R. Walter, P. J. Bryant, D. van Dyk, J. Coulombe, T. Cahill, and G. S. Berns, Science **213**, 505 (1981).
[22] D. P. Kiehart, Y. Tokutake, M. S. Chang, M. S. Hutson, J. Wiemann, X. G. Peralta, Y. Toyama, A. R. Wells, A. Rodriguez, and G. S. Edwards, in *Cell Biology: A Laboratory Handbook*, edited by J. E. Celis, 3rd ed. (Elsevier Academic, 2006), pp. 87–103.
[23] A. Vogel, J. Noack, G. Hüttman, and G. Paltauf, Appl. Phys. B **81**, 1015 (2005).
[24] G. Edwards, R. Logan, M. Copeland, L. Reinisch, J. Davidson, B. Johnson, R. Maciunas, M. Mendenhall, R. Ossoff, and J. Tribble, Nature **371**, 416 (1994).
[25] G. S. Edwards, Laser & Photonics Review **3**, 545 (2009).
[26] K. M. Joos, in (SPIE, 1996), pp. 89–92.
[27] V. A. Serebryakov, é. V. Boĭko, N. N. Petrishchev, and A. V. Yan, Journal of Optical Technology **77**, 6 (2010).
[28] J. Noack and A. Vogel, IEEE Journal of Quantum Electronics **35**, 1156 (1999).
[29] V. Venugopalan, A. Guerra, K. Nahen, and A. Vogel, Phys. Rev. Lett. **88**, (2002).
[30] A. Vogel and V. Venugopalan, Chem. Rev. **103**, 577 (2003).

[31] M. H. Niemz, *Laser tissue interactions : fundamentals and applications ; with 33 tables, 40 problems and solutions* (Springer, Berlin [u.a.], 2007).
[32] A. Vogel, K. Nahen, D. Theisen, and J. Noack, IEEE Journal of Selected Topics in Quantum Electronics **2**, 847 (1996).
[33] J. Colombelli, S. W. Grill, and E. H. K. Stelzer, Rev. Sci. Instrum. **75**, 472 (2004).
[34] J. Colombelli and J. Solon, Cell and Tissue Research (2012).
[35] G. Paltauf and H. Schmidt-Kloiber, Appl. Phys. A **62**, 303 (1996).
[36] W. Soliman, T. Nakano, N. Takada, and K. Sasaki, Japanese Journal of Applied Physics **49**, 116202 (2010).
[37] Lord Rayleigh, Philos. Mag. **34**, (1917).
[38] W. Lauterborn and C.-D. Ohl, in *In Fascination of Fluid Dynamics*, edited by A. Biesheuvel and G. F. Heijst (Springer Netherlands, Dordrecht, 1998), pp. 63–76.
[39] M. Frenz, G. Paltauf, and H. Schmidt-Kloiber, Phys. Rev. Lett. **76**, 3546–3549 (1996).
[40] G. Sankin, W. Simmons, S. Zhu, and P. Zhong, Phys. Rev. Lett. **95**, (2005).
[41] P. A. Lawrence, *The making of a fly : the genetics of animal design* (Blackwell Science, Oxford [England]; Cambridge, Mass., USA, 1992).
[42] N. Harden, Differentiation **70**, 181 (2002).
[43] D. P. Kiehart, Current Biology **9**, R602 (1999).
[44] A. Jacinto, A. Martinez-Arias, and P. Martin, Nat. Cell Biol. **3**, E117 (2001).
[45] M. S. Hutson, J. Veldhuis, X. Ma, H. E. Lynch, P. G. Cranston, and G. W. Brodland, Biophysical Journal **97**, 3075 (2009).
[46] J. D. Franke, R. A. Montague, and D. P. Kiehart, Current Biology **15**, 2208 (2005).
[47] A. Scuderi and A. Letsou, Developmental Dynamics **232**, 791 (2005).
[48] X. G. Peralta, Y. Toyama, M. S. Hutson, R. Montague, S. Venakides, D. P. Kiehart, and G. S. Edwards, Biophysical Journal **92**, 2583 (2007).
[49] A. Rodriguez-Diaz, Y. Toyama, D. L. Abravanel, J. M. Wiemann, A. R. Wells, U. S. Tulu, G. S. Edwards, and D. P. Kiehart, HFSP Journal **2**, 220 (2008).
[50] R. Fernandez-Gonzalez, S. de M. Simoes, J.-C. Röper, S. Eaton, and J. A. Zallen, Developmental Cell 17, 736 (2009).

CHAPTER 2

MATERIALS AND METHODS

2.1 Introduction

To study tissue mechanics using multi-point laser ablation we needed to design and build two experimental subsystems. First, an existing sequential single-pulse ablation system was modified to include a spatial light modulator (SLM) and the accompanying opto-mechanical elements. Software for controlling the SLM was developed in-lab using a combination of LabVIEW (National Instruments, Austin, TX) and Visual C++ (Microsoft, Redmond, WA). This control software models the optical transfer function of the new ablation system and generates kinoforms – *i.e.*, phase patterns written onto the SLM – quickly and with sufficient uniformity to ablate live samples. Second, a high-speed imaging system was constructed using a diode laser "strobe" and a high-sensitivity camera synchronized to the ablation laser.

Drosophila embryos were dechorionated, and mounted on an aluminum holder. This holder is designed to maximize fluorescent imaging quality, without compromising the survivability of the mounted embryos. A computer model of the amnioserosa tissue was developed, and simulations run to compare with our experimental data.

2.2 Multi-point laser ablation using a spatial light modulator

At the start of this project, our lab was equipped with a single-point ablation system based on a design published by Kiehart *et al.* [1]. The new optical path builds on this by adding a spatial light modulator (SLM) along the beam path (Figure 2.1) and repositioning several of the original optical

elements. The new layout retains as much of the functionality of the original system as possible, and we can switch between single-point and multi-point ablation by replacing the SLM with a mirror.

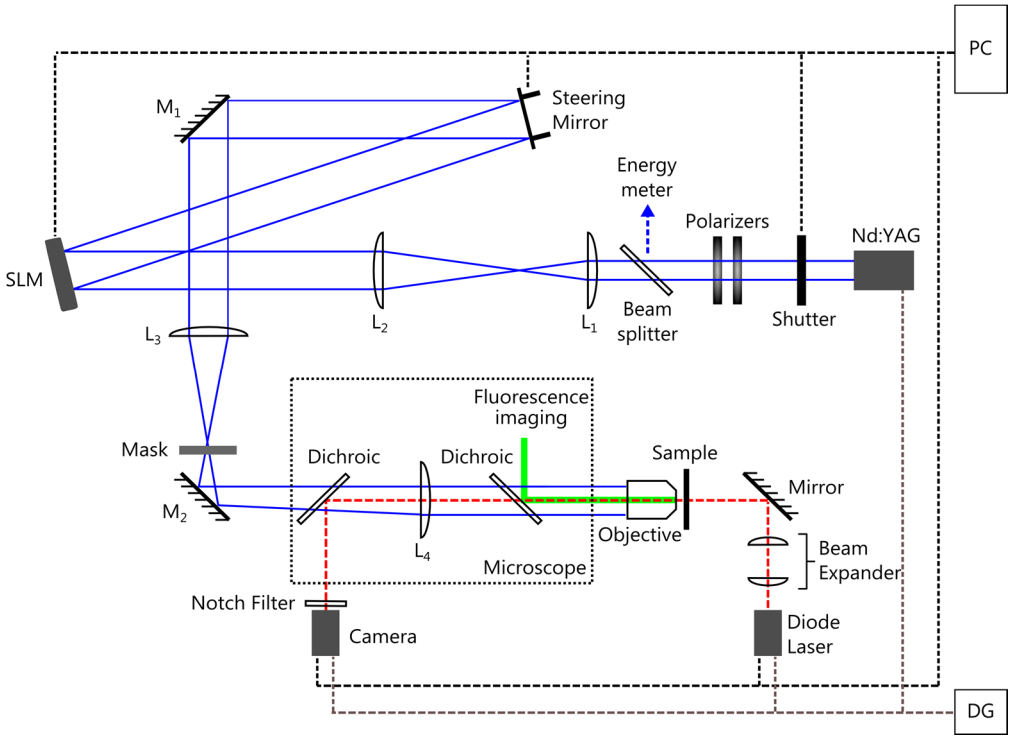

Figure 2.1: The ablation system. The ablation beam path is shown outlined in blue; the path of the excitation laser for fluorescent imaging is in green; and the high-speed bright-field imaging optical path is in red. The mirror M_2 reflects the beam vertically, through a port in the base of the inverted confocal microscope. The SLM, steering mirror, ablation laser shutter, high-speed camera, and diode laser are computer (PC) controlled. The camera and both lasers may be triggered using a delay generator (DG).

The SLM works as a programmable diffractive optical element that splits a single collimated laser beam into several separate ablation spots [2–4]. It does so by adding a position-dependent phase onto the beam incident on the active surface of the SLM. The phase-modified beam reflected from the SLM forms a diffraction pattern when transmitted through a lens and focused onto a sample. The maximum size and complexity of the diffracted pattern depend on the internal

characteristics of the SLM and the focal lengths and positions of the focusing optics of the ablation path.

There are several space constraints on the physical layout of the optical path. A large portion of the vibration-dampening optical table is occupied by a confocal fluorescent microscope, which is an integral part of the ablation system. In addition, the size of the SLM and the ablation laser units restrict their possible placement on the table. These constraints limit the maximum path length between elements and have an effect on the size of the final ablation pattern.

For ablation, we use the third harmonic of a Q-switched Nd:YAG laser (Minilite II, Continuum, Santa Clara, CA; λ = 355 nm, 5-ns pulsewidth, 8 mJ maximum energy, horizontal polarization). For most experiments this laser is used in its internally triggered mode, providing a continuous series of laser pulses at 10 Hz. A shutter placed in front of the exit aperture of the laser is used to control exposure of the sample. For experiments requiring precise synchronization, this laser may be externally triggered. A pair of polarizers allows precise control of the ablation pulse energy. Part of the ablating beam is picked off and focused on to an energy meter, which allows the pulse energy to be measured in real time.

To generate a pattern of ablation points we use a programmable 2D SLM (PPM X8267, Hamamatsu Photonics K.K., Japan; 768×768 pixels, 8-bits per pixel, 20×20-mm effective area) [5] in phase-only mode. This is an electronically-controlled, optically-addressed device where a computer generated 8-bit image is written to an internal liquid-crystal-display (LCD) and optically projected onto an amorphous silicon photoconductive layer attached to the main liquid-crystal (LC) layer of the SLM (Figure 2.2). Each pixel of this device is an independently controllable collection of birefringent liquid-crystals and adds a phase shift to any light reflected off the dielectric mirror sandwiched between the photo-conductor and LC layers. The LC layer is capable

of creating a greater than 2π phase shift for 355 nm light. The image projected onto the photoconductor is slightly, but intentionally out of focus so as to blur-out the pixel structure of the LCD and hence reduce aliasing effects. This blurring has an effect on the uniformity of the final output pattern and is compensated for by our control software.

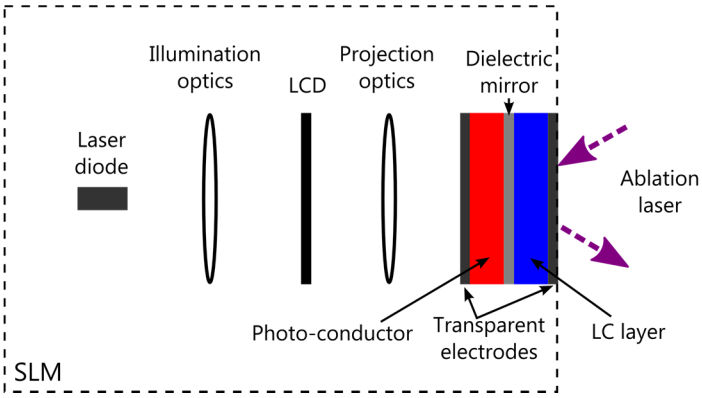

Figure 2.2: Internal design of the SLM. The image written to the LCD is projected on to the photo-conductor by the laser diode on the left. The ablation laser light enters from the right and is reflected by the dielectric mirror.

The basic ablation path consists of two pairs of lenses (L_1-L_2 and L_3-L_4) working as beam expanders and a steering mirror (SM). The two mirrors, M_1 and M_2, serve to bend the path to our requirements. The first beam expander consists of two lenses, L_1 (effective focal length, or EFL, for 355-nm light = 48 mm) and L_2 (EFL = 448 mm). L_1 can be translated along the optical axis to make the beam converge, diverge, or exit the beam expander collimated. These changes control the focal plane for ablation within the sample. Ideally the steering mirror should be at the focus of the second lens, L_2 [6]. This results in a constant beam spot size on the mirror surface, no matter what position is chosen for L_1. Because the beam on the steering mirror is transferred to the objective with a fixed reduction in size by the second, afocal, beam expander, the energy entering the objective is fixed, regardless of L_1 position (and hence the focal plane). Although inserting the SLM into the beam path meant we could not maintain this ideal positioning, this has no practical effect on our experiments because the focus of the ablation laser is always fixed to the same

plane as that of the fluorescent microscope's excitation laser, so as to image the structures we ablate. The focal lengths of L_1 and L_2 were selected to expand the approximately 3-mm diameter Gaussian laser beam to cover the 20×20-mm SLM LC surface area. The Gaussian nature of the beam, and hence the non-uniform illumination of the SLM LC is taken into account by the SLM control software.

Lenses L_3 (EFL = 484 mm) and L_4 (EFL = 165 mm, a permanently fixed tube lens located inside the microscope) form an afocal beam reducer, which serves to slightly overfill the back aperture of the microscope objective. L_3 also acts as the SLM's Fourier lens [4,5,7]. The steering mirror (SM) is positioned so that this pair of lenses focuses an image of the back aperture of the microscope objective onto the mirror surface. This positioning ensures that changing the angle of the mirror changes the angle at which the beam enters the objective, without changing the position of the beam. This prevents vignetting the beam and changing the energy entering the objective [1,6]. We can thus scan the ablation point over the field-of-view of the microscope without affecting the energy delivered to the focal plane of the objective. As the position and the focal length of lens L_4 are fixed, the appropriate positions of SM and L_3 are decided solely by the EFL of L_3.

For single-point ablations, the SLM can be used as a mirror (76% reflectivity at λ = 355 nm); however, to avoid exposing the LC to UV radiation unnecessarily, we use a mirror placed in front of the SLM. Switching between the SLM and the mirror can be done with little loss of efficiency.

Exposing the SLM to the high-powered pulsed UV ablation laser can damage the SLM. To estimate the damage threshold for this device, we directed the 3-mm-diameter ablating beam through a non-pixelated 25-mm-diameter LC test cell – essentially a large, single-pixel SLM (Boulder Nonlinear Systems Inc., Lafayette, CO) – and evaluated damage as a loss of voltage-dependent birefringence. Damage occurred for average laser intensity greater than 0.14 W/cm^2 at

a laser repetition rate of 10 Hz, which corresponds to peak intensity greater than 3.5 x 10^6 W/cm^2. During experiments we maintain a large safety margin by exposing the SLM to peak intensities of less than 1.9 x 10^5 W/cm^2 (pulse energies of less than 3 mJ). During a normal 5-hour experimental session the SLM is exposed to just 5-10 such ablation pulses as well as a few dozen much lower energy (~100 μJ) pulses during initial alignment. Even with these broad safety margins, this system is capable of simultaneous ablation at over thirty points in tissue using a standard, Neofluar microscope objective (~40% transmission at 355 nm). Performance of the liquid-crystal layer of the SLM may degrade with long-term UV exposure, but after 5 years of use (as of 2012), we see no significant degradation of the system.

The SLM adds a position-dependent-phase onto the Gaussian beam. After passing through the Fourier lens (L_3), the beam forms a diffraction pattern at an image plane between L_3 and L_4. The size of this pattern, which is transferred through the remaining optics to the ablation plane, depends on the EFL of the Fourier lens. This pattern contains multiple diffraction orders, of which only the 1^{st} positive order is useful experimentally. We use a knife-edge placed at the intermediate image plane as a simple beam block to remove the 0^{th} order and all negative orders. The higher positive orders are significantly weaker than the 1^{st} order and can be safely ignored as they are usually below the ablation threshold for tissue. The EFL of the Fourier lens, and the distance between pixel centers in the SLM limit the maximum ablation pattern size to a 160×160-μm area of the ablation plane, when using a 40× microscope objective. The beam block further reduces this to an effective area of 160×64 μm. Nonetheless, this is sufficient for a wide range of incisions in our target biological system.

Only a small fraction of the energy contained in the initial laser pulse is transmitted through to the ablation plane. Just 76% of the energy incident on the SLM is reflected by the internal dichroic

mirror. Less than 40% of that passes the beam block (the 1st diffractive order contains less than 20% of the light, but the mask also passes higher positive diffractive orders), and only 40% of light passing the beam block is transmitted through the objective to the sample. Thus, the 1st order pattern in the objective's focal plane contains less than 6% of the light incident on the SLM. Although it is possible to improve on this by using optical elements specifically designed to work with 355-nm light, it was not necessary for the purposes of this project.

2.3 A weighted Gerchberg-Saxton algorithm for generating phase patterns

The problem of finding an appropriate phase pattern, or kinoform, may be defined as follows. Given a desired intensity/ablation pattern, $I_F(\overrightarrow{r_F}) \propto A_F(\overrightarrow{r_F})^2$, and an initial Gaussian ablation beam with amplitude profile, $A_I(\overrightarrow{r_I})$, and uniform phase, we need to find a set of phases $\emptyset(\vec{r}_i)$ such that $|\mathcal{F}\{A_I(\overrightarrow{r_I})\exp[i\emptyset(\overrightarrow{r_I})]\}|^2 = A_F(\overrightarrow{r_F})^2$ [8,9]. Here, the subscript I refers to the beam at the SLM plane, and the subscript F refers to the beam at the ablation or target plane. Note that the phase pattern on the ablation plane $\emptyset(\vec{r}_F)$ is not important; only the amplitude, and thus the intensity, matters.

Mathematically, the simplest way would be to take the inverse Fourier transform of the desired pattern, using arbitrary final phase values. Unfortunately this approach would involve modulating both the amplitude and the phase of the beam: SLMs do not allow independent modulation of amplitude and phase [8]; and modulating the amplitude wastes energy and reduces efficiency [9]. Finding a suitable phase-only solution that would create the required intensity pattern in the ablation plane is not as straightforward. There is no analytical solution that yields a suitable kinoform for an arbitrary ablation pattern. Instead a numerical solution is required.

SLMs are often used in optical trapping experiments for dynamically generating optical traps [5–10]. Although the lasers used in these experiments are different from those used in microsurgical

applications, similar algorithms can be used to calculate approximate phase patterns. When selecting an algorithm, three things need to be considered, namely *uniformity*, *speed*, and *efficiency*. For our purposes, uniformity of the ablation pattern (Eqn. 2.1) is the most important factor. All points should receive approximately the same amount of energy.

$$uniformity = 1 - \frac{\max[I_k] - \min[I_k]}{\max[I_k] + \min[I_k]} \tag{2.1}$$

where I_k refers to the intensity measured at each of the points in the target pattern [8].

Speed is also important, as we are targeting living, dynamic tissue. All but the simplest algorithms used for calculating kinoforms are iterative. The time required for convergence to a suitable solution depends on the desired ablation pattern and degree of uniformity. It is therefore necessary to find a balance between desired uniformity and speed. Efficiency, defined here as the energy in the ablation pattern as a fraction of total energy delivered to the ablation plane, is not usually a concern. Energy is lost into "ghost" points in the pattern (usually a combination of higher diffraction orders and aliased points). In all but the simplest ablation patterns, these extra points receive much less energy than the main pattern. They are typically below ablation threshold and can be safely ignored. For simple patterns containing only one or two points, the 2nd and higher orders will be significant. In those cases one can introduce extra points in an area of the pattern blocked from reaching the sample just to weaken the effect of higher diffraction orders.

To generate kinoforms for our experiments, we implemented a weighted Gerchberg-Saxton algorithm (WGS) [8,9]. This is a medium-speed algorithm that is capable of producing highly uniform results. Table 2.1 compares the theoretical performance of a number of common algorithms. The most uniform of these is the direct search algorithm, which starts with a random

phase pattern and incrementally changes each point in the pattern to improve the quality of the final intensity pattern [9]. This painstaking process will find the most uniform result a given SLM is capable of producing, but is, on average, very slow. The WGS algorithm is almost as good, but significantly faster**.**

Table 2.1: Comparison of the theoretical performance of different algorithms for generating kinoforms for a 768×768-pixel 8-bit SLM. The target output pattern is a 10×10 square grid of points. The performance metrics are calculated after K iterations. N = number of SLM pixels, M = points in the target pattern, P = number of gray-levels the SLM is capable of displaying (256 in this case). Modified from Di Leonardo *et al.* [8].

Algorithm	Uniformity	Efficiency	K	Scaling
Random mask encoding	0.58	0.01	Not iterative	N
Superposition	0.01	0.29	Not iterative	N×M
Random superposition	0.01	0.69	Not iterative	N×M
Gerchberg-Saxton	0.60	0.94	30	K×N×M
Adaptive-Additive	0.79	0.93	30	K×N×M
Direct search	1.00	0.68	7.5×10^5	K×P×M
Weighted Gerchberg-Saxton	0.99	0.93	30	K×N×M

Our implementation of the weighted Gerchberg-Saxton algorithm [2,9,11–13] may be summarized as follows. Let the subscript F refer to parameters on the output (or target) plane and I to parameters on the input (SLM) plane, the superscript j to the results after the jth iteration of the algorithm, and the second subscript k to the kth point in the target pattern. Then $A_{F,k}^{j}$ would refer to the amplitude of the simulated electric field at the kth target point after j iterations of the algorithm.

1. Break up the target pattern (A_F) into a set of patterns each containing one point of the original pattern ($A_{F,k}$).

2. Create an array of random complex weights with a unit modulus (w_k^0), with one such weight per point in the target pattern.
3. Find the complex Fourier transform (H_k) of each single point pattern.
4. Multiply the k^{th} transformed pattern, H_k, by the k^{th} complex multiplier, w_k^j.
5. Sum all the resulting patterns to form a compound hologram.

$$A_I^j \exp\left(-i\theta_I^j\right) = \sum w_k^j H_k$$

6. Replace the amplitude of this hologram with the amplitude distribution of the initial laser beam, A_0, and convolve with the transfer characteristics of the SLM, $g(\vec{r})$.
7. Take the inverse Fourier transform of this new hologram.
8. Extract the amplitude information, A_F^j, and normalize to the highest amplitude value.
6. Replace the amplitude of this hologram with the amplitude distribution of the initial laser beam, A_0, and convolve with the transfer characteristics of the SLM, $g(\vec{r})$.

$$A_I^j \exp\left(-i\theta_I^j\right) \rightarrow A_0 \exp\left(-i\theta_I^j\right) * g(\vec{r})$$

7. Take the inverse Fourier transform of this new hologram.

$$A_F^j \exp\left(-i\theta_F^j\right) = \mathcal{F}^{-1}[A_O \exp\left(-i\theta_I^j\right) * g(\vec{r})]$$

8. Extract the amplitude information, A_F^j, and normalize to the highest amplitude value.
9. Compare the resulting target pattern with the desired pattern.
10. Create a new set of complex weights based on the phase and relative amplitude of each point. (Note that $A_{F,k}^j$ here refers to the normalized amplitude at point *k*.)

$$w_k^{j+1} = (1 - A_{F,k}^j) \exp\left(-i\theta_{F,k}^j\right)$$

11. If the desired accuracy has not been reached, go back to step 4.
12. Write the phase information, θ_I^j, from step 6 to the SLM.

There are a number of ways in which the weights can be adjusted after each iteration [6]. The one used in this version of the algorithm rapidly converges towards a solution, but on rare occasions the solution found may not be stable nor optimal. In those occasions, restarting the calculation may find a better solution, as a new set of random weights will be used to seed the algorithm. Figure 2.3 is a schematic of algorithm, showing how this iterative algorithm consists of distinct calculation and simulation steps. A more detailed flowchart of this WGS algorithm is presented in Figure 2.4.

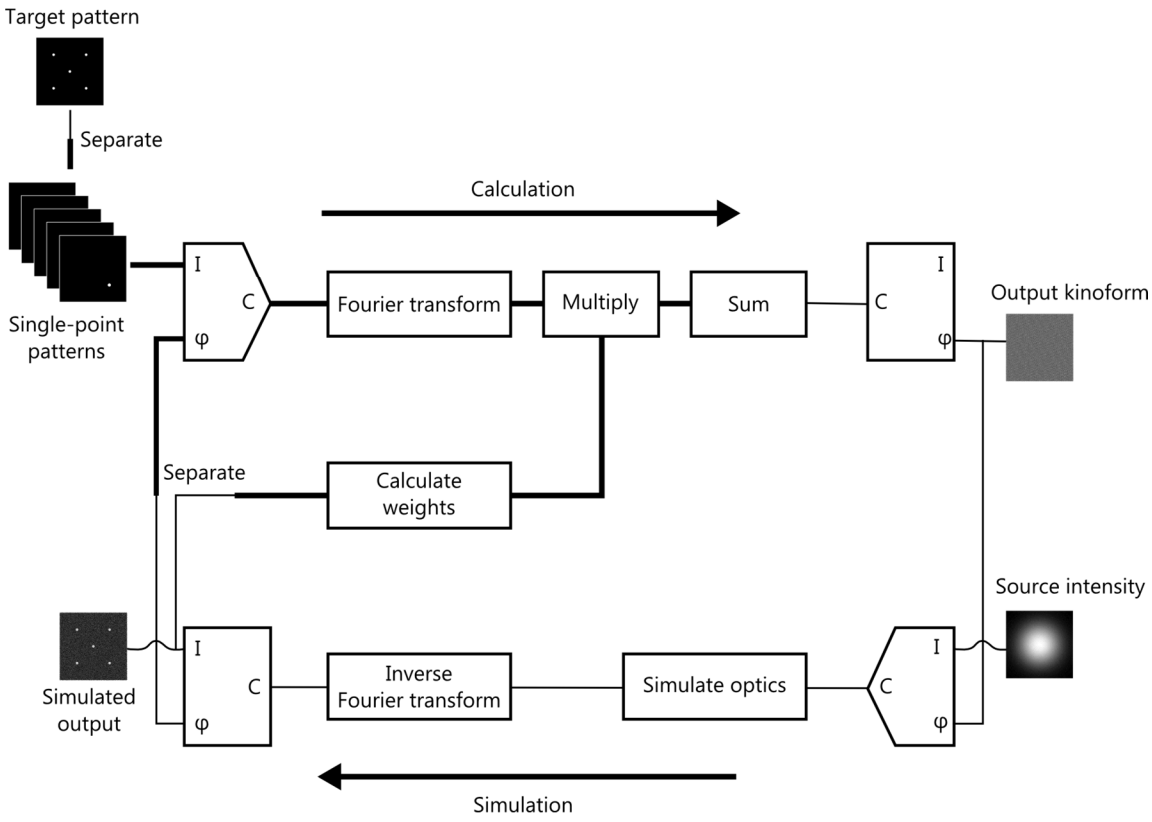

Figure 2.3: Schematic of the weighted Gerchberg-Saxton algorithm.

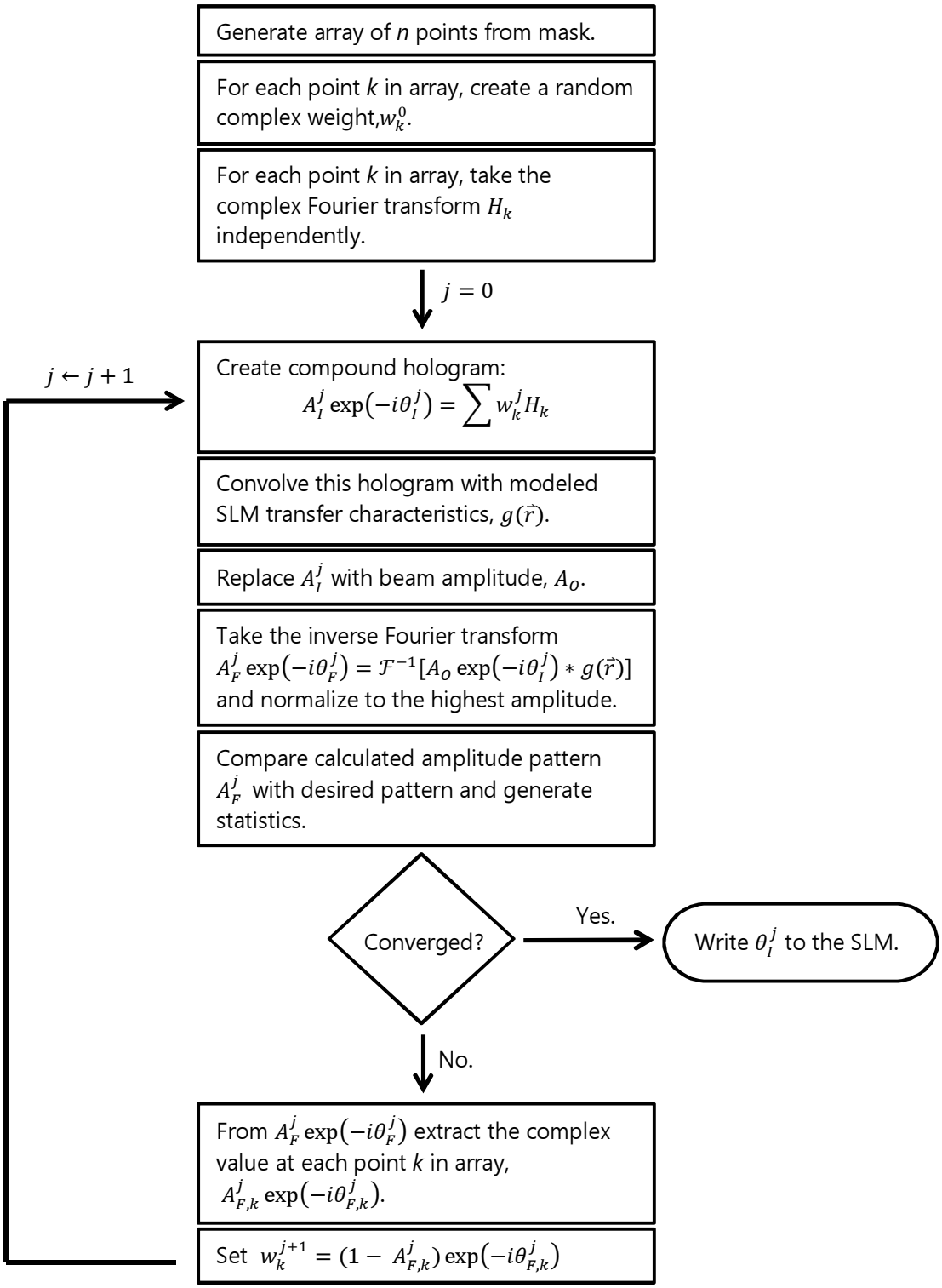

Figure 2.4: Flowchart for the weighted Gerchberg-Saxton algorithm used to control the SLM.

The software also accounts for the errors introduced into the kinoform by the slightly out-of-focus internal optics of the SLM. It does this by convolving the generated compound hologram with a 2D non-symmetric Gaussian blur, $g(\vec{r})$, before Fourier transforming it to simulate the output pattern. To estimate the approximate convolution function necessary for this task, we looked at the actual output generated by a non-convolved kinoform. The blur in the Fourier plane creates an intensity envelope in the image plane, with points closer to the center of the SLM field-of-view having higher intensities than points closer to the edge (Figure 2.5). By projecting the target pattern on to paper, and measuring the intensity of the fluorescence at each target point, it is possible to approximate the shape of this envelope and hence the necessary convolution function. The blur created by the internal optics of the SLM is not symmetric, and the width of the Gaussian convolution function had to be estimated separately for each axis.

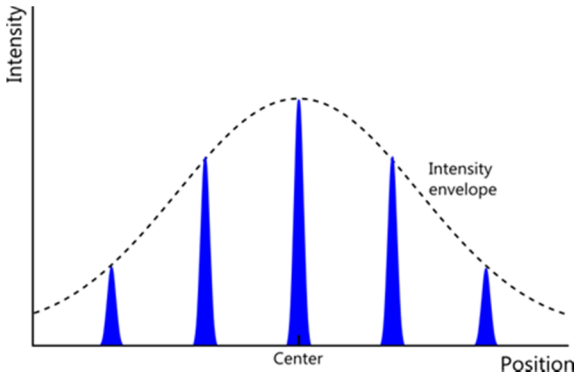

Figure 2.5: Intensity envelope in the target plane, caused by blurring in the Fourier plane. The intensity profiles of five target spots are shown in blue.

One can account for a number of other properties of the system in a similar fashion; however, since each additional calculation increases the time per iteration, it may not be optimal to include properties that have a minimal effect on the final output. An important factor that is not accounted for in the current version of the software is the mapping of each phase in the generated kinoform to an 8-bit intensity value written to the internal LCD of the SLM. The loss of

precision due to this transformation undoubtedly has an effect on the efficiency of the ablation pattern, but the calculations involved are computationally expensive. We thus perform this mapping only on the final output.

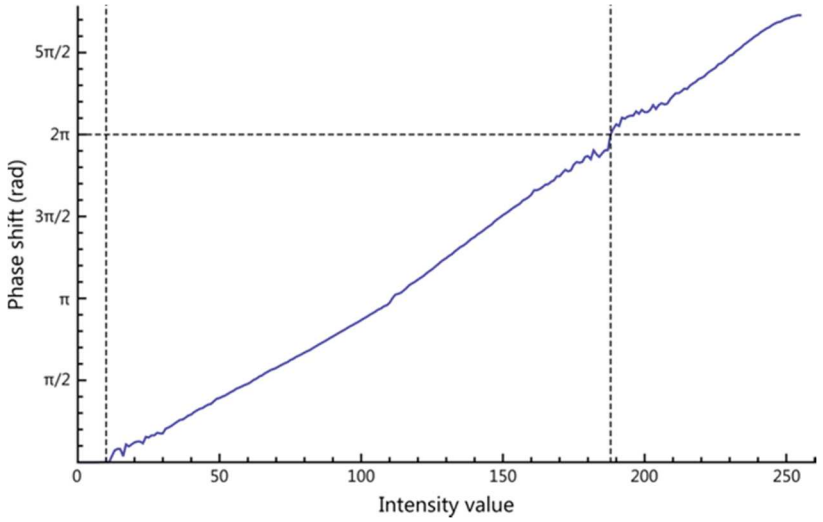

Figure 2.6: The phase shift as a function of the intensity value written to the SLM.

For this mapping we use a calibration curve specific to the SLM used in this project (Figure 2.6). Since this instrument was built to provide a better than 2π phase change using a 405-nm laser, the full range of intensity values are not necessary when working with the 355-nm ablation laser. In fact, all the real-valued phases calculated by the WGS-based software are mapped to an integer in the range 10 to 188. Even with just 178 usable intensity values, we can still quickly create precise target patterns (Figure 2.7). Currently, a single mapping function is used for every pixel in the SLM; however, different pixels actually have slightly different transfer functions. This pixel-to-pixel variation can be caused by multiple effects. First, the deterioration of the LC layer may affect different pixels to different degrees. Second, the illumination of the internal LCD of the SLM may not be uniform, which in turn would affect the intensity of the pixel projected on to the photoconductor. This has not had a noticeable effect yet, but could become an issue with time.

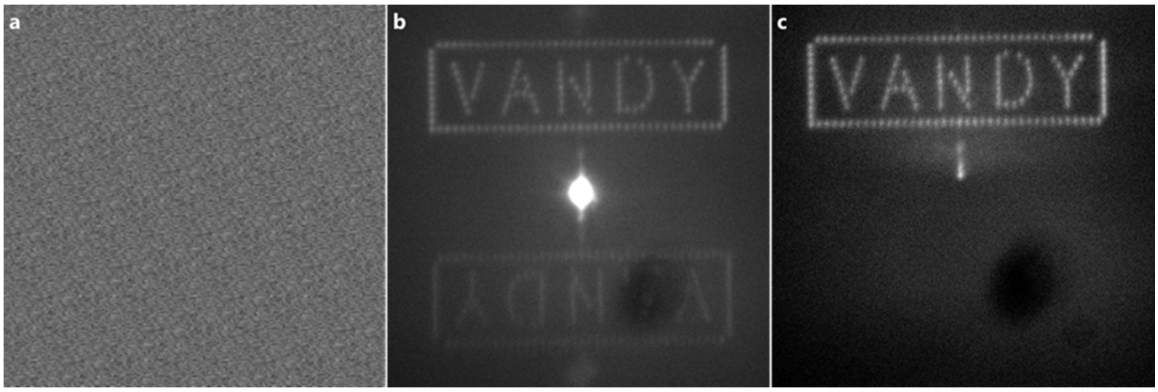

Figure 2.7: Example of a phase and output pattern. **a.** The kinoform encoded as an 8-bit image. **b.** The output pattern, imaged by directing the diffracted beam onto a sheet of white paper (focused using the microscope's tube-lens only to generate a macroscopic pattern ~10-cm across). The 1^{st} order, 0^{th} order and the 1^{st} negative order can be seen. **c.** The same pattern with the beam block in place on the intermediate image plane. The dark area on the lower right is an imhomogeneity in the paper target.

2.4 High-speed bright-field imaging

A second optical path was added to the system to image cavitation bubbles formed during ablation. This high-speed bright-field imaging system was designed to be cost effective and flexible. This system is built around a high-sensitivity CCD camera (CoolSNAP EZ, Photometrics, Tucson, AZ; 1392×1040-pixel 12-bit sensor, >60% quantum efficiency in the range 450 nm to 650 nm) and a pulsed laser illumination source. The illumination laser used most often is a diode laser (Cube, Coherent, Santa Clara, CA; λ = 660 nm, 61 mW) with controllable pulse duration. The camera is triggered before ablation, and the illumination laser is used as a strobe light with an accurately adjustable delay (controllable in 1-ns steps) and minimal jitter (<1-ns trigger-to-output delay jitter).

This system can image cavitation bubbles in liquid with illumination pulse durations as short as 7 ns. For imaging though the fly embryos, longer pulses (~0.5 μs) are needed to obtain sufficient contrast. We can also use the residual second harmonic (λ = 532 nm) light in the ablation beam as a significantly brighter illumination source. For this purpose a dichroic filter is placed in front of

the exit aperture of the Nd:YAG laser to separate the two wavelengths and direct the 532-nm light into a fiber optic cable. The laser pulse exiting the fiber is used in place of the laser diode (Figure 2.8). The length of the fiber determines the delay between the ablation and illumination pulses, and is not continuously adjustable as with the diode laser.

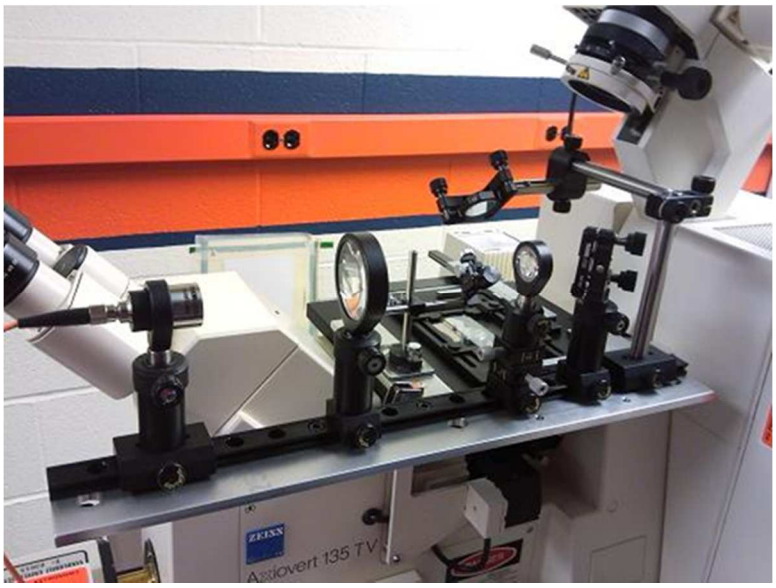

Figure 2.8: The bright-field illumination system mounted on the microscope. The fiber output coupling lens is on the left and can be replaced with the diode laser. Two mirrors on the right direct the beam on to the sample. A hydrophone used to measure pressure waves in liquid can be seen in the center, behind the two lenses forming the beam expander.

A delay generator (SRS DG645, Stanford Research Systems, Sunny Vale, CA) is used to trigger the ablation laser, camera and diode laser. This is also used to set the pulse duration for the illumination laser. A synchronization signal from the flash-lamp in the ablation laser is used as the timing signal for the delay generator (DG). The flash-lamp is left running at 10 Hz, with the shutter at the exit aperture of the Nd:YAG laser left open. The Q-switch of the laser is set to be triggered externally and is controlled by the delay generator. During an experiment, the camera is set for a 200-ms exposure, and is triggered by the DG immediately after it receives a sync signal from the flash-lamp (Figure 2.9). The DG triggers the Q-switch 150 μs after the flash-lamp fires, when the

energy stored in the ablation laser cavity is at a maximum. Finally, the illumination laser is triggered after a set delay.

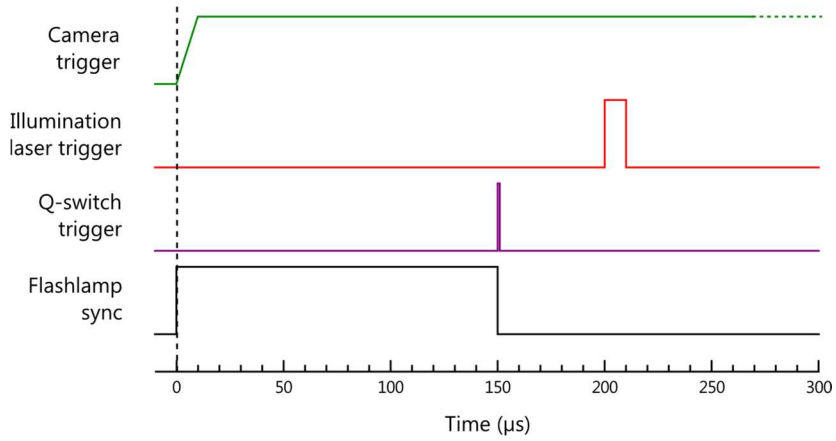

Figure 2.9: Timing diagram for the high-speed imaging system. The diagram represented is for a 10-µs illumination pulse initated 50 µs after ablation. The duration of the illumination pulse is set by the width of the illumination laser trigger signal. The time difference between the rising edges of the Q-switch trigger and illumination laser trigger signals sets the delay between the two laser pulses.

Although we can set the desired delay between ablation and illumination with sub-nanosecond accuracy, the accuracy of the actual delay is limited by the approximately 2-ns jitter inherent to the electronics controlling the ablation laser (the illumination laser has a jitter of less than 0.5 ns). Still, this jitter is much smaller than the usual illumination pulse duration (tens of nanoseconds to a few microseconds), and the lifetime of cavitation bubbles (tens of microseconds).

The dichroic used to couple-in the laser-scanning confocal system is removed during high-speed imaging. This is done to protect the photomultiplier tubes in the confocal system from inadvertent exposure to the illumination laser, and to remove a cause of transmission loss in the illumination path.

2.5 Sample preparation and mounting

Three different transgenic *Drosophila* strains were used in experiments described in this work. The most often used strain in our lab is *ubi-DE-Cad-GFP* (Drosophila Genetic Resource Center, Kyoto, Japan). This strain ubiquitously expresses a GFP-cadherin fusion protein to label epithelial cell borders [14]. *E-Cad:GFP; Sqh:mCherry* (gift from A. Jacinto, Instituto de Medicina Molecular, Lisbon, Portugal) labels epithelial cadherin proteins in green, and the myosin-regulatory-light-chain sqh (spaghetti-squash) in red. Experiments to investigate 3D cell shapes used embryos expressing the membrane marker *Resille(117–2)-GFP* [15] (gift from J. Zallen, Sloan-Kettering Institute, New York, NY).

The ellipsoidal, 500×200-μm embryos are collected and incubated until the required developmental stage is reached (approximately 24 hours at 15.5°C). They are then washed in a dilute bleach solution to remove the outer chorion layer, exposing the inner vitelline membrane [1,16,17]. The dechorionated embryos are then glued to a coverslip (#1.5, ~170μm thick) and lightly pressed down using a toothpick. Although the vitelline membrane of each embryo is firmly glued to the coverslip, the embryonic tissue is free to move and develop inside the enclosing membrane. The embryos are allowed to dehydrate for about five minutes, to further flatten the curved embryo, before being covered in a thin layer of hydrocarbon oil (#27, Sigma-Aldrich, St Louis, MO). The layer of oil prevents further dehydration while allowing oxygen to diffuse through to the embryo. Finally, an oxygen permeable membrane (YSI, Yellow Spring, OH) is placed on top and the coverslip attached to an aluminum sample holder (Figure 2.10).

For some experiments, we anesthetize embryos by flowing CO_2 or Ar gas over the holder, using a petri dish to cover the sample holder "well". Gas is pumped at ~5 psi through a small hose attached to the cover. Removing the petri dish/hose combination restores the embryos to normal

air. Embryos exposed to 2 hours of CO_2 will develop and hatch normally once oxygen is restored (24 of 24 *E-Cad:GFP; Sqh:mCherry* embryos hatched after exposure).

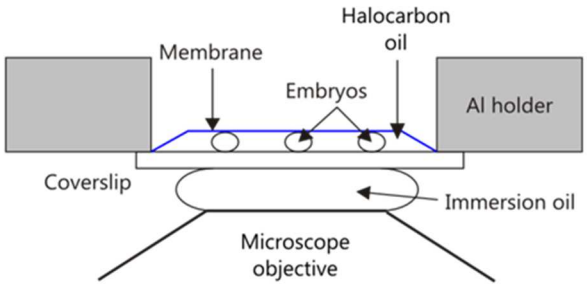

Figure 2.10: A cross-section diagram of sample holder (not to scale).

2.6 Modeling the behavior of isolated amnioserosa cells

The following description of the model constructed to simulate the dynamics of amnioserosa cells during dorsal closure was submitted to the journal as supplemental data for with the work described in *Chapter 4*. It is included here for completeness.

2.6.1 High elastic strain model

To model the oscillatory behavior of amnioserosa (AS) cells, we begin with the model of Solon *et al.* [18]. This model successfully simulates normal oscillatory behavior in the amnioserosa, as well as the behavior after point ablations.

The model contains 80 tightly packed polygons representing AS cells that are elastically linked to a fixed 200×150 μm ellipse, representing connections to the surrounding lateral epidermis (LE). Just as in Solon *et al.* [18], we generate an initial cellular configuration by selecting 80 random points within the bounding ellipse and annealing their positions using a repulsive interaction to achieve a reasonably homogenous distribution of forming points (Figure 2.11a). We then use Mathematica's Voronoi tessellation function [19] with these forming points to divide the ellipse

interior into convex polygons. Any vertices lying outside the ellipse are replaced by vertices on the ellipse boundary (Figure 2.11b).

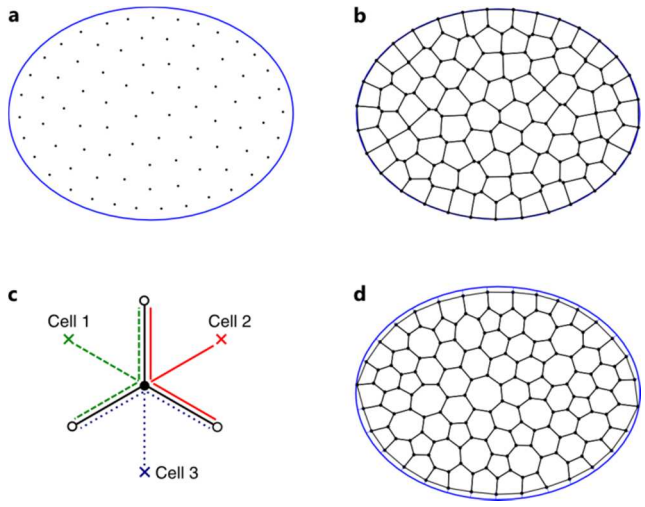

Figure 2.11: Diagrams of the model during initialization. **a.** Homogeneously distributed forming points within a fixed ellipse. **b.** Voronoi tessellation of the ellipse interior. **c.** Diagram showing the links attached to an interior vertex. Links within cells 1, 2 and 3 are colored green, red and blue respectively. **d.** Model annealed to a passive elastic equilibrium.

Within a single cell, each vertex is connected by springs to two other vertices and the cell centroid. Since three cells meet at each interior vertex, each such vertex participates in a total of six vertex-to-vertex links and three vertex-to-centroid links (Figure 2.11c). Vertices on the sheet boundary are shared between only two cells, but have an additional link to the fixed ellipse. Each such vertex therefore participates in four vertex-to-vertex, two vertex-to-centroid and one vertex-to-ellipse links. The vertices at the extreme left and right of the model form the canthi. They are connected to the fixed ellipse by springs that are 10× stiffer than other vertex-to-ellipse links.

The model solves a set of ordinary time-delay differential equations for the vertex positions. This set is described by Equations 2.1 and 2.2 (vectors in bold).

$$\dot{\mathbf{X}}_i = \frac{1}{\mu}\sum_j \left[k_{i,j}\left(\left|\mathbf{X}_j - \mathbf{X}_i\right| - L_{i,j}\right) + F_{i,j}\right]\hat{\mathbf{X}}_{i\to j} \qquad (2.2)$$

with $$F_{i,j} = F_{\max} \frac{1}{1+[\frac{\alpha A_{eq}}{A(t-\tau)}]^h} \quad (2.3)$$

where j is iterated over all connections to the i^{th} vertex, $\boldsymbol{X}_j$ represents the position of the j^{th} vertex, and $\widehat{\boldsymbol{X}}_{i\to j}$ is the unit vector from vertex i to vertex j. For each connection, Eqn. 2.2 has two parts: a spring-like term with spring constant $k_{i,j}$ and equilibrium length $L_{i,j}$ that depend on the link type (vertex-vertex, vertex-centroid, vertex-fixed ellipse); and an active stretch-induced contractile term, $F_{i,j}$, in the form of a time-delayed Hill function [20].

The equilibrium lengths of all vertex-vertex and vertex-centroid springs in this model are set to a constant L_0, chosen to be approximately 1/4 the links' ~20 μm average length. This places all such links under high elastic strain. The equilibrium lengths of all links to the fixed ellipse are taken as zero.

The Hill function describing active stretch-induced contractions goes to zero when the past area of a cell, $A(t-\tau)$, is much less than a critical multiple of its initial equilibrium area (αA_{eq}). As the past area exceeds this critical value, the Hill function rapidly reaches its maximum value, $\mathrm{F_{max}}$. The coefficient h sets the sharpness of this transition. The time delay, τ, sets the period of cell shape oscillations (slightly more than 2τ).

The modeled tissue is initially annealed to an equilibrium configuration based solely on the passive elastic links (Figure 2.11d). The Hill function is then turned on to begin oscillations. Figure 2.12a shows how the two components of this equation vary with time during the oscillation cycle of a typical simulated cell. Note that the passive elastic forces are always positive (tensile) in this model and never counteract the active contractions. The internal forces of every cell are thus always directed inwards.

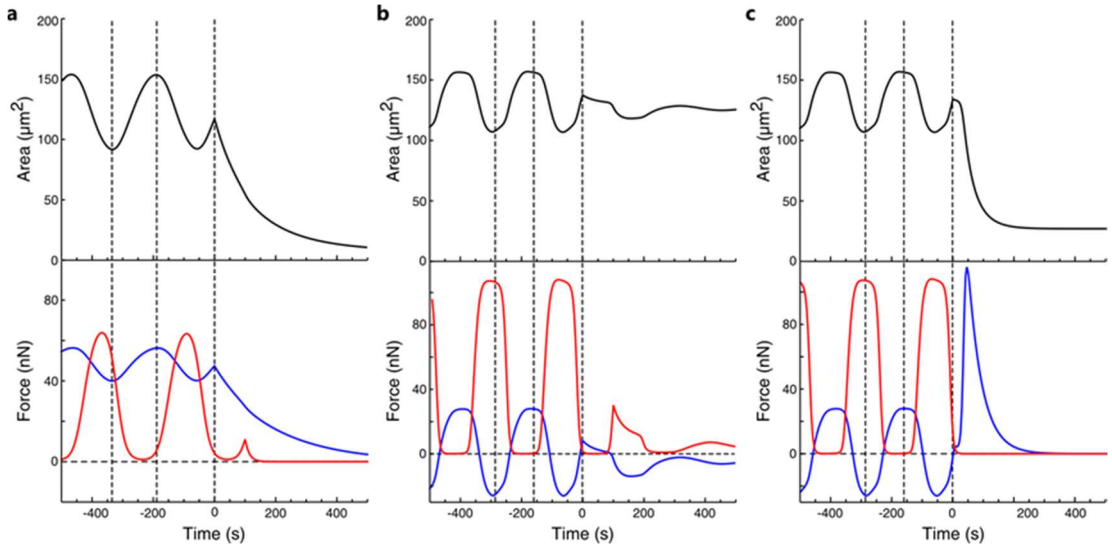

Figure 2.12: Matched graphs of area and cell-internal forces versus time for sample simulations using different models: **a.** high-elastic-strain model; **b.** low-elastic-strain model without an active contraction of cell-wound boundaries; and **c.** low-elastic-strain model with an active contraction of cell-wound boundaries. The active contractile force in the oscillating cell is shown in red. The average elastic force in this cell is shown in blue. Positive values denote tensile/contractile forces; negative values compressive/expansive forces. Ablation to isolate the oscillating cell occurs at t = 0.

2.6.2 Low elastic strain model

For this model, we modified Eqn. 2.2 as follows:

$$\dot{\mathbf{X}}_i = \frac{1}{\mu}\sum_j \left[k_{i,j}\left(\left|\mathbf{X}_j - \mathbf{X}_i\right| - S_{i,j}^{(1)} L_{i,j}\right) + S_{i,j}^{(2)} F_{i,j}\right]\hat{\mathbf{x}}_{i\to j} \tag{2.4}$$

where

$$S_{i,j}^{(1)\text{ or }(2)} = \begin{cases} 1 - 1\Big/\left[1+\exp\left(-\dfrac{t-\tau_d}{\tau_s}\right)\right] & \text{, if (1) link or (2) cell is adjacent to wound.} \\ 1 & \text{, otherwise.} \end{cases} \tag{2.5}$$

Note that the logistic functions $S_{i,j}^{(1)}$ and $S_{i,j}^{(2)}$ differ only in the situations for which each is triggered: the former only in edge-links directly adjacent to a wound, the latter on all links in each cell adjacent to a wound.

The simulated cell sheet is annealed under the conditions described for the high-elastic strain model. The equilibrium length of each spring, $L_{i,j}$, is then reset to the current length of that spring. Each link is thus under a low elastic strain (initially zero). Once oscillations begin, the passive elastic forces cycle between positive (tensile) and negative (compressive) phases. During the compressive phases, the passive elastic forces counteract the active stretch-induced contractions, yielding short periods during each cycle when a cell's net internal forces are directed outwards.

With low elastic strain and no active wound response, an isolated cell would not collapse, but would revert to its initial equilibrium size (Figure 2.12b). It is thus necessary to add a new active process represented by the logistic function $S_{i,j}^{(1)}$. For springs on cell edges adjacent to a wound, this factor drives the effective equilibrium length to zero. It thus represents a process that actively shortens all interfaces between healthy and wounded cells – both those in the isolated cell and those in the outer wound margins. The decay of $S_{i,j}^{(1)}$ causes cell-wound interfaces to shorten to the extent allowed by compression of vertex-centroid springs (Figure 2.12c). The second logistic function $S_{i,j}^{(2)}$ reduces the strength of the time-delayed stretch-activated Hill function term, $F_{i,j}$, in cells adjacent to a wound.

Both models effectively simulate oscillations in apical surface area, as well as the long-term behavior of point wounds, multi-point wounds and isolated cells. On the other hand, as will be shown in *Chapter 4*, only the low-elastic-strain model yields the correct behavior for isolated cells during the first 60 s after ablation.

2.6.3 Parameter selections for the models

The choice of a viscous damping coefficient, μ, has a significant effect on the simulation results. The models simulate viscous damping by treating each vertex as a particle submerged in a

uniformly viscous fluid. This simple representation does not differentiate between motions that change cell shape and those that simply translate all cell vertices. In reality, one would expect strong differences in the viscous resistance for these two types of motion. Vertex motion that changes the area or shape of a cell should experience strong effective damping due to the movement of mass away from (or towards) the surface and remodeling of the cellular cytoskeleton; rigid-body translation of a cell would encounter weaker damping. More complex vertex motions involve a combination of translation and reshaping, resulting in a broad band of effective viscosities. Nonetheless, one can effectively simulate a particular type of event by choosing an appropriate value for μ.

We can estimate the effective viscosity/elasticity ratio for quasi-translational motion by analyzing tissue recoil after ablation of a single cell edge [18,21]. Severing one link in an elastic network causes all vertices to move to new equilibrium positions. Assuming that any effects due to active contractions are negligible and that the effective viscosity is uniform over the time and length scales of this reconfiguration, we can fit the measured relaxation of vertices adjacent to the ablated edge to the exponential decay expected for a strongly overdamped spring (Figure 2.13a):

$$X(t) \propto \exp(t/t_0) \qquad \text{where } t_0 = \mu/k. \tag{2.5}$$

From our experiments we obtain an estimate for t_0 of 22 ± 3 s (mean ± SEM, N = 6). We used this value to inform our selection of parameters for simulations of cell-edge cuts.

In contrast to the expansion of a cell-edge wound, which is weighted towards translation of all vertices away from the wound site, the behavior of an isolated cell is strongly weighted towards reshaping. We thus left all other parameters constant, but used a higher effective viscosity for the simulation of cell-isolation experiments (Figure 2.13b).

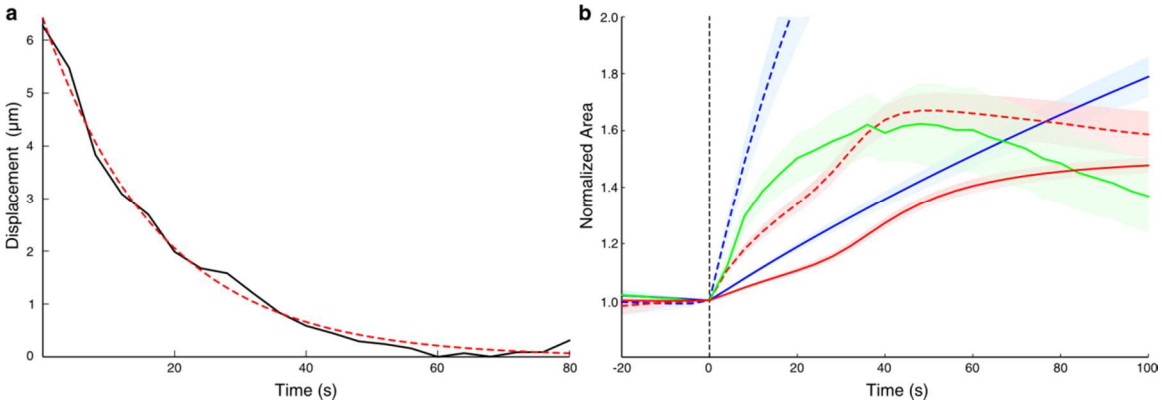

Figure 2.13: Selecting a viscous damping coefficient for the simulations. **a.** An experimental displacement versus time curve for a single vertex following a cell-edge cut (*black solid*) with the best fit of an exponential relaxation (*red dashed*). **b.** Graphs of normalized wound area versus time for experimental and simulated edge cuts. The average of four experimental cuts is shown in green. Simulation results from the high-elastic-strain model are shown in blue; those from the low-elastic strain model in red. The dashed curves use a smaller viscous damping coefficient than the solid curves. Shaded areas represent ±1 standard error of the mean.

Finally, we note a weakness in these models, which use a single tissue-wide parameter, τ, to set the oscillation periods. Experimentally, we see a relatively broad distribution of periods. In the simulations, all cells have nearly the same period. Even though we begin the simulations with random phases for individual cells, regular phase patterns eventually evolve. This synchronization leads to high amplitude oscillations in the total surface area of the simulated tissue. This uniform period has not been a significant issue when considering the behavior of a single cell, but it may be necessary to select a cell-specific time delay from a broader distribution for simulations that consider the coupled behavior of multiple cells.

Table 2.2: Parameter values used in the models

Parameter	Description		Value used in model	
			High-strain	Low-strain
μ	Viscous damping coefficient for cell-isolation simulations (nN·s/μm)		90	
	Viscous damping coefficient for edge-cut simulations (nN·s/μm)		18	
$k_{i,j}$	Spring constant (nN/μm)	v-v	0.25	0.90
		v-c	0.25	1.10
		v-e	1.20	1.20
$L_{i,j}$	Equilibrium length of spring (μm)	v-v,v-c	L_0 = 5	Link specific
		v-e	0	
F_{max}	Maximum activated contractile force (nN)		8	
α	Activation coefficient		1.1	
A_{eq}	Equilibrium apical area of a cell (μm^2)		Cell specific	
$A(t)$	Surface area of cell at time t (μm^2)		Cell specific	
τ	Time-delay for Hill function (s).		100	
h	Hill coefficient		10	25
τ_d	Activation delay for logistic function (s)		-	30
$1/\tau_s$	Slew rate of logistic function (s^{-1})		-	1/4

2.7 References

[1] D. P. Kiehart, Y. Tokutake, M. S. Chang, M. S. Hutson, J. Wiemann, X. G. Peralta, Y. Toyama, A. R. Wells, A. Rodriguez, and G. S. Edwards, in *Cell Biology: A Laboratory Handbook*, edited by J. E. Celis, 3rd ed. (Elsevier Academic, 2006), pp. 87–103.

[2] J. E. Curtis, B. A. Koss, and D. G. Grier, Optics Communications **207**, 169 (2002).

[3] E. R. Dufresne and D. G. Grier, Rev. Sci. Instrum. **69**, 1974 (1998).

[4] E. R. Dufresne, G. C. Spalding, M. T. Dearing, S. A. Sheets, and D. G. Grier, Rev. Sci. Instrum. **72**, 1810 (2001).

[5] Y. Igasaki, F. Li, N. Yoshida, H. Toyoda, T. Inoue, N. Mukohzaka, Y. Kobayashi, and T. Hara, OPT REV **6**, 339 (1999).

[6] E. Fällman and O. Axner, Appl. Opt. **36**, 2107 (1997).

[7] J. A. Neff, R. A. Athale, and S. H. Lee, Proceedings of the IEEE **78**, 826 (1990).

[8] R. Di Leonardo, F. Ianni, and G. Ruocco, Opt Express **15**, 1913 (2007).

[9] G. C. Spalding, J. Courtial, and R. Di Leonardo, in *Structured Light and Its Applications an Introduction to Phase-Structured Beams and Nanoscale Optical Forces.*, edited by D. Andrews (Academic Press, Amsterdam, 2008), pp. 139–157.

[10] P. M. Prieto, E. J. Fernandez, S. Manzanera, and P. Artal, Optics Express **12**, 4059 (2004).

[11] T. Haist, M. Schönleber, and H. . Tiziani, Optics Communications **140**, 299 (1997).

[12] G. Sinclair, J. Leach, P. Jordan, G. Gibson, E. Yao, Z. J. Laczik, M. J. Padgett, and J. Courtial, Optics Express **12**, 1665 (2004).

[13] R. Gerchberg, Optik **35**, 237 (1972).

[14] H. Oda and S. Tsukita, J. Cell. Sci **114**, 493 (2001).

[15] X. Morin, Proceedings of the National Academy of Sciences **98**, 15050 (2001).

[16] X. Ma, H. E. Lynch, P. C. Scully, and M. S. Hutson, Phys. Biol. **6**, 036004 (2009).

[17] D. P. Kiehart, J. M. Crawford, and R. A. Montague, Cold Spring Harbor Protocols **2007**, pdb.prot4717 (2007).

[18] J. Solon, A. Kaya-Çopur, J. Colombelli, and D. Brunner, Cell **137**, 1331 (2009).

[19] J.-R. Sack and J. Urrutia, *Handbook of computational geometry* (Elsevier, Amsterdam; New York, 2000).

[20] A. V. Hill, The Journal of Physiology **40**, (1910).

[21] G. Forgacs, R. A. Foty, Y. Shafrir, and M. S. Steinberg, Biophysical Journal **74**, 2227 (1998).

CHAPTER 3

HOLOGRAPHIC UV LASER MICROSURGERY

Aroshan K Jayasinghe[1], Jason Rohner[1] and M Shane Hutson[1,2,3,*]

[1]Department of Physics & Astronomy, Vanderbilt University, Nashville, TN 37235, USA
[2]Department of Biological Sciences, Vanderbilt University, Nashville, TN 37235, USA
[3]Vanderbilt Institute for Integrative Biosystem Research & Education, Nashville, TN 37235, USA

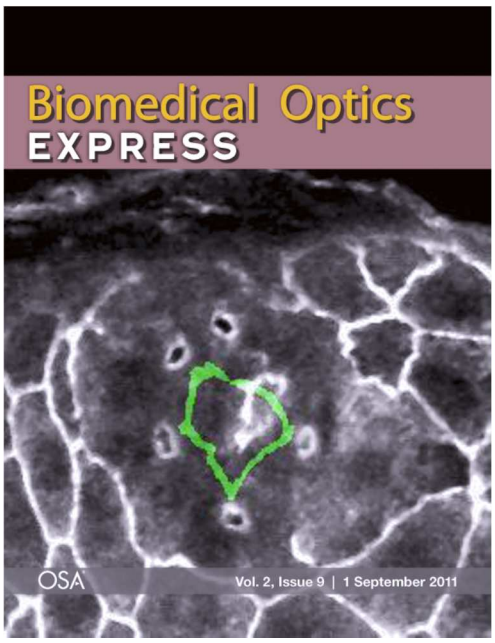

This work was published in the September 2011 issue of *Biomedical Optics Express* (Vol. 2, Issue 9.), and was featured as its cover article. Supplemental movies (designated in the text as Media 1-3) can be accessed through the journal's website, http://dx.doi.org/10.1364/BOE.2.002590.

Jason Rohner conducted damage threshold measurements on a liquid crystal test cell. Aroshan Jayasinghe designed the optical layout, programmed the system control software and conducted all other experiments herein.

3.1 Abstract

We use a spatial light modulator (SLM) to diffract a single UV laser pulse to ablate multiple points on a *Drosophila* embryo. This system dynamically generates a phase hologram for ablating a user-defined pattern fast enough to be used with living, and thus moving, tissue. We demonstrate the ability of this single-pulse multi-point system to perform two experiments that are very difficult for conventional microsurgery – isolating single cells *in vivo* and measuring fast retractions from large incisions.

3.2 Introduction

Laser microsurgery is a well-established method for studying the cellular forces that drive morphogenesis [1–5]. In many cases, microsurgery creates extended incisions in a tissue by ablating discrete points one at a time – a serial multi-pulse procedure. Such incisions have proven useful in determining the relative morphogenetic roles of different tissue regions; however, the quantitative interpretation of such experiments is limited. Only the first pulse ablates unaltered tissue; all subsequent pulses ablate tissue that is already retracting or undergoing strain relaxation. This motion makes some potentially useful microsurgeries very challenging – *e.g.*, cutting around a single cell or patch of tissue to mechanically isolate it from a surrounding epithelium – and strongly interferes with the quantitative measurement of retraction velocity after extended incisions [1]. Here, we present a method for circumventing these problems by simultaneously ablating multiple points in a living tissue. We do so by dynamically shaping the phase profile of a single laser pulse using a programmable spatial light modulator (SLM).

SLMs are widely used to dynamically control multiple optical traps, a technique known as holographic optical tweezers [6,7]. The primary difference between an optical trapping setup and

a microsurgical system is the use of a continuous-wave visible or near-IR laser in the former, but a pulsed laser in the latter. A wide variety of pulsed lasers have been used for laser microsurgery ranging from mode-locked near-IR systems running at 80 MHz to Q-switched UV systems running at only 10 Hz [8–12]. The choice of laser parameters for a given microsurgical application is driven by the scale of the targeted biological system (*i.e.*, multi-cellular, cellular or sub-cellular), the acceptable level of collateral damage and the time scales of the tissue dynamics of interest. Nanosecond UV lasers excel at cutting cell edges using just a single pulse to measure the mechanical retraction of surrounding cells on time scales of milliseconds and longer. Such experiments could also be done using amplified femtosecond lasers, but less-expensive nanosecond UV lasers ablate with similarly low thresholds [9,12]. They have thus become the instrument of choice for microsurgical investigations of cellular mechanics. Here we show how nanosecond UV lasers can be coupled with an SLM to provide new and innovative means to probe cellular mechanics. Although pulsed lasers have been used in SLM-based ablation systems to study multi-point cavitation in liquids [13–15], pulsed UV exposure places unique demands on SLM damage thresholds for holographic microsurgery. In addition, the simultaneous ablation of multiple points may lead to unintended interactions between multiple cavitation bubbles in the tissue – confounding interpretations of the post-ablation tissue movements. We investigate both potential limitations below and find that holographic microsurgery must consider both, but is not strongly limited by either.

3.3 Materials and methods

3.3.1 Optical path

Our experimental layout contains three independently controlled optical paths for ablation, confocal fluorescence imaging and high-speed bright-field imaging (Figure 3.1).

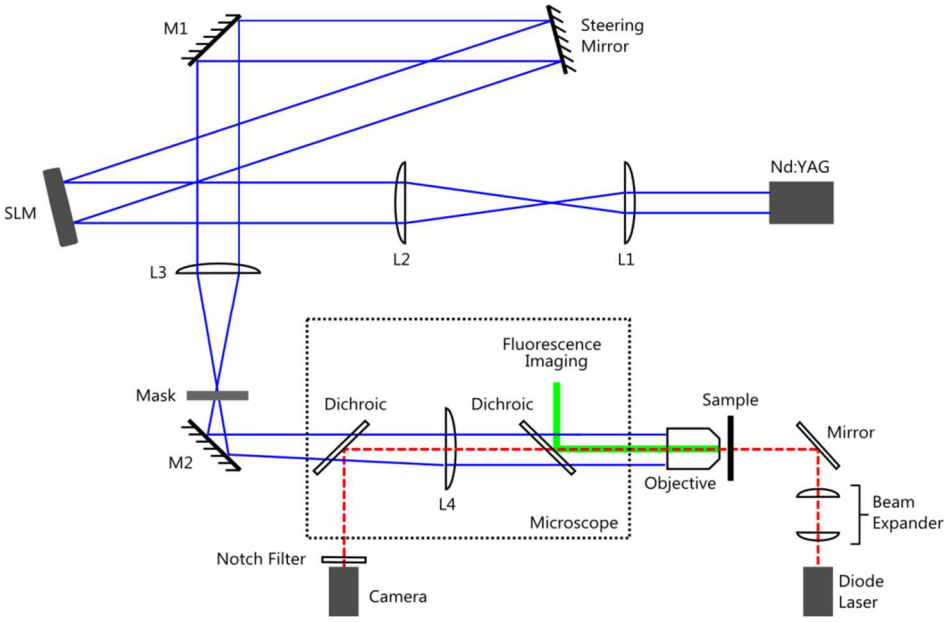

Figure 3.1: Optical layout with paths for ablation, high-speed bright-field imaging and confocal fluorescence imaging shown in solid blue, dashed red and thick green lines, respectively.

The ablation path transports light from the 3rd harmonic of a Q-switched Nd:YAG laser (Minilite II, Continuum, Santa Clara, CA; 4-ns pulse-width, λ = 355 nm) to ablate tissue with either a steerable single-point [3,16,17] or a single-pulse, multi-point configuration using a programmable phase-only SLM (PPM X8267, Hamamatsu Photonics K.K., Japan) [18]. For single-point ablations, the SLM can be used as a mirror (76% reflectivity at 355 nm); however, using an overabundance of caution, we avoid such use of the SLM and instead place a mirror just in front of it to avoid unnecessary UV exposure. This replacement can be made with little loss of efficiency [19,20]. Lens pair L_1-L_2 expands the ablating beam to fully cover the SLM's 20×20-mm active area. Lens pair L_3-L_4 then projects the phase-modified beam onto the back aperture of a microscope objective (40×, 1.3 NA). A mask placed at the conjugate focus after L_3 removes unwanted diffractive orders. To summarize energy losses in the optical path, 76% of the energy incident on the SLM is reflected, less than 40% of which passes the mask (the 1st diffractive order contains less than 20% of the light, but the mask also passes higher positive diffractive orders), and only 40% of light passing

the mask is transmitted through the optics and objective to the sample. Thus, the 1^{st} order pattern in the objective's focal plane contains less than 6% of the light incident on the SLM. The higher diffractive orders are individually weaker and below the threshold for ablation.

Since exposure to a pulsed UV laser could damage the SLM, we evaluated damage thresholds by directing a 3-mm-diameter beam through a non-pixelated 25-mm-diameter SLM test cell – essentially a large 'single-pixel' device (Boulder Nonlinear Systems Inc., Lafayette, CO) – and evaluated damage as a loss of voltage-dependent birefringence. At a pulse repetition rate of 10 Hz, damage occurred for average intensity greater than 0.14 W/cm^2, which corresponds to peak intensity greater than 3.5×10^6 W/cm^2. To maintain a large safety margin, we only exposed the SLM to peak intensity $<1.9 \times 10^5$ W/cm^2. With the current optical configuration, this corresponds to pulse energy < 3 mJ. The average intensity threshold is of lesser concern because the SLM is exposed to less than ten ablation pulses and a few dozen lower energy alignment pulses in a typical five-hour experimental session. Within these safety margins, our microsurgery system is still capable of simultaneous ablation at over thirty points.

The fluorescence imaging path is used to track cell and tissue movements and is needed for precise targeting of the ablating laser to specific cells or tissue regions. This path is internal to an inverted laser-scanning confocal microscope (LSM 410/Axiovert 135TV, Carl Zeiss, Thornwood, NY). The high-speed bright-field imaging path is used to monitor the dynamics of ablation-induced cavitation bubbles (typically in a liquid sample instead of the highly-scattering tissues). The illumination source is a pulsed diode laser (Cube, Coherent, Santa Clara, CA; λ = 660 nm) and images are recorded by a high sensitivity CCD camera (CoolSNAP EZ, Photometrics, Tucson, AZ). A filter in front of the camera cuts out all light except for a narrow band around 660 nm. The strobe length of the pulsed diode laser (≥ 10 ns) and the delay between the ablation pulse and

the laser strobe are both set using a digital delay generator (SRS DG645, Stanford Research Systems, Sunny Vale, CA). The imaging paths and ablating beam are co-aligned through dichroics to allow concurrent ablation and imaging.

3.3.2 Generating the phase hologram

To create a user-defined ablation pattern, we introduce a position-dependent phase onto the ablating beam's profile (using the phase-only SLM). The required phase hologram is calculated using a weighted Gerchberg-Saxton algorithm [21] that assumes a fixed amplitude profile in the phase plane and iteratively varies the phase hologram [20,22]. An initial guess for the appropriate phase hologram is generated by discretizing the desired ablation pattern (*e.g.*, a 10-μm line segment might be approximated by six points spaced 2-μm apart), calculating the 2D Fourier transform of each point independently, multiplying each transform by a different complex number or weight, summing all of the weighted transforms, and taking the spatially varying phase of this final sum. This initial guess is then used, together with the known optical characteristics of our system, to calculate the expected intensity distribution in the objective image plane. The uniformity of this distribution is used to calculate a new set of complex weights for the next iteration. This process is repeated until the calculated output converges on the target ablation pattern with sufficient uniformity. The weighting scheme prioritizes speed and uniformity over diffraction efficiency. As such, efficiency is low (<20%) and drops rapidly as the number of points increases. Given this drop in efficiency, the most complex pattern we have been able to ablate contains sixty points. After convergence, the calculated phase hologram is written to the SLM as an 8-bit, 768×768-pixel image. The software for phase calculations and SLM control was developed and implemented using LabVIEW (National Instruments, Austin, TX) and Visual C++ (Microsoft, Redmond, WA).

The entire process – obtaining a confocal image of the sample, designing an ablation pattern, calculating the corresponding phase hologram, writing this pattern to the SLM, and finally performing the ablation – takes about two minutes. The actual time depends strongly on the number of points in the discretized target pattern. Using a 40× objective, the target pattern is limited to a 160×64-μm area by the magnification of the optical path and the distance between pixel centers in the SLM. This is sufficient for a wide range of incisions.

3.3.3 Sample preparation

All microsurgeries were performed on a transgenic strain of *Drosophila*, ubi-DE-Cad-GFP (Drosophila Genetic Resource Center, Kyoto, Japan), that ubiquitously expresses a GFP-cadherin fusion protein to label epithelial cell borders [23]. Fly embryos were incubated until mid-dorsal-closure stage, then prepared and mounted as described in [3]. Embryonic tissues were imaged and ablated close to the cells' apical surface. The ablations are carried out sufficiently above ablation threshold (2-5×) to ensure clean and complete incisions from a single pulse, despite small variations in sample preparation and tissue depth, as well as fluctuations in the ablating laser [3].

3.3.4 Cavitation bubbles

We can use high-speed images of cavitation bubbles to ensure that all the targeted points are above ablation threshold and there are no unintended ablation points introduced by the dynamically generated hologram. To image cavitation bubbles, the ablation laser was focused ~15 μm into a cuvette filled with an ethanol solution of laser dye (LD-390, Exciton, Dayton, OH; 0.56 g/L in 95% ethanol). We measured the ablation threshold of this solution (264 nJ) to be similar to that of embryonic tissue (215 nJ), and significantly less (approximately 1%) than that of deionized water (29.1 μJ). Nonetheless, for a given above-threshold pulse energy, the bubble

lifetimes are similar in all three samples (Figure 3.2). The advantage of having a low threshold is twofold. Less energy is required when recreating equivalent patterns of bubbles, and any effects due to a lack of uniformity in the output pattern will be easily seen.

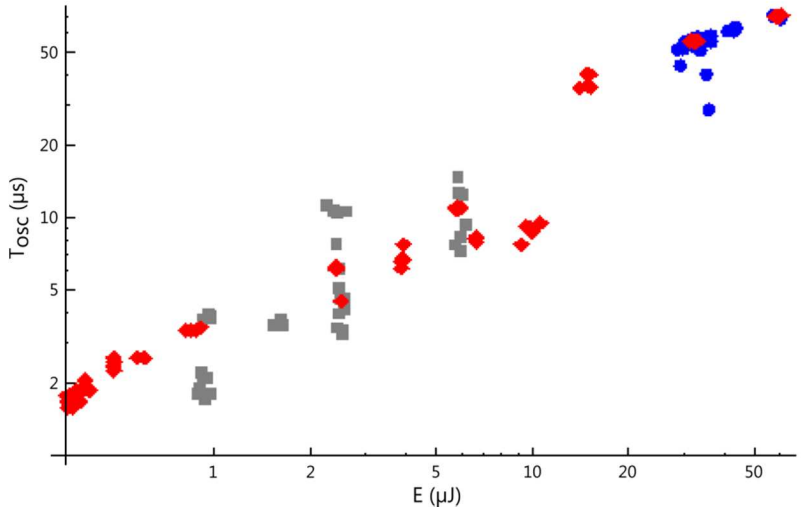

Figure 3.2: Lifetime of laser-induced cavitation bubbles as a function of energy incident on the sample: (*red diamonds*) solution of LD-390 in ethanol; (*gray squares*) fruit fly embryos; and (*blue circles*) deionized water. Although the ablation thresholds differ by a factor of nearly 100, the bubble lifetime for a given pulse energy is consistent across all three samples.

To calculate ablation thresholds we placed a needle hydrophone (HNR-0500, Onda, Sunnyvale, CA; 0.5 mm aperture, 2.5 mm outer diameter, <20 ns rise time, 2.24 V/MPa sensitivity) and recorded the pressure transients caused by the initial plasma and subsequent cavitation bubble collapse. The delay between these transients is directly related to the bubble lifetime and can be used in the Rayleigh formula to approximate the maximum bubble radius [9,24].

3.4 Results and discussion

One challenging, but potentially useful microsurgery is to mechanically isolate a single epithelial cell *in vivo* (Figure 3.3 and 3.4). The aim is to cut all of the cell-cell interfaces radiating away from

a target cell, leaving that cell intact, but unconnected to the rest of the cell sheet. The isolated cell should relax to a size and shape dictated by intracellular forces.

Our target epithelium is the amnioserosa at Bowne's stage 13 [25] of fruit fly embryogenesis. Amnioserosa cells at this stage are approximately 10-20 μm in diameter and 3-6 μm thick with five to eight neighboring cells. Ablating a hole clean through one of the visible cell-cell interfaces releases the tensile stress both along that edge and across the apical surfaces of the adjoining cells [26]. Thus, five to eight cell edges need to be cut to isolate a single cell from the rest of the tissue.

With the conventional ablation system, a computer-controlled mirror steers the beam to cut cell edges one at a time (Figure 3.3). This involves repeatedly taking confocal images of the tissue, targeting the moving edges and triggering the ablation laser. Each cycle takes tens of seconds, or longer if the tissue retracts strongly and one must wait to accurately target the next edge. During strong retraction, even an experienced operator will often miss a targeted edge, therefore requiring multiple ablations to cut some edges. During this drawn-out process, the cell-to-be-isolated may retract away from its original position and is often deformed by the anisotropic stresses present at intermediate stages. The order in which edges are targeted can usually minimize the retraction, but not the deformation. As a consequence, the size and shape of the isolated cell are not determined by intracellular forces, but are instead strongly influenced by the order and timing with which its connections to the rest of the sheet are severed. A high repetition rate laser, combined with a suitable scanning system can shorten the time required to cut a 30-μm diameter circle around a cell to just a few seconds [27,28], but this is still slow for use in applications that measure fast retractions on millisecond time scales [3].

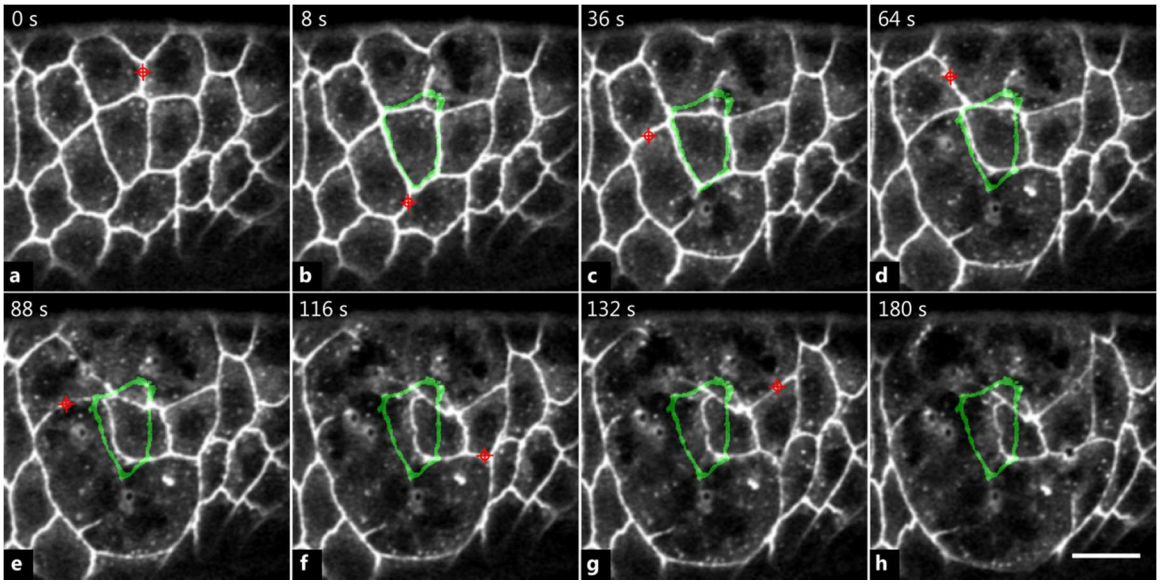

Figure 3.3: Isolating a single cell from the amnioserosa using a conventional multi-pulse system (Media 1). The energy of each ablation pulse was 6.3 μJ at the mirror in front of the SLM – approximately 1.3 μJ at the sample, which is approximately 5× the ablation threshold. Each panel shows a confocal image of the tissue either **a**. before or **b-h.** during and after the sequence of ablations. Green overlays show the original outline of the cell to be isolated. Red crosshairs demarcate targets for the next ablation pulse. The static bright rings in the post-ablation images are holes in the embryo's overlying vitelline membrane. The 20-μm scale bar is common to all images. The time stamp for each panel is relative to the first image.

We then performed the same experiment using the single-pulse multi-point system (Figure 3.4). To cut around a cell, we targeted the midpoints of all adjacent cell edges. Since the targeted cell edges may move during the iterative phase hologram calculation (at this stage of development, amnioserosa cells pulse with a period of about four minutes [29]), we targeted two closely spaced points per edge to maximize the probability of a clean and complete cut.

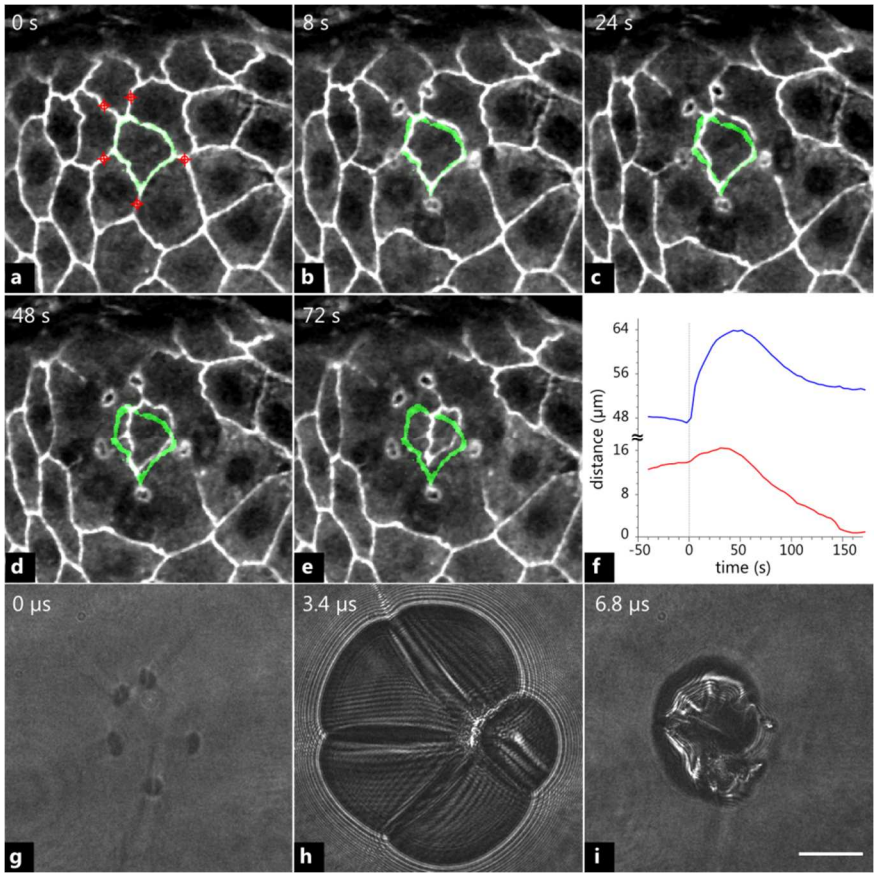

Figure 3.4: Isolating a single cell from the amnioserosa using the single-pulse multi-point system (Media 2). The energy of the ablation pulse was 171 µJ at the surface of the SLM – approximately 10.3 µJ at the sample, which is about 4× the threshold expected for ten single-point ablations. **a.** Confocal image of the tissue before ablation. Red crosshairs demarcate targets for ablation. **b-e.** Confocal images after ablation. One can clearly see five holes in the overlying vitelline membrane. Green overlays show the original outline of the isolated cell. The time stamp for each panel is relative to the first image. **f.** Comparison of the dynamic retraction of surrounding tissues (*upper curve*) and the collapse of the isolated cell (*lower curve*) as measured along a single line passing through the wound and isolated cell. **g-i.** High-speed bright-field images of cavitation bubbles in solution. Images taken immediately post ablation, at maximum extent and at collapse with 10 ns exposures. Five pairs of cavitation bubbles can be seen in *g*. The 20-µm scale bar is common to all images.

In the example shown, ten points are used to cut around the cell of interest, destroying six surrounding cells. The SLM-based multi-point ablation system is able to quickly and cleanly isolate a single large cell from the surrounding tissue with no visible damage to the isolated cell. Interestingly, although the surrounding tissue retracts strongly, the isolated cell initially shows only minor changes in shape, area and position (Figure 3.4b-c) Only later, as the surrounding

wound starts to heal, does the apical surface of the isolated cell autonomously contract (Figure 3.4d-e). We quantify these dynamics along a single line crossing the wound and isolated cell as shown in Figure 3.4f. The surrounding tissue initially retracts with a velocity of ~1.4 μm/s during the first four seconds, comparable to previous measurements in the amnioserosa [1,2,5,30,31] and slightly higher than the velocities seen for individually severed actin filaments in cultured endothelial cells [32]. Strain relaxation of this surrounding tissue occurs with a relaxation time of ~16 s and is complete by 50 s. In contrast, the apical surface of the isolated cell almost doesn't react to the ablation. Prior to ablation, it was expanding at a low rate of 30 nm/s; after ablation, it underwent a barely perceptible increase in expansion rate to 60 nm/s. Only after ~40 seconds does this isolated cell begin to contract at an average rate of 130 nm/s. Taken together, these results confirm that the tissue is under substantial tension; however, this tension places the cells under a very small elastic strain. Otherwise, the isolated cell would have immediately collapsed after ablation. On longer time scales, this isolated cell does undergo a sustained contraction, but the long pause implies that this is not a passive mechanical response. A thorough investigation of these biphasic dynamics and their implications for the mechanics of epithelial cells will be discussed elsewhere.

To assess the impact of cavitation bubbles on the ablated tissue, we used a hydrophone to measure the bubble lifetime *in vivo*. Using the same phase hologram and the same pulse energy on multiple embryos, we measured an average bubble lifetime of 6.9 μs. Using the Rayleigh relationship [24] for bubbles in water, this lifetime corresponds to a spherical bubble radius of 38 μm – surprisingly large given the limited damage evident in our confocal images. We could not directly image cavitation bubbles in the highly scattering *in vivo* environment, so we imaged lifetime-matched bubbles in a laser-dye solution (Figure 3.4g-i). For matched lifetimes, spherical bubbles in this ethanol-based solution are predicted to be 6% larger than in water [24]. During

the first 10 ns after the ablation pulse, one can clearly see five pairs of bubbles, corresponding to the five pairs of targeted ablation points (Figure 3.4g). Importantly, even with some energy in higher diffractive orders, there are no unintended bubbles. The five pairs of bubbles expand over the next few microseconds to abut one another at their maximum extent. The individual bubbles are smaller than the Rayleigh prediction, but the agglomeration has a maximum extent (~80 μm) very close to twice this predicted radius. This extent clearly does not match the damage evident in our confocal images, suggesting that bubbles produced in tissues do not behave the same as those in solution [33]. The *in vivo* bubbles may have a smaller extent for the same lifetime (due to elastic constraint by the surrounding tissue or to the fact that the environment of a fruit fly embryo is more nearly isochoric than isobaric) or may expand into the fluid trapped between the cell layer and the vitelline membrane that encases the embryo.

To further test the capabilities of the SLM-based system, we made linear incisions in the lateral epidermis of stage 14 fly embryos (Figure 3.5). Each targeted incision was discretized with points spaced approximately 4 μm apart. This spacing was chosen to make a quasi-continuous cut in the epidermis (the cells of which are 3-4 μm across) while minimizing the total laser pulse energy. In Figure 3.5, the shorter line is created by four ablation points, the longer by six.

In the confocal image immediately after ablation, one can see two lines of holes in the overlying vitelline membrane and some deformation of the epidermis (Figure 3.5b). At later times, large holes in the epidermis open perpendicular to each linear incision (Figure 3.5c-e). Using the same phase hologram and the same pulse energy on multiple embryos, we measured an average bubble lifetime of 6.8 μs. As before, this corresponds to a surprisingly large value for the predicted maximum bubble radius (37 μm) that is consistent with the maximum extent of matched-lifetime bubbles in laser-dye solution (~74 μm, Figure 3.5h). Nonetheless, since the

ablation process is complete within a few tens of microseconds, it is possible to measure a true initial retraction velocity and thus make solid inferences regarding variations in stress between adjacent segments of the epidermis. In a conventional laser microsurgery system, one must either compare incisions created in different embryos – thus conflating inter- and intra-embryo variations in tension – or compare sequential incisions in the same embryo – with the results dependent on the order of the incisions. The single-pulse multi-point ablation system eliminates both problems.

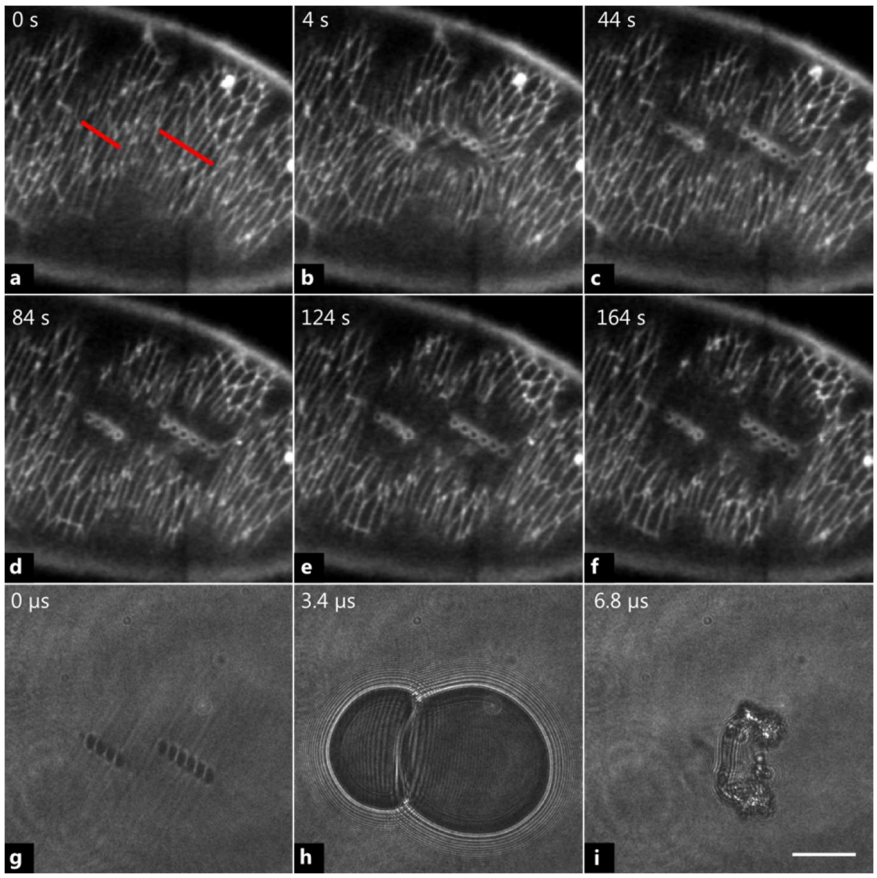

Figure 3.5: Multi-point ablation for linear incisions in the lateral epidermis (Media 3). The energy of the ablation pulse was 146 µJ at the surface of the SLM – approximately 8.7 µJ at the sample, which is approximately 3× the threshold for ten single-point ablations. **a.** Confocal image of the tissue before ablation. Red lines demarcate the targeted incisions. **b-f.** Confocal images after ablation. **g-i.** Lines of cavitation bubbles generated by same pattern in laser dye. Images was taken immediately post ablation, at maximum extent and at collapse with a 10 ns exposure. The common scale bar is 20-µm long.

One new question that does arise with the multi-point ablation system is the possibility of hydrodynamic interactions between multiple cavitation bubbles [13]. Jets formed between closely-spaced bubbles could ensure complete ablation of the targeted edges in Figure 3.3 and enhance the continuity of the linear incisions in Figure 3.5 [33–35]; however, the bubbles in these patterns expand to such an extent that small scale jets are obscured by the large scale asymmetric collapse of the bubble agglomeration (Figure 3.4i and Figure 3.5i). Nevertheless, one should measure the hydrodynamic interactions for each class of ablation pattern and take those interactions into account when interpreting the mechanical implications of microsurgery in tissues.

3.5 Conclusions

Using a programmable, phase-only SLM, we can successfully ablate multiple points over a wide area (approximately 160×64 μm) with a single pulse from a nanosecond UV laser. We can dynamically generate the necessary phase hologram quickly enough to use this technique for microsurgical applications in living embryos. Care must be taken to measure and limit hydrodynamic interactions between simultaneous cavitation bubbles, but with proper care, this technique opens up several interesting research avenues including isolating single cells *in vivo* and measuring fast retraction from arbitrarily shaped wounds.

3.6 References

[1] Y. Toyama, X. G. Peralta, A. R. Wells, D. P. Kiehart, and G. S. Edwards, Science **321**, 1683 (2008).

[2] M. S. Hutson, Y. Tokutake, M. S. Chang, J. W. Bloor, S. Venakides, D. P. Kiehart, and G. S. Edwards, Science **300**, 145 (2003).

[3] X. Ma, H. E. Lynch, P. C. Scully, and M. S. Hutson, Phys. Biol. **6**, 036004 (2009).

[4] D. P. Kiehart, The Journal of Cell Biology **149**, 471 (2000).

[5] X. G. Peralta, Y. Toyama, M. S. Hutson, R. Montague, S. Venakides, D. P. Kiehart, and G. S. Edwards, Biophysical Journal **92**, 2583 (2007).

[6] E. R. Dufresne, G. C. Spalding, M. T. Dearing, S. A. Sheets, and D. G. Grier, Rev. Sci. Instrum. **72**, 1810 (2001).

[7] E. R. Dufresne and D. G. Grier, Rev. Sci. Instrum. **69**, 1974 (1998).

[8] J. Colombelli, E. G. Reynaud, and E. H. . Stelzer, Methods in Cell Biology **82**, 267–291 (2007).

[9] M. S. Hutson and X. Ma, Phys. Rev. Lett. **99**, 158104 (2007).

[10] A. Vogel and V. Venugopalan, Chem. Rev. **103**, 577 (2003).

[11] V. Venugopalan, A. Guerra, K. Nahen, and A. Vogel, Phys. Rev. Lett. **88**, (2002).

[12] A. Vogel, J. Noack, G. Hüttman, and G. Paltauf, Appl. Phys. B **81**, 1015 (2005).

[13] K. Y. Lim, P. A. Quinto-Su, E. Klaseboer, B. C. Khoo, V. Venugopalan, and C.-D. Ohl, Phys. Rev. E **81**, (2010).

[14] P. A. Quinto-Su, V. Venugopalan, and C.-D. Ohl, Opt. Express **16**, 18964 (2008).

[15] A. Mao, Holographic Modulation of a Pulsed UV Laser Microbeam for Biophysical Investigations of Tissue Dynamics, Senior Thesis, Free Electron Laser Laboratory, Duke University, 2004.

[16] E. Fällman and O. Axner, Appl. Opt. **36**, 2107 (1997).

[17] D. P. Kiehart, Y. Tokutake, M. S. Chang, M. S. Hutson, J. Wiemann, X. G. Peralta, Y. Toyama, A. R. Wells, A. Rodriguez, and G. S. Edwards, in *Cell Biology: A Laboratory Handbook*, edited by J. E. Celis, 3rd ed. (Elsevier Academic, 2006), pp. 87–103.

[18] Y. Igasaki, F. Li, N. Yoshida, H. Toyoda, T. Inoue, N. Mukohzaka, Y. Kobayashi, and T. Hara, OPT REV **6**, 339 (1999).

[19] E. Martín-Badosa, M. Montes-Usategui, A. Carnicer, J. Andilla, E. Pleguezuelos, and I. Juvells, J. Opt. A: Pure Appl. Opt. **9**, S267 (2007).

[20] G. C. Spalding, J. Courtial, and R. Di Leonardo, in *Structured Light and Its Applications an Introduction to Phase-Structured Beams and Nanoscale Optical Forces.*, edited by D. Andrews (Academic Press,, Amsterdam:, 2008), pp. 139–157.

[21] R. Di Leonardo, F. Ianni, and G. Ruocco, Opt Express **15**, 1913 (2007).

[22] M. Montes-Usategui, E. Pleguezuelos, J. Andilla, and E. Martín-Badosa, Opt. Express **14**, 2101 (2006).

[23] H. Oda and S. Tsukita, J. Cell. Sci **114**, 493 (2001).

[24] Lord Rayleigh, Philos. Mag. **34**, (1917).

[25] J. Campos-Ortega, *The Embryonic Development of Drosophila Melanogaster*, 2nd ed. (Springer, Berlin;New York, 1997).

[26] M. S. Hutson, J. Veldhuis, X. Ma, H. E. Lynch, P. G. Cranston, and G. W. Brodland, Biophysical Journal **97**, 3075 (2009).

[27] J. Colombelli, E. G. Reynaud, J. Rietdorf, R. Pepperkok, and E. H. K. Stelzer, Traffic **6**, 1093 (2005).

[28] J. Colombelli, S. W. Grill, and E. H. K. Stelzer, Rev. Sci. Instrum. **75**, 472 (2004).

[29] J. Solon, A. Kaya-Çopur, J. Colombelli, and D. Brunner, Cell **137**, 1331 (2009).
[30] M. Rauzi, P. Verant, T. Lecuit, and P.-F. Lenne, Nat Cell Biol **10**, 1401 (2008).
[31] R. Farhadifar, J.-C. Röper, B. Aigouy, S. Eaton, and F. Jülicher, Current Biology **17**, 2095 (2007).
[32] S. Kumar, I. Z. Maxwell, A. Heisterkamp, T. R. Polte, T. P. Lele, M. Salanga, E. Mazur, and D. E. Ingber, Biophysical Journal **90**, 3762 (2006).
[33] I. Toytman, A. Silbergleit, D. Simanovski, and D. Palanker, Phys. Rev. E **82**, (2010).
[34] Y. Tomita, A. Shima, and K. Sato, Appl. Phys. Lett. **57**, 234 (1990).
[35] P. A. Quinto-Su and C.-D. Ohl, J. Fluid Mech. **633**, 425 (2009).

3.7 Acknowledgements

This work supported by the National Science Foundation (IOB-0545679) and the Human Frontier Science Program (RGP0021/2007C).

CHAPTER 4

DYNAMIC SHAPE OSCILLATIONS IN THE EMBRYONIC AMNIOSEROSA ARE CELL AUTONOMOUS: RESULTS FROM HOLOGRAPHIC LASER MICROSURGERY

Aroshan K. Jayasinghe[1], Sarah M. Crews[1] and M. Shane Hutson[1-3,*]

[1]Department of Physics & Astronomy
[2]Department of Biological Sciences
[3]Vanderbilt Institute for Integrative Biosystem Research & Education, Vanderbilt University, Nashville, TN

The following work has been prepared for journal submission.

Sarah Crews designed and characterized the apparatus for anesthetizing *Drosophila* embryos. Aroshan Jayasinghe designed and conducted the other experiments and programmed the computational model described herein.

4.1 Abstract

Holographic laser microsurgery, a newly developed technique for studying forces acting on tissue *in vivo*, is used to isolate single amnioserosa cells from the surrounding tissue during dorsal closure, a stage of *Drosophila* embryonic development during which amnioserosa cells periodically contract their apical surface area. We find that the post-isolation behavior of individual cells depends on the phase in this contraction cycle they were in at the moment of isolation. To investigate this further, we repeated these experiments on embryos anesthetized with CO_2 gas, and found that isolated cells retain their apical shape and size while under anesthesia and only contract once the embryo is revived. This suggests that amnioserosa cells are not under a significant membrane tension and that cell-autonomous contractile forces play an important part in reshaping the apical surface of individual cells, requiring significant changes to existing computational models.

4.2 Highlights

- Laser microsurgery isolates individual cells from a monolayer epithelium *in vivo*.
- Cells expanding before isolation do not immediately nor passively contract.
- These cells later actively contract in a process suppressed by CO_2 anesthesia.
- Computational models with highly stretched springs misrepresent the cell mechanics.

4.3 Introduction

Morphogenetic events in embryogenesis are often accompanied by changes in cell shape [1–5]. Although cell shape changes can and do drive tissue remodeling in isolated tissues, the situation is much more complicated for adjacent tissues that undergo complementary changes. If cells of tissue A contract along one axis and cells of tissue B extend in the same direction, it is not immediately clear which process is a case of active reshaping and which, if either, is a passive response. Such complementary changes in adjacent tissues occur in *Drosophila* embryogenesis during germband retraction and dorsal closure [6–8]. One can even find complementary cell shape changes within a single morphogenetically active tissue in the form of cell shape oscillations – *e.g.*, in *Drosophila* dorsal closure and ventral furrow invagination [9–14]. Both between and within tissues, the question of import is this: when an individual epithelial cell changes shape, is this process best characterized as viscoelastic or viscoplastic deformation due to forces internal to the deforming cell or forces exerted on that cell by its neighbors? Here, we address this question in the context of cell shape oscillations in the *Drosophila* amnioserosa. We use holographic laser microsurgery to mechanically isolate individual cells *in vivo*. The subsequent isolated-cell responses clearly show that these cells' shape oscillations are cell autonomous – much more so than suggested by previous models [14].

Cell shape oscillations occur in amnioserosa cells during the process of dorsal closure, which has long been of interest due to its experimental accessibility [6,7,15] and its similarity to wound healing [16–18]. During closure, lateral epidermis (LE) cells on the lateral flanks of the embryo elongate and move dorsally as amnioserosa (AS) cells on the dorsal surface contract and eventually invaginate [6,7,19]. The two flanks of lateral epidermis fuse at the dorsal midline and the invaginated amnioserosa cells undergo apoptosis [19–23]. During early dorsal closure, the

large squamous cells of the AS go through repeated cycles of apical expansion and contraction [14]. These cycles have oscillation periods of ~ 230 s, with neighboring cells typically out of phase. Previous work in the amnioserosa and other morphogenetically active tissues has shown that the contraction phases of periodic cell shape changes are driven by medial contractile networks on the cells' apical surfaces [11,24–27]. To date, the only examination of the expansion phases has been computational modeling that generated expansion of one cell via contraction of its neighbors [14].

Laser-microsurgery has often been used for evaluating biomechanics *in vivo* [15,28–35]. This technique has typically been used in a negative fashion – *i.e.*, ablate one or more cells of interest and investigate how the loss impacts the short and long-term behavior of adjacent cells. The short-term responses provide information on the mechanical force that was carried by the biological structure(s) that are now missing [32–34,36]. The long-term responses provide information on the system's ability to compensate for that loss [6,15,31]. Here, we complement these approaches; instead of ablating a cell of interest, we use a multi-point ablation technique to simultaneously ablate a ring of neighboring cells [37]. Post-ablation dynamics of the isolated cell are now driven by cell autonomous forces. Comparison of the pre- and post-ablation dynamics provides information on whether pre-ablation dynamics were driven by intra- versus intercellular forces.

4.4 Results and discussion

Our goal is to evaluate the autonomy of cell shape changes in an embryonic epithelium like the amnioserosa. To do so, we use holographic laser-microsurgery to mechanically isolate a single cell [37]. An example of such an experiment is shown in Figure 1a-e. Our protocol targets all

neighbors of the cell-to-be-isolated with ablation near the middle of each neighbor-neighbor interface – like targeting "spokes" emanating from the cell-to-be-isolated. These interfaces often move during the targeting process, so we ablate two closely spaced points for each interface to maximize the chance for a clean and complete cut [37]. The ablated locations are visible in Figure 1b-e as the static dark spots resulting from puncture wounds in the embryo's encasing vitelline membrane. Leakage through these holes is prevented by a glue layer between the membrane and coverslip [34]. Within the embryo, each laser wound extends clean through the ~ 6-μm thick epithelium [34]. Although we specifically target cell-cell interfaces, previous work has shown that such wounds quickly and effectively destroy all mechanical integrity in the two targeted cells [38]. This targeting strategy also provides a clear and immediate indicator of successful cell isolation via separation of the near and far fragments of fluorescently labeled interfaces.

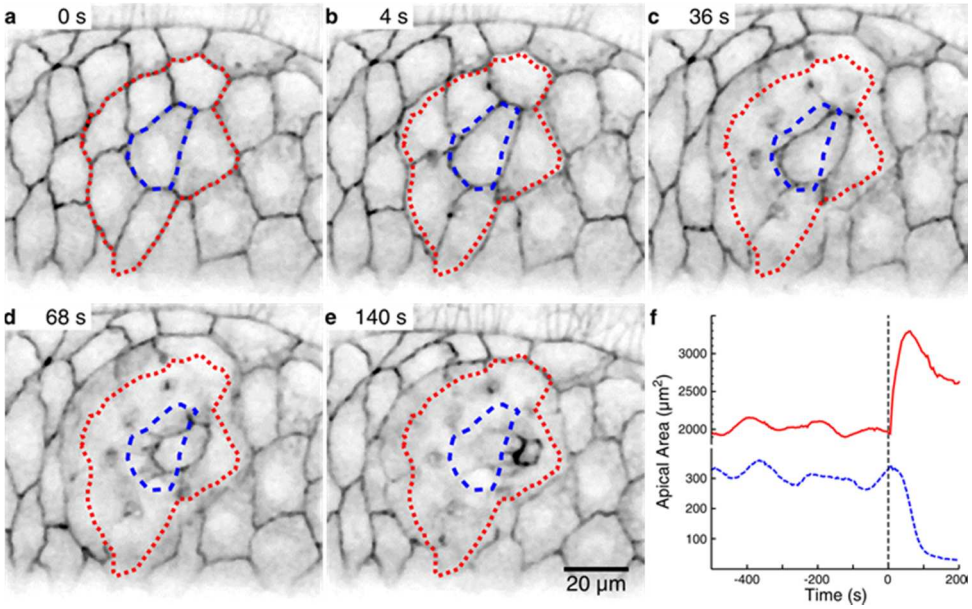

Figure 4.1: An example cell-isolation experiment. **a-e.** Pre- and post-ablation confocal images (inverted grayscale) showing retraction of the wound and eventual contraction of the isolated amnioserosa cell. Times relative to ablation are shown in the upper left. Overlays denote pre-ablation shapes of the isolated cell (*blue, dashed*) and the outer boundary of the wound (*red, dotted*). A common scale bar is shown in *e*. **f.** Comparison of cell shape dynamics for the total area inside the outer wound margins (*red*) and the apical area of the isolated cell (*blue, dashed*).

Since we are using a holographic technique to ablate multiple locations with a single 5-ns laser pulse, cell isolation is nearly instantaneous; even long-lived cavitation phenomena are complete within 100 μs [37]. We thus have access to short and long-term behavior of both the cell sheet and the isolated cell. Note that all times in our analyses are relative to the image taken immediately preceding ablation. The actual ablation event occurs between images.

As shown in Figure 1, the outer boundary of the wounded area begins to expand immediately after ablation. This is consistent with previous experiments and clearly shows that the cell sheet as a whole is under tension. The wounded area continues to expand for up to 30 s, but during most of this time, the outer wound boundary remains ragged. It starts to smooth out only as the wound reaches its maximum area and begins to decrease, *i.e.*, as wound healing commences. The isolated cell can behave very differently. In this particular example, the apical area of the isolated cell does not immediately collapse. It only does so about 40 s after ablation – very close to the time at which wound healing begins. The differences and correlations between the post-ablation dynamics of wound and isolated cell are most clearly seen in the area-versus-time graph of Figure 1f. In other examples of this experiment, the outer wound always behaves similarly; it expands, pauses, and contracts, with a maximum wound area attained several tens of seconds after ablation. On a similar time scale, the isolated cell always begins to collapse; however, the immediate post-ablation behavior of the isolated cell can differ markedly – sometimes contracting, sometimes expanding. We were thus interested in any correlations between an isolated cell's short-term post-ablation response and its pre-ablation behavior.

At this stage of embryonic development, individual amnioserosa cells are undergoing periodic expansions and contractions in apical area. Since these pulsation cycles have periods of ~ 230 s [14,26,39], we imaged each cell sheet for 600-900 s before ablation to capture multiple

contraction cycles. These images were segmented and the apical area versus time information was analyzed for each cell-to-be-isolated to estimate its pulsation amplitude, period and phase. We restricted subsequent analysis to cells with a pulsation amplitude > 5% of that cell's mean area, finding a period of 235 ± 45 s (mean ± s.d., n = 41 cells).

We used two analyses to investigate whether an isolated cell's short-term post-ablation response was related to its pre-ablation pulsing behavior. First, we simply grouped the experiments according to whether the apical area of the cell-to-be-isolated was expanding or contracting just before ablation. As shown in the mean area-versus-time graphs for each group (Figure 4.1a), the post-ablation responses differ. Cells that were contracting before ablation immediately contract a bit faster after ablation; cells that were expanding, momentarily pause (on average), and then contract in an accelerating manner. Second, we binned the experiments according to pulsation phase (12 bins of width $\pi/6$ where a phase of zero represents a maximally expanded cell) and calculated the post-ablation contraction rate, dA/dt, with the area of each cell normalized to its mean area prior to ablation. As shown in Figure 4.1b-c, this rate is strongly dependent on the isolated cell's pre-ablation pulsation phase. The initial post-ablation contraction rate is strongest (-2% per second) for cells that were already contracting strongly before ablation – *i.e.*, phases near $+\pi/2$ – and weakest (essentially zero) for cells that were rapidly expanding before ablation – *i.e.*, phases near $-\pi/2$. All of these movements are taking place at extremely low Reynolds numbers, so the differences cannot be attributed to inertia. They imply amnioserosa cell shape pulsations that are largely autonomous; the major driving force for expansion of a cell's apical area is not tension applied by neighboring cells, but is instead internal to the expanding cell.

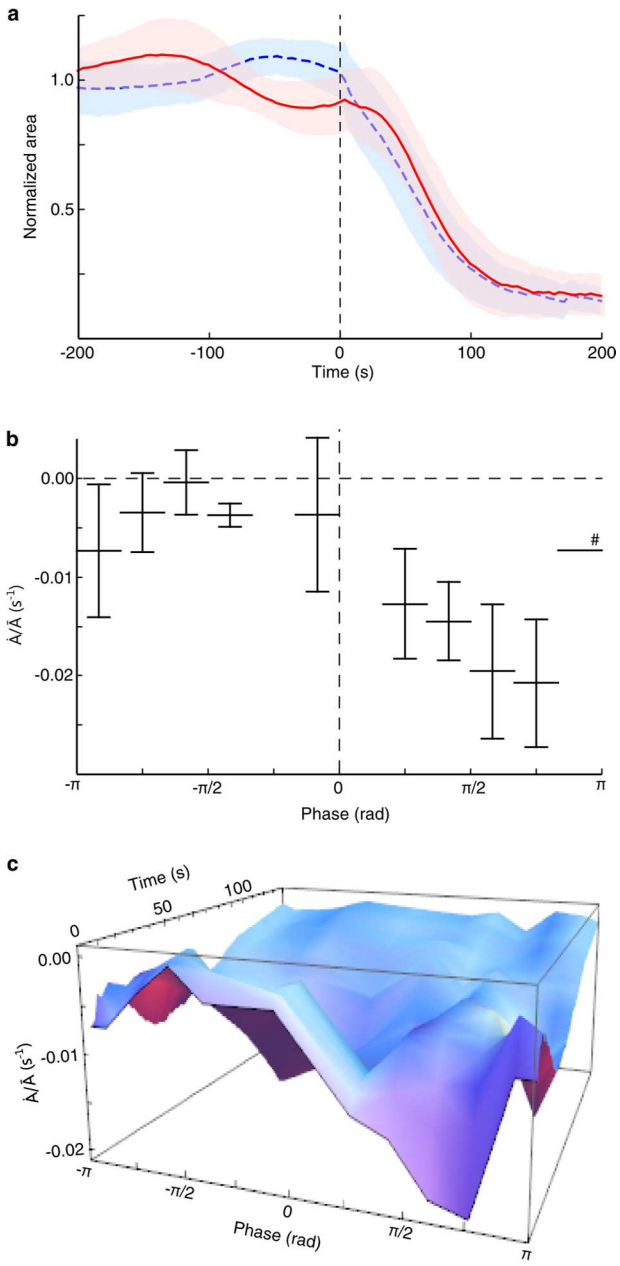

Figure 4.2. Dynamic changes in apical area after isolation of pulsating amnioserosa cells. **a.** Normalized apical area versus time for cells that were contracting just before ablation (*red, N* = 25) or those that were expanding (*blue, N* = 16). Lines denote the mean behavior of each group with shaded areas representing ±1 standard deviation. Individual cell areas were normalized to its average area before ablation, before the mean of the group was calculated. **b.** Initial rate of normalized area change, $\dot{A}/\bar{A}$, for cells isolated at different phases of their respective oscillation cycles. Results are grouped into twelve equal width bins from –π to +π. A phase of zero represents a cell at a temporally local maximum area. Horizontal lines are the means for each bin. Error bars show ±1 standard error of the mean. Two bins had no data and one bin (#) had only one data point. **c.** Surface plot showing longer term post-ablation behavior of $\dot{A}/\bar{A}$ versus time and pre-ablation oscillation phase.

On longer time scales, all isolated cells eventually collapse. Most importantly, cells with almost no initial post-ablation contraction increasingly accelerate their contraction rate over the next ~ 40 s (Figure 2c). Such accelerating contraction is inconsistent with simple elastic strain relaxation – suggesting the involvement of an active contraction.

4.4.1 Computational modeling of cell isolation experiments

To further explore the implications of our cell-isolation results, we turned to computational modeling of cell shape oscillations. The model by Solon *et al.* [14] approximates amnioserosa cells as polygons with each vertex embedded in a viscous fluid and connected to adjacent vertices and cell centroids by elastic springs (Figure 2.11). In parallel with each spring, the model includes active force elements that generate time-delayed, stretch-induced contractions. This arrangement yields cell shape oscillations that are typically out-of-phase in neighboring cells. When a cell is stretched beyond some threshold, a contractile response is triggered; after some time delay, this cell contracts and stretches its neighbors beyond threshold, which triggers contraction in the stretched neighbors and so on, resulting in pulsations with a period slightly longer than twice the time delay. For oscillations to occur in the model, the tissue as a whole had to be under tension. In the original publication of the model, this tension was produced by selecting an equilibrium length for each spring that was only ~25% of the average spring length, effectively placing each cell under an extremely high elastic strain (~ 3). Such high elastic strain is unrealistic in and of itself – no material is linearly elastic out to a strain of three – but it also directly conflicts our observation of points in the oscillation cycle when isolated cells have little to no immediate collapse, *i.e.*, they are only under small elastic strain.

Despite this conflict, the Solon model is quite successful at simulating both the contraction cycle of amnioserosa cells and the opening of cell-edge wounds after single point ablations [14]. To

determine whether the conflict actually yields any incorrect model predictions, we reproduced the original high-elastic-strain model, confirmed that our encoding yielded similar pulsations and wound responses, and then ran simulated cell isolation experiments. Not surprisingly, isolation of cells under high elastic strain leads to their rapid collapse (Figure 4.3a-c). This is a consequence of passive viscoelastic relaxation; any triggered contractions in the model only contribute in a time-delayed manner (> 100 s later). The high-elastic-strain model makes adequate qualitative predictions on long time scales – isolated cells contract in both the model and experiments – but it makes incorrect predictions with regard to the initial contraction rate. We ran 93 simulations that each isolated a pulsing cell at different points in its contraction cycle. Although the simulations do produce a phase-dependent response, the modeled cells collapse too quickly at all phases. Compare Figure 4.2a-c to Figure 4.3c-e. The largest discrepancy occurs for oscillation phases near $-\pi/2$, *i.e.*, cells that were expanding rapidly just before ablation. In our experiments, these cells had initial post-ablation contraction rates near zero, but in the model, they contract too rapidly. Rapid contraction occurs for all oscillation phases in the model because the parallel combination of high tensile elastic strain and active stretch-induced contractions is directed inwards for every cell at all times (Figure 2.11a).

We then sought minimal modifications of the model that would maintain pre-ablation oscillations and long-term wound retraction, while also replicating the *in vivo* behavior of isolated cells. The first change was setting the equilibrium length of each spring equal to its length at the start of the simulation, making this a low-elastic-strain model. The modeled tissue as a whole is still under tension, but individual oscillating cells can now have a net internal force that is transiently directed outward (whenever the elastic component is under a compression that exceeds the currently active stretch-induced contraction, see Figure 2.11b). This modification helps match experimental results for the initial post-isolation response; however, by itself, this single

modification also prevents the longer-term collapse of isolated cells. We thus introduce a second modification by which all unharmed cells actively reduce the length of their interfaces in contact with ablated cells. This active response is encoded in the model by a time-dependent sigmoidal function that drops the equilibrium length of each vertex-vertex spring to zero if both vertices are adjacent to a wounded cell. This response effectively minimizes the contact length between healthy and wounded cells and its time constant sets the time scale both for active contraction of an isolated cell and rounding up of a wound's outer boundary. A similar wound-triggered sigmoidal function is used to eliminate the stretch-induced contractions in cells that contact wounded cells. The long-term shape of an isolated cell is then determined by the balance between an active wound-induced contraction of its vertex-vertex springs and compression of its unaltered vertex-centroid springs. As shown in Figure 4.3f-j, this low-elastic-strain model reproduces pre-ablation pulsations and more closely simulates the behavior of a single isolated cell. In particular, both its short and long-term responses match the experimentally observed phase-dependence.

Reproducing the experimental results thus required two co-dependent modifications of the Solon *et al.* [14] model: (1) reduction of the elastic strain to near zero and (2) addition of an active contact-dependent response. We then ran additional experiments to see if these modifications are justifiable.

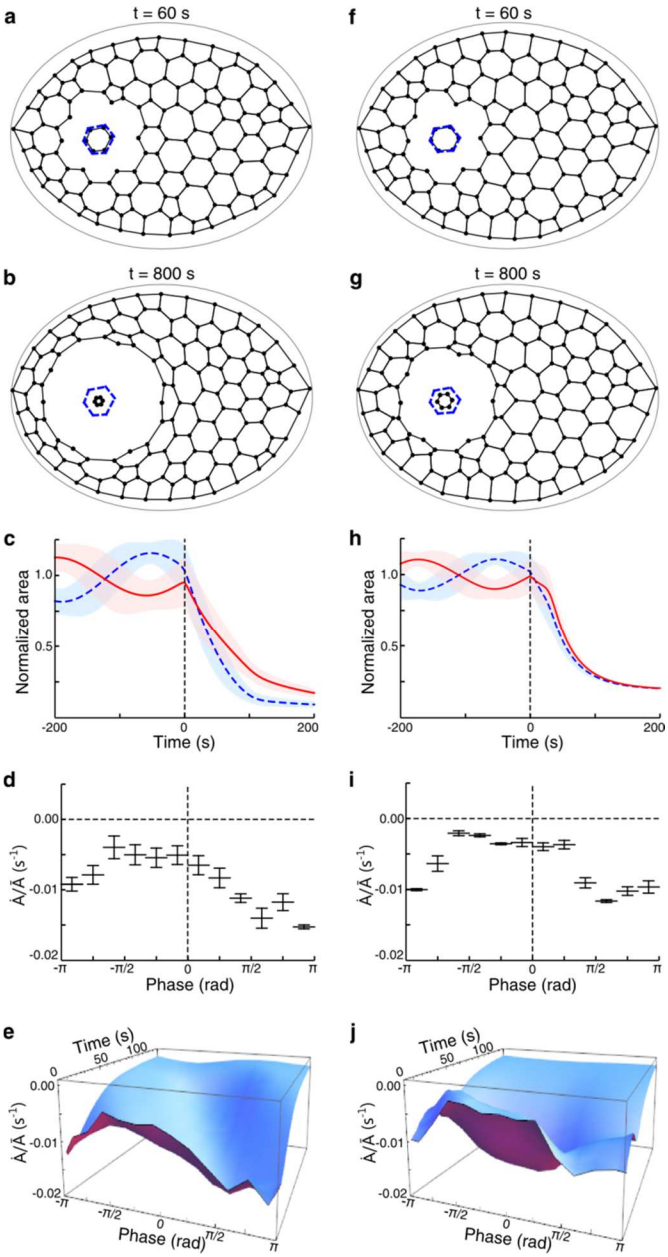

Figure 4.3: Comparison of high-elastic-strain and low-elastic strain models. **a-b.** Simulation of a cell-isolation experiment using a high-strain model. Blue outline shows the pre-ablation shape and size of the isolated cell. **c.** Normalized apical area versus time for cells that were contracting just before ablation (*red, N* = 48) or those that were expanding (*blue, dashed N* = 45). Lines denote the mean behavior of each group with shaded areas representing ±1 standard deviation. Individual cell areas were normalized to each cell's average area before ablation, before the mean of the group was calculated. **d.** Initial rate of normalized area change, $\dot{A}/\bar{A}$, for cells isolated at different phases of the oscillation cycle. Results are grouped into twelve equal width bins from –π to +π. Horizontal lines are the means for each bin. Error bars show ± standard error of the mean. **e.** Surface plot showing longer term post-ablation behavior of $\dot{A}/\bar{A}$ versus time and pre-ablation oscillation phase. **f-j.** Matching results for simulations using a modified low-elastic-strain model with active wound-induced contraction.

4.4.2 Cell isolation experiments under CO_2 anesthesia

To further investigate the role of active responses, we blanketed fly embryos with CO_2 gas – a common method for anesthetizing adult flies that also works on larvae and embryos [40,41] – and then conducted additional cell isolation experiments. When CO_2 is applied during early dorsal closure, amnioserosa pulsations cease within four minutes (Figure 4.4f), but residual tissue motion continues a few minutes longer, presumably until the cells reach a mechanical equilibrium under passive tension. When CO_2 is removed, initial tissue movements begin in just a few minutes, but the pattern of regular pulsations is not re-established until ~30-35 minutes later. With up to two hours of CO_2 exposure, embryos go on to develop normally and hatch. A similar temporary cessation of pulsations and morphogenetic progress can be induced by blanketing the fly embryos with argon, suggesting that this effect is largely due to transient anoxia.

We chose to wait ~15 minutes after starting CO_2 flow before mechanically isolating a single cell. As shown in Figure 4, the apical area of the cell-to-be-isolated stabilizes during this exposure, and then undergoes an immediate, but slight, post-ablation recoil (< 12% of its area). During the next 500 s, as the flow of CO_2 continues, the isolated cell retains its shape and area. The outer boundary of the wound opens slowly, but similarly retains its ragged shape. We then stopped the flow of CO_2 at 500 s after ablation and observed the longer-term resumption of an active response. Only ~900 s later does the wound start to significantly reshape (Figure 4d). At 2000 s after ablation (1500 s after CO_2 removal), wound healing is underway, but the isolated cell retains ~76% of its pre-ablation apical area (Figure 4.4f). Approximately 2500 s after ablation, there finally appears to be a strong contraction of the isolated cell's apical surface. At this point, the isolated cell's edges are significantly dimmer than the rest of the tissue – possibly due to the degradation of fluorescently-labeled cadherin junctions – which makes quantification difficult. Nonetheless, it

is clear that passive relaxation of elastic strain only accounts for a few percent of the isolated cell's contraction; the large remainder requires an active response.

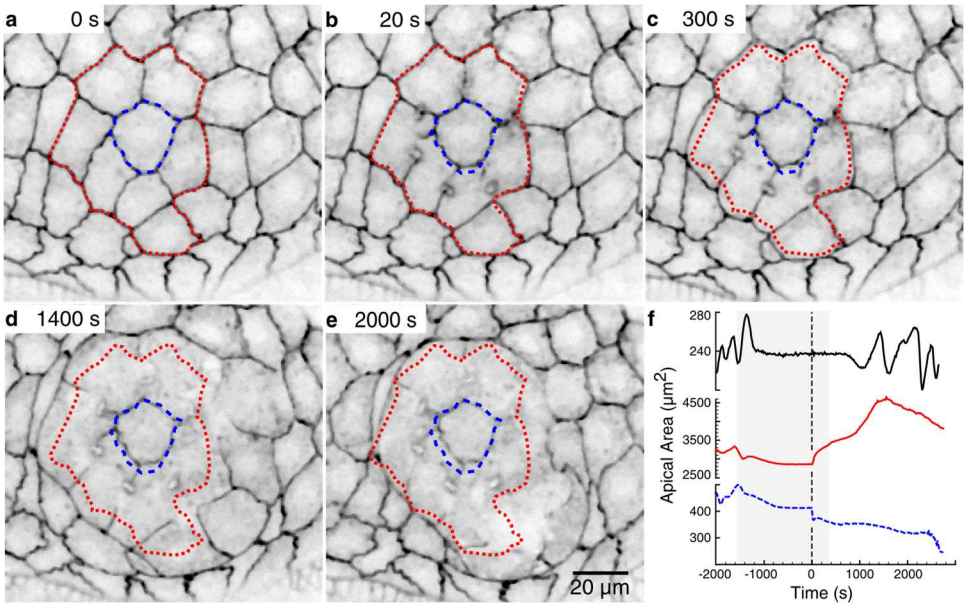

Figure 4.4: Cell isolation experiment in a CO_2-anesthetized embryo. **a-e.** Pre- and post-ablation confocal images (inverted grayscale) showing slow retraction of the wound and almost no contraction of the isolated cell. Times relative to ablation are shown in the upper left. Overlays denote pre-ablation shapes of the isolated cell (*blue, dashed*) and the outer boundary of the wound (*red, dotted*). A common scale bar is shown in *e*. **f.** Comparison of cell shape dynamics for the total area inside the outer wound margins (*red*) and the apical area of the isolated cell (*blue, dashed*). The uppermost curve is for a cell in a different embryo exposed to CO_2 for the same length of time, but not ablated (*black*). The shaded region denotes the duration of CO_2 exposure.

We then used both models to simulate cell-isolation experiments in embryos anesthetized with CO_2. We modeled anesthesia as the suppression of all active force terms, including the sigmoidal wound-response functions. As expected, the isolated cell and wound boundary behavior in the high-elastic-strain model failed to match experimental data (Figure 4.5a-e); the model's isolated cell collapsed immediately even under anesthesia. In contrast, the low-elastic-strain model is a good match to our experimental results (Figure 4.5f-i). Most importantly, isolated cells do not collapse under anesthesia (Figure 4.5j). Instead, the targeted cell snaps back to its equilibrium size

post-ablation, and retains this size until active forces resume (Figure 4.5f-h) – very similar to our experimental observations.

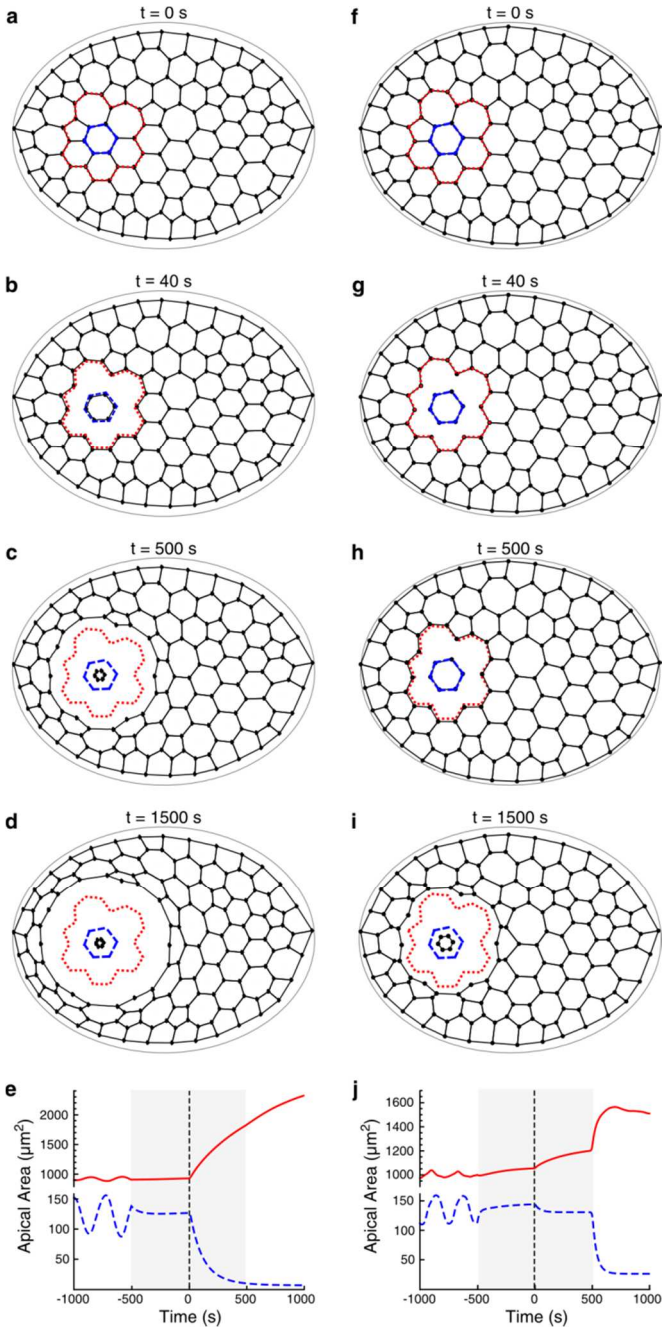

Figure 4.5: Simulations of cell-isolation experiments in CO_2-anesthetized embryos using the high-elastic-strain **a-e**, or low-elastic strain models **f-j**. CO_2 exposure was simulated by transiently suppressing all active contractions from -500 to +500 s. Overlays denote pre-ablation shapes of the isolated cell (*blue dashed*) and the outer boundary of the wound (*red dotted*). **e,j.** Area versus time for the wound (*red*) and the isolated cell (*blue dashed*) using each model. The shaded area denotes the time during which active contractions were suppressed.

4.4.3 3D shape changes associated with apical contraction cycles

Although both the experiments and their matching simulations imply pulsations of amnioserosa cells that are strongly cell autonomous, this autonomy requires what seems like a very strange mechanical situation: epithelial cells with a net internal force that is directed outwards, *i.e.*, an in-plane compressive stress. Two possible sources of this outward force are pressurization of the cell's cytoplasm or coupling between the apical and basal surfaces of the cell. We thus imaged the three-dimensional structure of pulsing amnioserosa cells using the Riselle-117 strain [12,42]. Three-dimensional reconstructions show that these cells are not rigidly prismatic in shape. Instead, there are considerable dynamic changes in the basal half of the cell (Figure 4.6), including wedging of the cell walls, formation of bulges, and rippling of the basal surface.

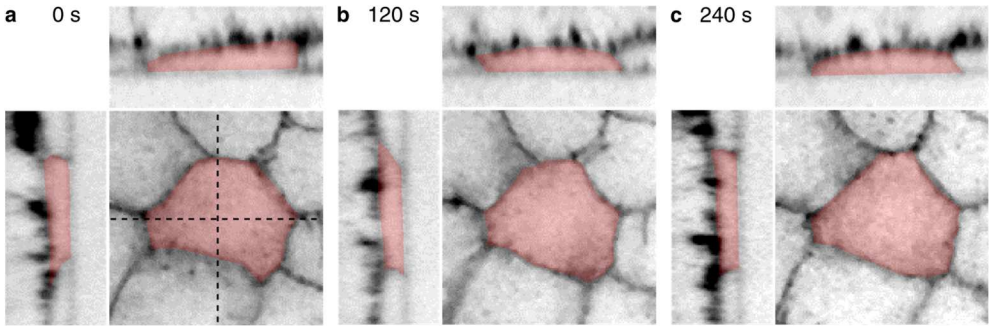

Figure 4.6: Three-dimensional view of dynamic changes in amnioserosa cell shape. The extent of one cell is highlighted in red. Three views are shown for each time point: an *xy*-view of the apical area (bottom right); an *xz*-cross-section (top); and a *yz*-cross-section (left). The rougher, outermost surface in each cross-section corresponds to the basal surface.

Although the complexity of these basal surface dynamics prevents us from discerning any strong correlations with the apical dynamics, there was no significant change in the total volume of each cell on the time scale of a single pulsation cycle. Volume pushed away from the apical surface during a constricted phase of the cycle is possibly collected in the basolateral domain and returned to the apical domain in the next half cycle. We are following up with a detailed analysis

of these 3D cell shape changes. For now, cytoplasmic pressure is but a plausible source for the compressive stress.

4.4.4 Conclusions

During dorsal closure, the cell shape oscillations of amnioserosa cells are mainly cell autonomous. Most importantly, the expansion phase of each cell's cycle is driven by cell-internal forces, not by the contraction of neighboring cells. Our results on amnioserosa cells isolated via laser-microsurgery are in agreement with observations of partially detached germband cells in α-catenin knockdowns. These cells also autonomously oscillate [25]. Both experiments show that individual cells can generate tensile and compressive forces to reshape their volume autonomously. Three-dimensional reconstructions of amnioserosa cells suggest that basolateral elasticity allows cytoplasm to be pushed away from the apical surface during constriction, and can help restore the cell to an equilibrium shape when an active contraction ends.

Despite the autonomy of these oscillations, the phasing of neighboring cells is coordinated (largely out-of-phase) by active stretch-induced contractions. Another active response drives the apical collapse of mechanically isolated cells and the recoil of cells surrounding a laser-induced wound. Both occur on the same time scale, both can be eliminated by CO_2 anesthesia, and both can be modeled as a single contact-dependent process. We do not know the exact biochemical trigger for this response, but it could be as simple as a lack of adhesions to neighboring cells.

Martin *et al.* [11] suggested a sub-cellular ratcheting model for driving apical constriction during invagination. It is possible that the stretch-induced contraction cycle in amnioserosa cells work in a similar fashion, incrementally modifying cytoskeletal structure and reducing equilibrium surface area. This cell-autonomous reshaping would work in conjunction with super-cellular structures, the effects of which have been measured in the past [14,15,33].

4.5 Experimental Methods

4.5.1 Fly strains and sample preparation

All microsurgical experiments were performed using a transgenic *Drosophila* strain expressing *E-Cad:GFP; Sqh:mCherry* (gift from A. Jacinto, Instituto de Medicina Molecular, Lisbon, Portugal). Additional experiments to investigate 3D cell shapes used *Resille*(117–2)-*GFP* [42] (gift from J. Zallen, Sloan-Kettering Institute, New York, NY). Embryos were collected and incubated until early-dorsal-closure stage (~24 hours at 15.5°C), dechorionated in a dilute solution of bleach and mounted dorsal-side down on a glass coverslip [29,34]. The mounted samples were then placed in a suitable sample holder for confocal imaging under a layer of halocarbon oil (#27, Sigma-Aldrich, St Louis, MO) and a gas permeable membrane (YSI, Yellow Spring, OH). In some experiments, fly embryos were anesthetized by temporarily replacing the air over the sample with water-vapor-saturated CO_2, or Ar.

4.5.2 Laser ablation and microscopy

All laser ablation experiments used a laser scanning confocal microscope (LSM 410/Axiovert 135TV, Carl Zeiss, Thornwood, NY) with an attached holographic UV laser ablation system [37]. This system simultaneously ablates multiple targeted points by diffracting single pulses from a Q-switched Nd:YAG laser (Minilite II, Continuum, Santa Clara, CA; 5-ns pulse-width, λ = 355 nm) using a spatial light modulator (PPM X8267, Hamamatsu Photonics K.K., Japan). Tissues were ablated and imaged as close to the apical surface as possible. All microsurgeries were carried out at pulse energies approximately 2-3× threshold to ensure consistent and repeatable ablation. Confocal images were obtained at 4 s/scan, at a resolution of 0.326 μm/pixel, using a 40×, 1.3 NA, oil-immersion objective.

Additional time-resolved 3D image stacks were obtained on a spinning disk confocal microscope (Eclipse Ti, Nikon Instruments, Melville, NY/Quorum WaveFX-X1, Ontario Canada) using a 40×, 1.3 NA, oil-immersion objective at 0.22 μm/pixel in-plane resolution, 0.5 μm between image planes and a time of 20 s between image stacks.

4.5.3 Image processing and analysis

We used ImageJ (NIH, Bethesda, MD) software for basic image processing tasks. To measure the area of cells, we used Seedwater Segmenter [43], a custom watershed-based segmentation software. The cell area data extracted from segmentation was imported into Mathematica 8.0 (Wolfram Research, Champaign, IL), and Fourier transformed to identify frequency components in the apical area oscillations. Since amnioserosa cells have been shown to pulse with a periodicity of ~ 240 s [14,39], we estimated the oscillation phase based on the highest-amplitude frequency component in the range from 1/150 to 1/300 s^{-1}. We limited our analysis to data sets with oscillation amplitude greater than 5% of the mean cell area. To estimate numerical derivatives, we used a 2^{nd}-order, 5-point Savitzky-Golay smoothing differentiation filter [44,45].

4.5.4 Computational models of amnioserosa pulsations

Our model is based on Solon *et al.* [14]. The model contains 80 tightly-packed polygonal cells. Each interior vertex has elastic links to three neighboring vertices and three cell centroids. Each exterior boundary vertex has elastic links to two neighboring vertices, two cell centroids and a fixed ellipse. The latter representing attachment to the surrounding lateral epidermis. The motion of each vertex is described by an ordinary differential equation containing passive spring-like terms for the elastic links and active force terms for the time-delayed stretch-induced contractions. For more details, see *Chapter 2,* Section 2.6. The set of ordinary, time-delayed

differential equations was solved numerically using Mathematica 8.0 (Wolfram Research, Champaign, IL).

4.6 Acknowledgements

This work supported by the National Science Foundation (IOB-0545679), the Human Frontier Science Program (RGP0021/2007C) and the National Institutes of Health (1R01-GM099107).

4.7 References

[1] D. Fristrom, Tissue and Cell **20**, 645 (1988).
[2] J. Bard, *Morphogenesis: The Cellular and Molecular Processes of Developmental Anatomy* (Cambridge University Press, 1992).
[3] J. Campos-Ortega and V. Hartenstein, *The Embryonic Development of Drosophila Melanogaster*, 2nd ed. (Springer, 1997).
[4] T. Lecuit and P.-F. Lenne, Nature Reviews Molecular Cell Biology **8**, 633 (2007).
[5] M. A. Wozniak and C. S. Chen, Nature Reviews Molecular Cell Biology **10**, 34 (2009).
[6] D. P. Kiehart, The Journal of Cell Biology **149**, 471 (2000).
[7] A. Jacinto, S. Woolner, and P. Martin, Developmental Cell **3**, 9 (2002).
[8] F. Schöck and N. Perrimon, Developmental Biology **248**, 29 (2002).
[9] D. Sweeton, S. Parks, M. Costa, and E. Wieschaus, Development **112**, 775–789 (1991).
[10] H. Oda and S. Tsukita, J. Cell. Sci **114**, 493 (2001).
[11] A. C. Martin, M. Kaschube, and E. F. Wieschaus, Nature **457**, 495 (2008).
[12] A. C. Martin, M. Gelbart, R. Fernandez-Gonzalez, M. Kaschube, and E. F. Wieschaus, The Journal of Cell Biology **188**, 735 (2010).
[13] N. Gorfinkiel, G. B. Blanchard, R. J. Adams, and A. Martinez Arias, Development **136**, 1889 (2009).
[14] J. Solon, A. Kaya-Çopur, J. Colombelli, and D. Brunner, Cell **137**, 1331 (2009).
[15] M. S. Hutson, Y. Tokutake, M. S. Chang, J. W. Bloor, S. Venakides, D. P. Kiehart, and G. S. Edwards, Science **300**, 145 (2003).
[16] D. P. Kiehart, Current Biology **9**, R602 (1999).
[17] A. Jacinto, A. Martinez-Arias, and P. Martin, Nat. Cell Biol. **3**, E117 (2001).
[18] N. Harden, Differentiation **70**, 181 (2002).
[19] B. E. Stronach and N. Perrimon, Development **128**, 2905 (2001).
[20] V. Hartenstein and Y. N. Jan, Roux's Archives of Developmental Biology **201**, 194 (1992).
[21] J. M. Abrams, K. White, L. I. Fessler, and H. Steller, Development **117**, 29 (1993).
[22] A. Jacinto, W. Wood, T. Balayo, M. Turmaine, A. Martinez-Arias, and P. Martin, Curr. Biol. **10**, 1420 (2000).
[23] A. Scuderi and A. Letsou, Developmental Dynamics **232**, 791 (2005).
[24] J. D. Franke, R. A. Montague, and D. P. Kiehart, Current Biology **15**, 2208 (2005).
[25] R. Fernandez-Gonzalez and J. A. Zallen, Physical Biology **8**, 045005 (2011).

[26] G. B. Blanchard, S. Murugesu, R. J. Adams, A. Martinez-Arias, and N. Gorfinkiel, Development **137**, 2743 (2010).
[27] D. J. V. David, A. Tishkina, and T. J. C. Harris, Development **137**, 1645 (2010).
[28] M. W. Berns, J. Aist, J. Edwards, K. Strahs, J. Girton, P. McNeill, J. B. Rattner, M. Kitzes, M. Hammer-Wilson, L. H. Liaw, A. Siemens, M. Koonce, S. Peterson, S. Brenner, J. Burt, R. Walter, P. J. Bryant, D. van Dyk, J. Coulombe, T. Cahill, and G. S. Berns, Science **213**, 505 (1981).
[29] D. P. Kiehart, Y. Tokutake, M. S. Chang, M. S. Hutson, J. Wiemann, X. G. Peralta, Y. Toyama, A. R. Wells, A. Rodriguez, and G. S. Edwards, in *Cell Biology: A Laboratory Handbook*, edited by J. E. Celis, 3rd ed. (Elsevier Academic, 2006), pp. 87–103.
[30] S. Kumar, I. Z. Maxwell, A. Heisterkamp, T. R. Polte, T. P. Lele, M. Salanga, E. Mazur, and D. E. Ingber, Biophysical Journal **90**, 3762 (2006).
[31] X. G. Peralta, Y. Toyama, M. S. Hutson, R. Montague, S. Venakides, D. P. Kiehart, and G. S. Edwards, Biophysical Journal **92**, 2583 (2007).
[32] M. Rauzi, P. Verant, T. Lecuit, and P.-F. Lenne, Nat Cell Biol **10**, 1401 (2008).
[33] R. Fernandez-Gonzalez, S. de M. Simoes, J.-C. Röper, S. Eaton, and J. A. Zallen, Developmental Cell **17**, 736 (2009).
[34] X. Ma, H. E. Lynch, P. C. Scully, and M. S. Hutson, Phys. Biol. **6**, 036004 (2009).
[35] J. Colombelli and J. Solon, Cell and Tissue Research (2012).
[36] R. Farhadifar, J.-C. Röper, B. Aigouy, S. Eaton, and F. Jülicher, Current Biology **17**, 2095 (2007).
[37] A. K. Jayasinghe, J. Rohner, and M. S. Hutson, Biomedical Optics Express **2**, 2590 (2011).
[38] M. S. Hutson, J. Veldhuis, X. Ma, H. E. Lynch, P. G. Cranston, and G. W. Brodland, Biophysical Journal **97**, 3075 (2009).
[39] D. Azevedo, M. Antunes, S. Prag, X. Ma, U. Hacker, G. W. Brodland, M. S. Hutson, J. Solon, and A. Jacinto, PLoS ONE **6**, e23964 (2011).
[40] Y. R. Kundomal and J. M. Baden, Toxicology Letters **25**, 287 (1985).
[41] N. H. Badre, M. E. Martin, and R. L. Cooper, Comparative Biochemistry and Physiology - Part A: Molecular & Integrative Physiology **140**, 363 (2005).
[42] X. Morin, Proceedings of the National Academy of Sciences **98**, 15050 (2001).
[43] D. N. Mashburn, H. E. Lynch, X. Ma, and M. S. Hutson, Cytometry Part A **81A**, 409 (2012).
[44] A. Savitzky and M. J. E. Golay, Analytical Chemistry **36**, 1627 (1964).
[45] W. H. Press, *Numerical recipes : The art of scientific computing* (Cambridge University Press, Cambridge, UK; New York, 2007).

CHAPTER 5

CAVITATION BUBBLE DYNAMICS STUDIED *IN VIVO*

5.1 Abstract

Pulsed laser microsurgery results in the formation of cavitation bubbles *in vivo* and in solution. Although these short-lived bubbles can cause noticeable deformations in post-ablation tissue, they cannot be directly imaged using confocal fluorescent microscopy. To study cavitation in *Drosophila* embryos, we have developed a high-speed bright-field imaging system capable of directly imaging bubbles *in vivo*. We find that the maximum extent of these bubbles is greater than might be inferred from the size of the laser-disrupted region of tissue.

We then use this system to investigate cavitation bubbles dynamics during multi-point laser ablation in solution. Bubbles formed at the center of extended multi-point patterns grow faster and larger than others in the pattern. Understanding the mechanisms driving this enhanced growth is necessary for avoiding unwanted side-effects of holographic laser ablation. The dynamics of highly-reproducible bubbles formed in solution suggest that it may be necessary to avoid highly-symmetric ablation patterns in microsurgical experiments.

5.2 Introduction

If a sufficiently energetic laser pulse is focused to a point inside a transparent material, explosive vaporization can result [1–6]. If this ablation point is close to the surface of the material, it drives an ablation plume, but if the target is inside the material, it instead creates a cavitation bubble [1,6]. This holds true for ablation in tissue as well as liquids. These cavitation bubbles may

be significantly larger than the initial plasma, and can affect a volume of tissue greater than that initially vaporized by the ablating laser [7–11].

Cavitation bubbles have lifetimes ranging from hundreds of nanoseconds to a few tens of microseconds; much too short to be seen with our typical imaging modality – confocal scans which take tens of milliseconds or longer to complete. Nonetheless, the growth of cavitation bubbles in tissue can have effects that last longer than the bubbles themselves. For example, when we use our holographic laser microsurgery system to generate ablation patterns containing multiple tightly-spaced points, confocal scans taken tens of seconds later show significant warping of the cell sheet surrounding the wound (Figure 5.1). This suggests that large cavitation bubbles created during multi-point ablation may exert pressure on the cells surrounding the ablation wound, deforming the tissue. To investigate this possibility we need to study the dynamics of cavitation *in vivo*.

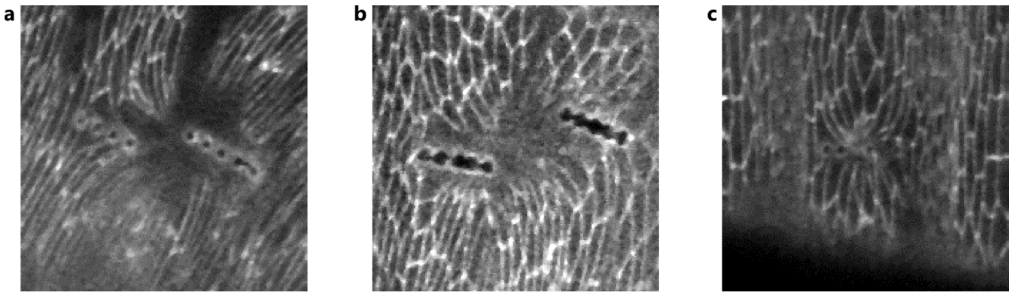

Figure 5.1: Confocal scans of the lateral epidermis of *Drosophila* embryos, taken approximately 60 s after ablation, show the effects of ablating lines of tightly spaced points. **a-b.** Undamaged cells appear to have been pulled towards a point between the pair of lines. **c.** Cells have been pulled towards the center of the single line.

The relatively opaque embryonic tissue makes it difficult to image cavitation bubbles *in vivo* using standard transmission microscopy. Instead of direct imaging, the maximum size of a single bubble may be inferred by either measuring its oscillation period, based on the relative delay between transient pressure waves created during plasma formation and bubble collapse [8,12], or by

observing the passage of the bubble wall past a fixed point [5,12]. Both of these methods assume spherically (or at least radially) symmetric expansion of a bubble, which may not hold true inside the confines of living tissue.

We thus developed a high-speed, bright-field imaging system specifically for imaging cavitation bubbles. This system uses a pulsed laser, with adjustable pulse-duration, to illuminate the sample from above the microscope objective. A high-sensitivity camera is used to image the variations in the brightness of the transmitted beam. Length of the illumination pulse is adjusted to suit the material and phenomena of interest. For example, we can image transient dynamics in transparent media by using short (~20 ns) illumination pulses, or we can use longer (~500 ns) pulses to increase contrast in more turbid systems and improve image quality. We then used this system to image bubbles formed by single-point and multi-point ablation in tissue and in liquid.

5.3 Materials and methods

Embryos used for imaging cavitation bubbles were dechorionated in a dilute bleach solution, glued to a glass coverslip, and covered with distilled water [12]. Using an uncovered layer of water, instead of our normal combination of hydrocarbon oil and an O_2-permeable membrane [13–15], improves the transmission characteristics of the illumination path. It also allows for the use of a needle hydrophone for measuring shockwaves produced during ablation. This setup does have a slight adverse effect on the quality of confocal images because the missing O_2-permeable membrane normally helps keep the curved surface of the embryo pressed against the coverslip.

Images formed by the bright-field imaging system lack all depth information. Each is essentially a picture of the shadows cast by structures in the ~200-μm thick embryo. Since it is not possible to

identify individual cells in these images, we don't use the bright-field system for targeting the ablation laser. Instead, we use confocal fluorescent images for targeting. Subsequent confocal images are used to assess the total area damaged by the ablation. The bright-field imaging system is used to measure the cross-sectional area of bubbles formed inside the embryo (Figure 5.2).

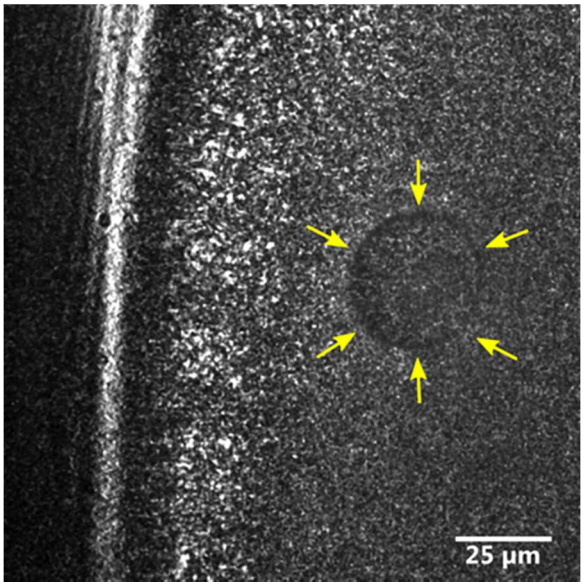

Figure 5.2: A single cavitation bubble (outlined by the yellow arrows) inside a *Drosophila* embryo, imaged 1 µs after ablation. The extreme edge of the embryo appears as a bright line on the left side of the image, and is ~100 µm above the plane of ablation.

As the ablation target for imaging cavitation in liquids we chose an ethanol solution of laser dye, with suitable spectral characteristics for use with our optical system (LD-390, Exciton, Dayton, OH; 0.56 g/L in reagent-grade ethanol, excitation wavelength = 355 nm, emission wavelength range = 378-398 nm). About 5 mL of this colorless solution is poured into a 30-mm diameter cylindrical holder with a #1.5 coverslip as its base. This holder is left uncovered to allow use of a needle hydrophone. Additional laser dye is added as necessary to compensate for evaporation.

The ablation threshold of this solution (264 nJ) is similar to that of embryonic tissue in *Drosophila* (215 nJ). Both are much less than that of deionized water (29.1 μJ), which has fewer quasi-free "seed" electrons, and thus requires a higher photon intensity for plasma formation [12]. We did measure some cavitation bubbles in deionized water and despite the difference in energy required for optical breakdown, above-threshold pulses result in similarly sized bubbles (Figure 3.2). The main advantage of a liquid with a low ablation threshold is the need for less energy to create a given ablation pattern. The lower threshold allowed us to generate patterns with as many as sixty points (Figure 5.3) without exceeding the damage threshold of the SLM.

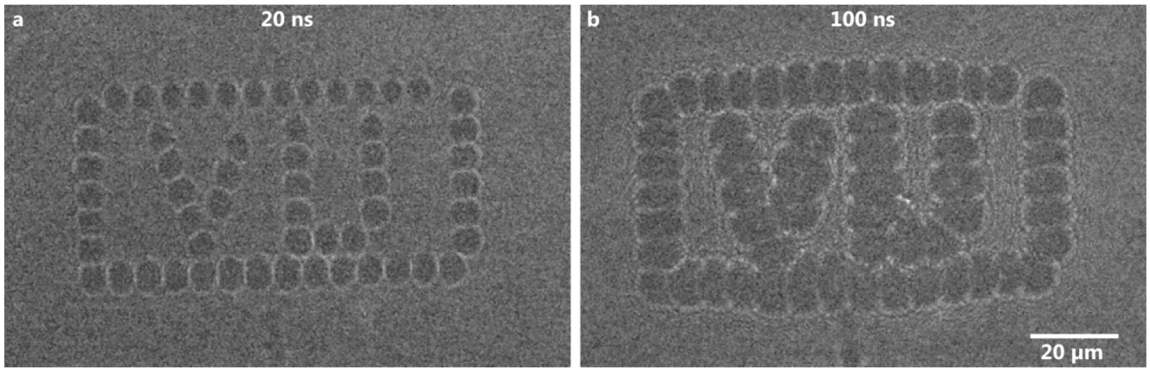

Figure 5.3: Pattern formed by 57 bubbles imaged using a 7-ns long illumination pulse. **a.** 20 ns after ablation. Individual bubbles are well defined. **b.** 100 ns after ablation. Some bubbles have started to merge and others have been displaced from their original position. The scale bar in *b* is common to both images. These images are taken with the shortest illumination pulses for which our system yields acceptable image contrast.

The uniformity of the laser dye solution yields reproducible cavitation with the shape and dynamics of a given bubble pattern depending only on the energy of the ablating laser pulse. Although our imaging system only takes one image per ablation event, this reproducibility enables the compilation of a representative image set showing cavitation bubble dynamics from initial formation to final dissipation. All we have to do is image bubbles created by different ablation pulses at different delay times. This same arrangement would not work as well in tissue, where each ablation would occur on a different embryo.

Figure 5.4 illustrates the use of this system to create a montage of images showing the growth, collapse and subsequent rebound of a single cavitation bubble. The delay between ablation and illumination increases in 100-ns steps starting from the moment of ablation – the equivalent of 10 million frames per second. The initial bubble has a 4-μs lifetime and a 13.5-μm maximum radius; the rebound bubble lasts for 1.5 μs, after which the remaining energy is dissipated into a cluster of much smaller bubbles.

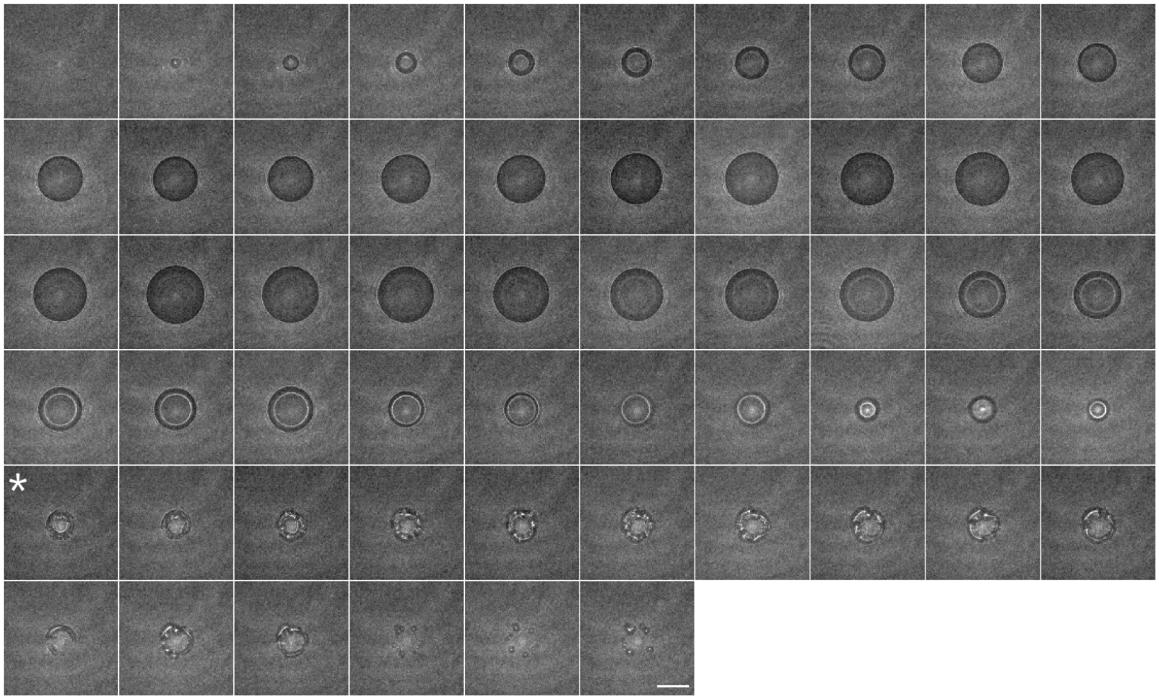

Figure 5.4: Dynamics of single-point cavitation bubbles in liquid, imaged using 20-ns long illumination pulses. The delay between ablation and illumination pulses was incremented in 100 ns steps from 0 to 5500 ns. The asterisk marks the first frame in which the rebound bubble is visible. The 20-μm scale bar is common to all images.

The ablation laser is focused to a plane approximately 10-15 μm inside the liquid. This depth is a compromise – deep enough to avoid damaging the glass coverslip, but shallow enough to allow plasma formation, which is limited by energy absorption in the laser dye before the focus. Note that the maximal bubble radius (~18 μm) in Figure 5.4 is greater than the maximum ablation depth. Bubbles formed within the range of accessible depths will unavoidably interact with the

coverslip. The interaction axis is parallel to the illumination axis, so we can't see the effects of this interaction using our current system. Similar and perhaps stronger interactions would take place during ablation of embryonic tissues, which are normally targeted at just 2-3 μm from the surrounding vitelline membrane.

5.4 Results and discussion

5.4.1 Cavitation in tissue

Previous research has shown, based on indirect measurements of maximum bubble radius, that cavitation bubbles produced during laser ablation are significantly larger than suggested by measurements of the laser-disrupted area [12,15]. To verify these results we compared images of cavitation bubbles formed *in vivo* with post-ablation confocal images of the targeted tissue.

Our bright-field system can take only one image per ablation event. Since we are interested in measuring the maximum size of the generated cavitation bubble, we set the delay between ablation and illumination pulses near half the bubble oscillation period, which yields an image of the bubble at close to its maximum radius. From hydrophone data, we know that the oscillation periods for cavitation bubbles formed at 2-3× ablation threshold are approximately 3-7 μs [12,15]. The larger bubbles formed during multi-point holographic ablation have longer lifetimes than those formed by single-point ablations [15].

Figure 5.5 compares bright-field images of cavitation bubbles and confocal images of the targeted cells after ablation at a single point (Figure 5.5a-b) or multiple points targeted holographically (Figure 5.5c-d). In both cases, the bubbles have asymmetric cross-sections and are much larger than the laser-disrupted area seen in subsequent confocal scans. Nonetheless, the diameter of the bubble, as measured along its largest dimension, is consistent with that implied

by its oscillation period using the Rayleigh formula [1,12,16,17]. This result is consistent with earlier comparisons of tissue damage and equivalent bubbles in liquid (Figures 3.4 and 3.5).

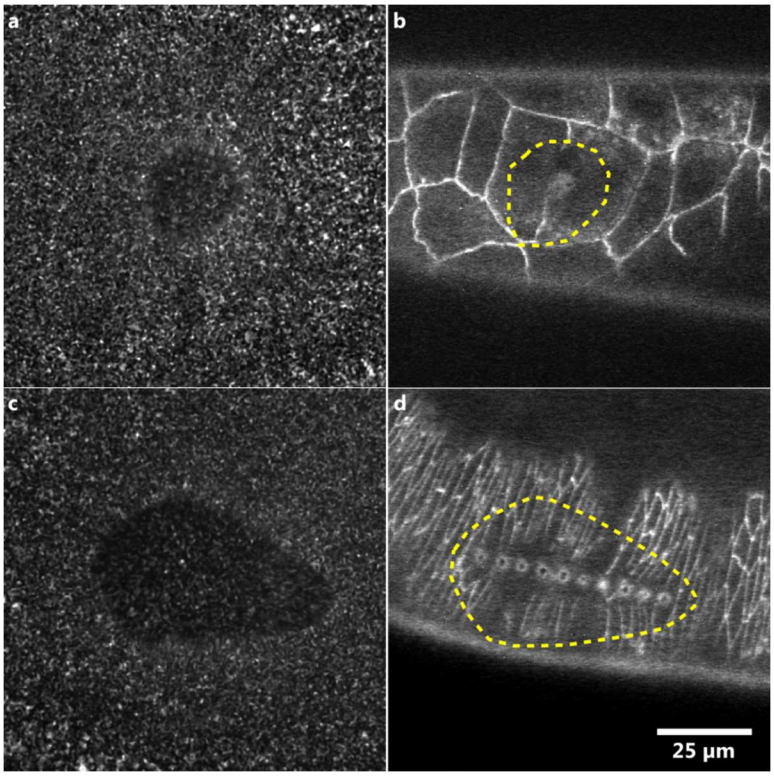

Figure 5.5: Cavitation bubbles formed during microsurgery are significantly larger than the damaged region of the tissue. **a.** Bright-field image of a single cavitation bubble formed during a laser-hole-drilling experiment in the amnioserosa. **b.** Confocal scan of the tissue post-ablation. The size and position of the bubble are shown outlined in yellow. **c** and **d.** Bright-field image of the cavitation bubble *(c)* and post-ablation confocal scan *(d)* from holographic ablation of a line in the lateral epidermis. Bright-field images were taken using a 500-ns long illumination pulse initiated 1 µs after ablation. Scale bar in *d* is common to all images.

The mismatch between observed bubble size and tissue damage suggests that the bubbles expand out of the plane of the tissue. This expansion is most likely into the perivitelline fluid filling the space between the tissue and overlying vitelline membrane, *i.e.*, following a path of least resistance. Expansion into this un-compartmentalized space would allow bubbles formed at different sites to interact and possibly affect tissue at points distant from those targeted.

Since the growth of bubbles *in vivo* is likely affected by differences in cellular geometry, and thus is not very reproducible, we turned to imaging cavitation bubbles formed in solution to study the interactions between ablation sites.

5.4.2 Jet formation during bubble collapse

During holographic microsurgery, interactions can occur among closely spaced bubbles. As part of our cell-isolation protocol [15], we use pairs of tightly spaced ablation points to cleave cell edges (Figure 3.4). The interaction between two such bubbles may result in jet formation [18,19], which may help in disrupting the cellular structures between these ablation sites [20]. To better understand the effects of paired ablation sites, we imaged the expansion and collapse of cavitation bubble pairs in solution (Figure 5.6).

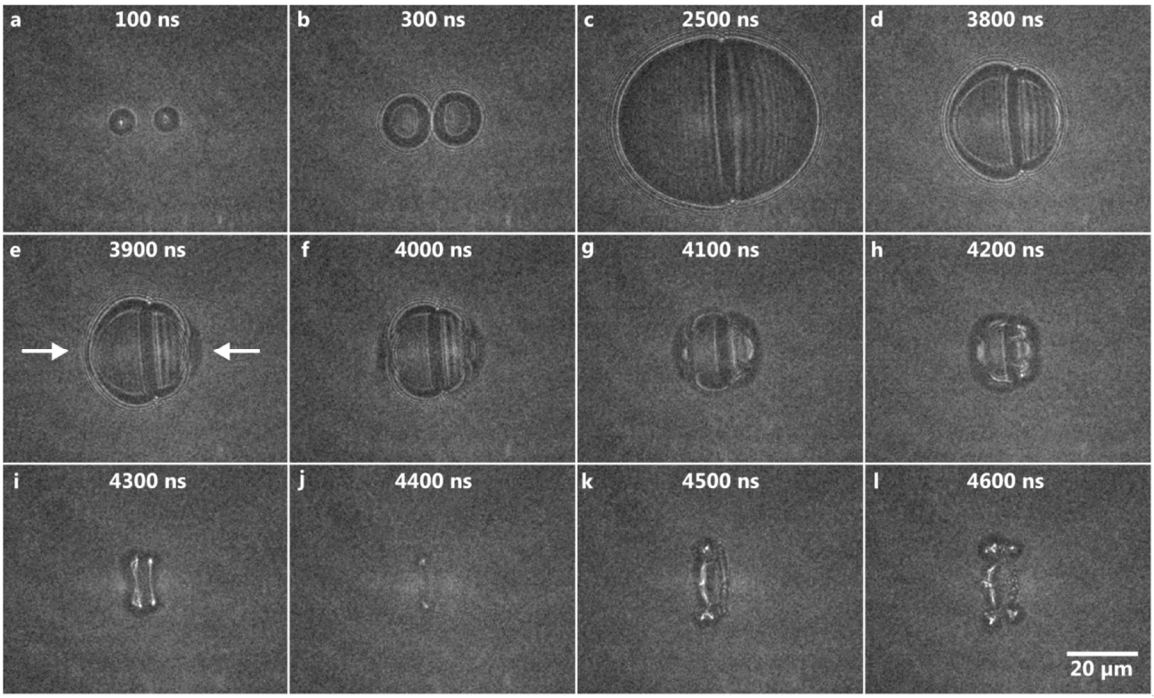

Figure 5.6: Dynamics of cavitation bubble pairs. **a-c.** The bubbles reach their maximum size near 2500 ns. **d-j.** The collapsing bubbles develop a pair of opposing jets. **k-l.** The rebounding bubbles develop along an axis perpendicular to that connecting the original ablation points. The arrows in *e* point to invaginations in the bubble walls indicating the formation of inward facing jets. The scale bar is common to all images. Bubbles were imaged using 20-ns long illumination pulses.

The bubbles, created 12.5 μm apart, grow to a maximum diameter of approximately 50 μm, but never merge (Figure 5.6a-c); a clearly defined interface remains visible at all times. The bubble walls opposite the interface invaginate as the two bubbles collapse (Figure 5.6d-i). This invagination, pointed to by the arrows in Figure 5.6e, is caused by that region of the bubble wall collapsing faster than the rest (Figure 1.8) [21]. This fast-moving portion of the bubble wall forms a jet extending through the bubble, and possibly through the opposite wall [19,21] (see also *Chapter 1, section 1.2.2.2*). After collapse of the initial bubbles, a line of smaller bubbles forms parallel to the previous interface (Figure 5.6j-l). Jets clearly do form between the targeted ablation sites; however the jets and the rebounding line of bubbles occupy a small volume compared to the cavitation bubbles' maximum extent.

5.4.3 Secondary cavitation

During holographic laser ablation experiments we often ablate multiple targets surrounding a patch of tissue. We thus investigated the effect multi-point ablation has on material in the center of such patterns. We started by observing the secondary effects caused by a ring of ablation points. This is an experiment analogous to that described by Kedrinskii (Figure 1.10) [22]. Figure 5.7 shows the evolution and secondary effects of a ring of 19 cavitation bubbles. An irregular cluster of small bubbles can be seen in the center of the ~50-μm diameter ring of laser-induced "primary" cavitation bubbles (Figure 5.7b-k). This central cluster reaches a maximum size of ~20 μm just 300 ns after ablation. A normally expanding single-point cavitation bubble would need ~2 μs to reach this size [17]. By 1000-ns after ablation, while the bubbles in the surrounding ring are still expanding, the bubbles at the center of the ring have collapsed, with a rebound bubble visible after 1500 ns (Figure 5.7l).

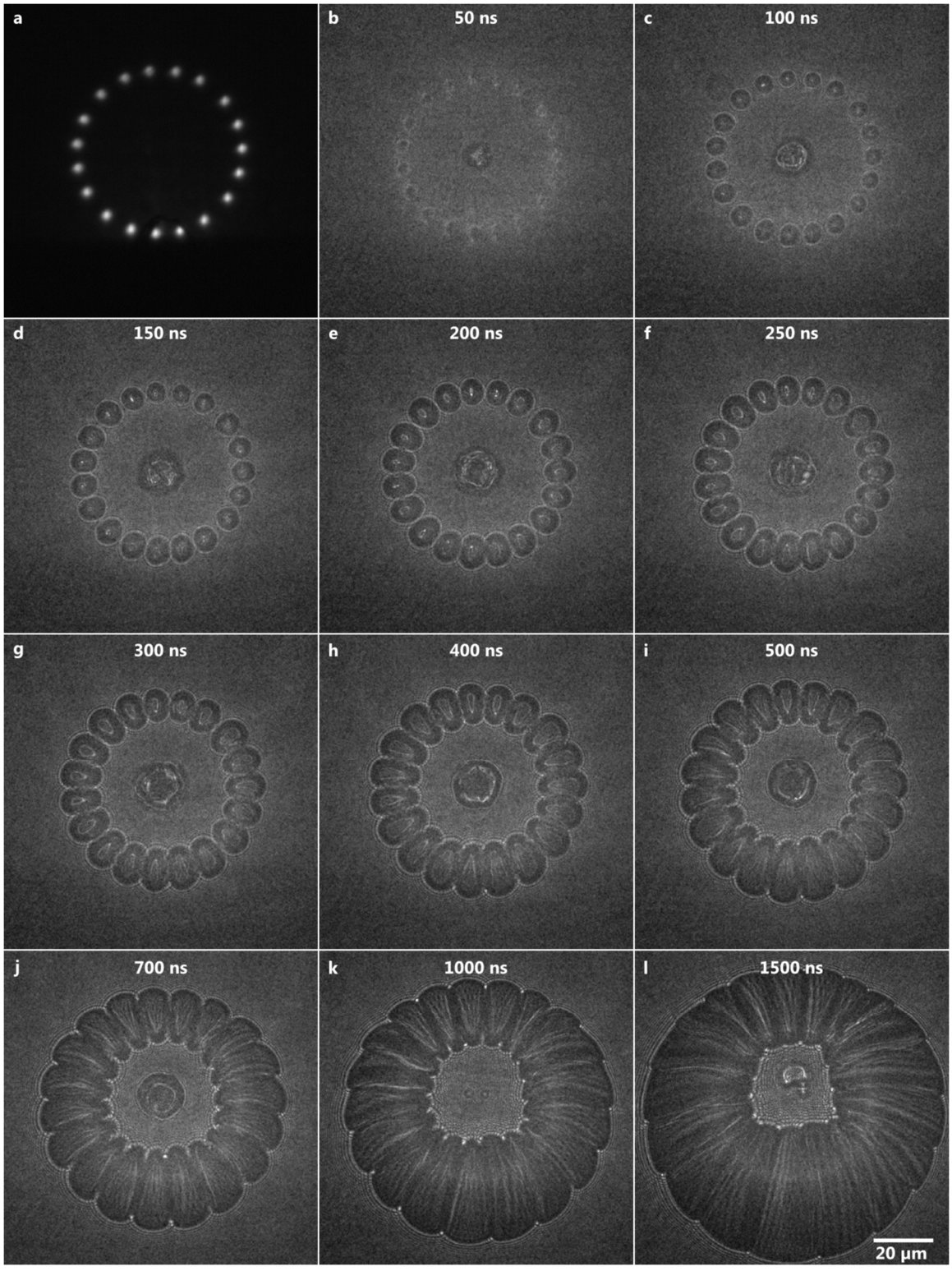

Figure 5.7: Rings of cavitation bubbles imaged using 20-ns illumination pulses. **a.** Pattern of fluorescent spots on white paper, created by the diffracted laser beam. Note that there is no fluorescence in the center of the ring. **b-l.** A short-lived cluster of bubbles appears in the center of the rapidly growing ring of cavitation bubbles, with a rebound of the cluster visible in *l*.

For comparison, we next observed the behavior of an additional primary cavitation bubble created at the center of a similar ring of bubbles (Figure 5.8). The central bubble grows significantly faster than those in the surrounding ring, reaching a radius of over 15 μm in less than 700 ns. At this point the bubbles have grown sufficiently to fill the space enclosed by the targeted circle (Figure 5.8j). As the bubbles in the surrounding ring continue to grow, the central bubble shrinks – at least in cross-section (Figure 5.8k-l). The central bubble's volume may be compressed by the surrounding bubbles, or pushed above the plane of ablation.

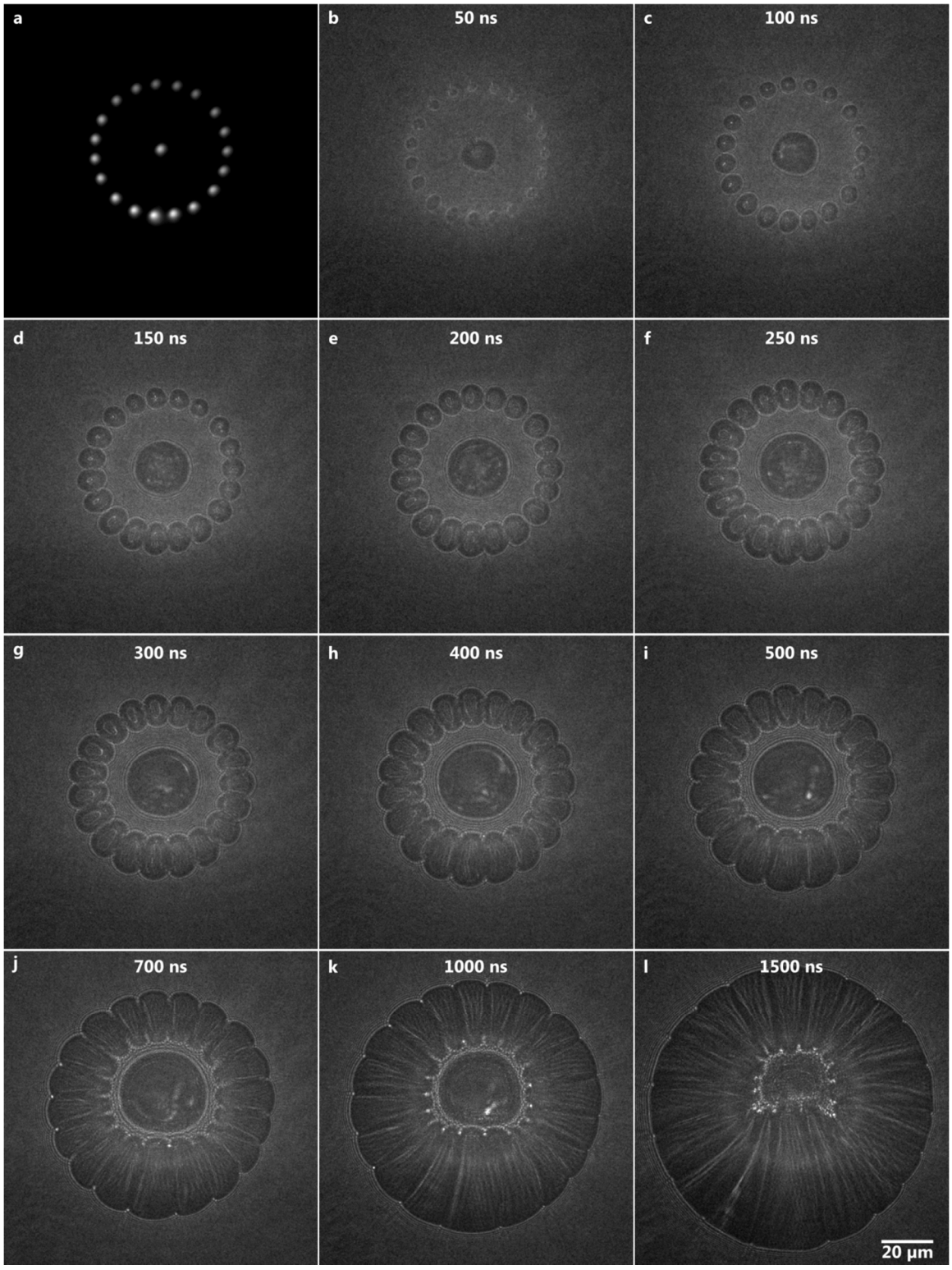

Figure 5.8: Growth of cavitation bubbles, the target pattern for which was a ring plus a central spot. **a.** Pattern of 20 fluorescent spots on white paper created by the diffracted laser beam. **b-i.** The surrounding ring of bubbles grows to contact the central bubble. **j-l.** The central bubble is displaced and squeezed by the surrounding bubbles.

Tensile stress in the targeted material can enhance the secondary effects of laser ablation. One mechanism by which such stresses may be induced is the interaction of multiple pressure waves creating tensile stress in the area where these waves intersect [23,24]. Another possibility is tensile (or rarefaction) waves created when a pressure wave is reflected from a free boundary [22]. These waves propagate towards the source of the initial pressure wave (see *Chapter 1, Section 1.2.2.3*) and, in the case of a circular pattern of ablation points, will converge at the center of the pattern creating a similar area of tensile stress. We observe cavitation starting approximately 30-40-ns after ablation, suggesting that reflected tensile waves are the more likely mechanism – a pressure wave travelling at the speed of sound in ethanol (~1.1 μm/ns) would reach the center of the approximately 18-nm radius ring of ablation points in less than 17 ns. However, it is possible that cavitation bubbles are initially too small to seen with our optical system, and are detected only after they grow or coalesce sufficiently.

Non-radially symmetric patterns have more nuanced, though still noticeable, effects. Figure 5.9 shows the growth of a 5×5 grid of cavitation bubbles. Even though the effect is not as pronounced as with a ring of bubbles, bubbles at the center of the grid grow noticeably faster. The bubble in the very center grows the fastest; bubbles in the middle row and column of the grid grow slightly slower, but still faster than the outer bubbles. Although each bubble in the pattern is affected by tensile waves, bubbles toward the center of the grid are affected by multiple such waves converging simultaneously, enhancing their growth.

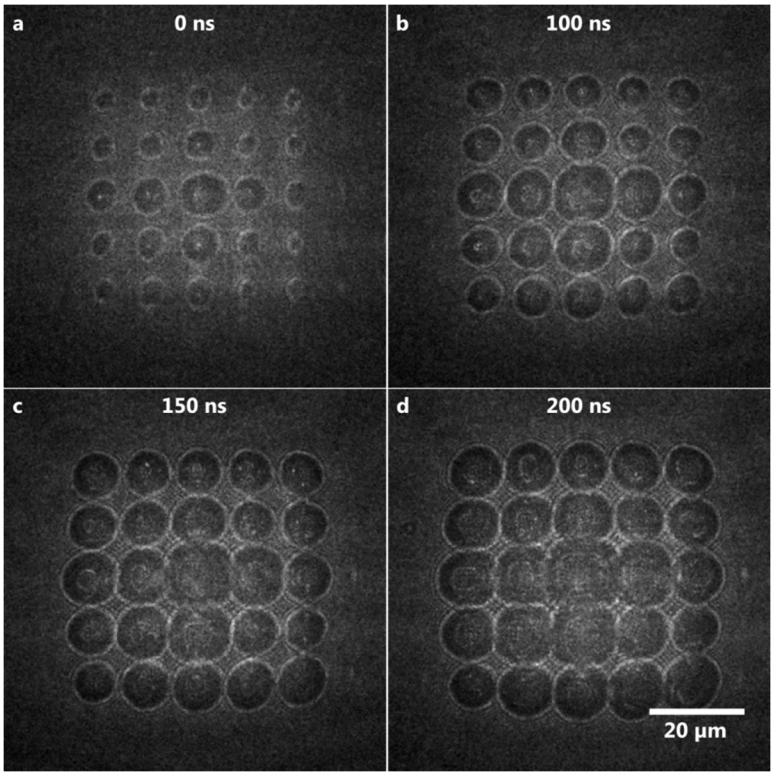

Figure 5.9: 5×5 array of ablation points, imaged using 20-ns illumination pulses. The scale bar is common to all images.

5.5 Conclusions

We have used a purpose-built high-speed bright-field imaging system to study the behavior of cavitation bubbles in liquids and in tissue. The size of the cavitation bubbles formed inside tissue is significantly larger than the region damaged (or even displaced), suggesting that the bubbles expand outside the targeted tissue, most likely in the space between the tissue and the outer vitelline membrane surrounding the embryo.

The dynamics of cavitation bubble patterns formed in liquid demonstrate that tensile waves, formed by shockwave-bubble interactions, can create a central low-pressure area. This effect can result in secondary cavitation, or rapid growth of centrally located laser-generated bubbles. This is

most noticeable in patterns that concentrate tensile waves, but any pattern with multiple closely spaced points is affected to some degree.

Two questions are raised by the images we have obtained using this bright-field imaging system. First, are cavitation bubbles formed *in vivo* expanding in the perivitelline space? Second, do the large bubbles formed in the center of multi-point ablation patterns press on intact tissue to create the deformation seen in confocal images (Figures 3.5 and 5.1)? Currently we can only image bubble dynamics on a plane perpendicular to the optical axis of the imaging system. To answer the above questions we need to add a third dimension to our images.

It may be possible to gain this additional information by using pairs of micro-mirrors placed either side of an embryo. The first mirror, facing the illumination laser at a 45° angle, would reflect light parallel to the coverslip and horizontally through the embryo. The second, facing the microscope objective at a same 45° angle, would reflect this light down to the camera. The pair would thus add two 90° bends to the path of the transmitted light. This would allow imaging on a plane perpendicular to the coverslip.

Although the dynamics of cavitation bubbles formed in a uniform liquid may differ from that of bubbles formed inside the complex, compartmentalized environment of an embryo, we can still use information gained from these images to optimize ablation patterns. By choosing the appropriate point spacing for a pattern, we can "tune" our microsurgical incisions to minimize damage to the surrounding tissue. Furthermore, by understanding the effects of cavitation during holographic laser ablation we can separate some side effects of the ablation process from the biomechanics of embryonic tissue.

5.6 References

[1] K. Y. Lim, P. A. Quinto-Su, E. Klaseboer, B. C. Khoo, V. Venugopalan, and C.-D. Ohl, Phys. Rev. E **81**, (2010).

[2] P. A. Quinto-Su, V. Venugopalan, and C.-D. Ohl, Opt. Express **16**, 18964 (2008).

[3] A. Vogel, K. Nahen, D. Theisen, and J. Noack, IEEE Journal of Selected Topics in Quantum Electronics **2**, 847 (1996).

[4] A. Vogel, S. Busch, and U. Parlitz, The Journal of the Acoustical Society of America **100**, 148 (1996).

[5] G. Paltauf and H. Schmidt-Kloiber, Appl. Phys. A **62**, 303 (1996).

[6] A. Vogel, J. Noack, K. Nahen, D. Theisen, S. Busch, U. Parlitz, D. X. Hammer, G. D. Noojin, B. A. Rockwell, and R. Birngruber, Applied Physics B: Lasers and Optics **68**, 271 (1999).

[7] A. Vogel, J. Noack, G. Hüttman, and G. Paltauf, Appl. Phys. B **81**, 1015 (2005).

[8] V. Venugopalan, A. Guerra, K. Nahen, and A. Vogel, Phys. Rev. Lett. **88**, (2002).

[9] A. Vogel and V. Venugopalan, Chem. Rev. **103**, 577 (2003).

[10] A. Vogel, S. Busch, K. Jungnickel, and R. Birngruber, Lasers in Surgery and Medicine **15**, 32 (1994).

[11] A. Vogel, R. Engelhardt, U. Behnle, and U. Parlitz, Applied Physics B Lasers and Optics **62**, 173 (1996).

[12] M. S. Hutson and X. Ma, Phys. Rev. Lett. **99**, 158104 (2007).

[13] X. Ma, H. E. Lynch, P. C. Scully, and M. S. Hutson, Phys. Biol. **6**, 036004 (2009).

[14] D. P. Kiehart, Y. Tokutake, M. S. Chang, M. S. Hutson, J. Wiemann, X. G. Peralta, Y. Toyama, A. R. Wells, A. Rodriguez, and G. S. Edwards, in *Cell Biology: A Laboratory Handbook*, edited by J. E. Celis, 3rd ed. (Elsevier Academic, 2006), pp. 87–103.

[15] A. K. Jayasinghe, J. Rohner, and M. S. Hutson, Biomedical Optics Express **2**, 2590 (2011).

[16] E. A. Brujan, K. Nahen, P. Schmidt, and A. Vogel, Journal of Fluid Mechanics **433**, 251–282 (2001).

[17] Lord Rayleigh, Philos. Mag. **34**, (1917).

[18] Y. Tomita, A. Shima, and K. Sato, Appl. Phys. Lett. **57**, 234 (1990).

[19] W. Lauterborn and C.-D. Ohl, in *In Fascination of Fluid Dynamics*, edited by A. Biesheuvel and G. F. Heijst (Springer Netherlands, Dordrecht, 1998), pp. 63–76.

[20] I. Toytman, A. Silbergleit, D. Simanovski, and D. Palanker, Phys. Rev. E **82**, (2010).

[21] C. E. Brennen, *Cavitation and bubble dynamics* (Oxford University Press, New York, 1995).

[22] V. Kedrinskii, *Hydrodynamics of Explosions. Experiments and Models* (Springer, Berlin;Heidelberg;New York, 2005).

[23] M. Frenz, G. Paltauf, and H. Schmidt-Kloiber, Physical Review Letters **76**, 3546 (1996).

[24] G. Paltauf, H. Schmidt-Kloiber, and M. Frenz, The Journal of the Acoustical Society of America **104**, 890 (1998).

CHAPTER 6

SUMMARY AND FUTURE DIRECTIONS

6.1 Summary

This dissertation describes the development of a new laser microsurgery tool for probing tissue mechanics *in vivo*, and its application in studying the forces driving dorsal closure in *Drosophila melanogaster* embryos. In addition, some possible secondary effects of multi-point ablation is discussed.

The new system is based upon a 2D spatial light modulator (SLM) operating in phase-only mode. The SLM is used to diffract a single pulse from a nanosecond UV laser to form a pattern of ablation points. This ablation system is tightly integrated with our confocal fluorescent microscope, allowing simultaneous imaging and ablation of tissue. The optical path of the ablating laser is designed to support both SLM based multi-point ablation and single-point ablation using a steering mirror to guide the laser beam.

New software was developed to control the SLM and calculate the kinoform needed to create the desired ablation pattern. This software is based on an implementation of the Gerchberg-Saxton algorithm, and accounts for the specific transfer characteristics of our optical path. The ablation system is used to target points in living tissue, and as such, the two main priorities in software design were uniformity of the output pattern and calculation speed.

This holographic ablation system enables a number of experiments that were not previously possible: studying the behavior of a single cell or small patch of cells isolated from surrounding tissue; investigating anisotropy in the forces developed in tissue during morphogenesis; and

measuring intra-embryonic variations in tension. As part of this research, I used this new system to isolate single amnioserosa cells and study the cell-autonomous forces involved in dorsal closure in *Drosophila*.

Analysis of cells isolated using holographic laser microsurgery suggests that the amnioserosa as a tissue relies on forces generated autonomously by individual cells. In particular, the reshaping of these cells' apical surfaces is driven by internally generated forces – both during contraction and expansion phases.

A computer model of the tissue was used to simulate the experiments. This model represents individual cells as a collection of vertices connected by a network of springs. Active contractile forces are represented by sigmoidal functions, which are triggered by specific events in the simulation. This modeling effort provided further evidence that individual cells in the amnioserosa are not under large elastic strains; and that internally generated contractile forces are responsible for the contraction in apical surface area observed post-isolation.

To investigate this cell-autonomous behavior further, *Drosophila* embryos were anesthetized using CO_2 gas. When embryos are anesthetized before ablation, the apical surface of amnioserosa cells retain their size and shape even after separation from the surrounding tissue. These cells only changed shape after CO_2 was removed and the embryo revived, demonstrating that the reshaping of isolated cells is an active process.

To investigate the effects of cavitation on tissue ablated the holographic laser microsurgery, I studied the growth of cavitation bubbles, both *in vivo* and in a laser dye solution, using a purpose-built, high-speed bright-field imaging system. Cavitation bubbles formed *in vivo* have a surprisingly large cross-section, much larger than the size of the laser-disrupted areas of tissue.

This suggests that the bubbles expand out of the tissue, possibly into the perivitelline fluid surrounding the embryo.

A significant concern with multi-point ablation is the possibility of adverse effects caused by interactions between multiple shockwaves and cavitation bubbles. Secondary cavitation effects are easily visible in high-speed images of cavitation bubble dynamics in liquids. These effects include: secondary cavitation at the center of an ablation pattern; more rapid growth of bubbles in the central areas of symmetric patterns; and jet formation during the collapse of a closely spaced pair of cavitation bubbles. Such effects are most noticeable in patterns that maximize the overlap of tensile waves created during ablation, but may also play a part in the post-ablation dynamics of tissue targeted using the simpler, yet more tightly-spaced ablation patterns we normally use for microsurgery. Understanding these secondary effects will be useful for designing optimal patterns for new ablation experiments.

Overall, the following conclusions can be reached from the described research.

- Holographic laser microsurgery is a useful technique for investigating the mechanics of morphogenesis *in vivo*.
- Using software designed specifically for speed and uniformity of output, it is possible to successfully target and ablate multiple points in living, dynamic tissue.
- The oscillatory behavior of amnioserosa cells during dorsal closure depends on forces generated autonomously within individual cells. In particular, the apical surface of each cell is reshaped by its internal forces. Intercellular forces play a smaller role.
- Passive elastic strain plays much smaller part in the dynamics of isolated cells than previously thought.

- This cell-autonomous behavior can be modeled using a network of springs to represent cell membranes and triggered, sigmoidal functions to represent the autonomously generated contractile forces.
- Multiple ablation events occurring in close proximity have interesting secondary effects that need to be accounted for in interpreting images of post-ablation tissue.

Holographic laser microsurgery is a useful new tool for probing the intra- and inter-cellular forces acting on tissue *in vivo*. The observed dynamics of ablated tissue can be used to guide the development of new computational models of morphogenesis. These new models may, in turn, suggest new microsurgical experiments for measuring the biomechanics of development. The knowledge gained from investigating dorsal closure will also be useful for modeling morphogenetic events such as palatogenesis and neural tube closure in the development of higher vertebrates.

6.2 Future directions

The results obtained from isolating single amnioserosa cells directed necessary modifications of an existing model that simulates some aspects of dorsal closure; however, this model does not yet fully describe the entire dorsal closure process. More sophisticated models are needed to account for such factors as variations in effective viscosity and tissue stiffness. The multi-point ablation system described in this work can be used to test and improve these new models.

The ablation system may also be used for a number of other experiments, for example, measuring the effects of instantaneously separating large parts of the amnioserosa from the lateral epidermis. Such an experiment would provide information on multi-cellular mechanical forces, complementing data obtained from single-cell experiments. The ablation pattern used for such an

extended incision would need to account for, and possibly minimize, the interactions between ablation points.

The ablation system can be optimized further to increase the targetable area and maximum number of ablation points. Our current system is designed to maintain flexibility and compactness, sacrificing targetable area and reducing the total energy delivered to the ablation plane. One could improve the system's performance by using optical elements designed to work specifically with 355-nm light.

Finally, further investigation is needed into the growth of cavitation bubbles *in vivo*. By using micro-mirrors to bend the illumination path for the high-speed bright-field imaging system, it may be possible to resolve the position and size of these bubbles in three dimensions; and providing information about the possible expansion of bubbles outside the targeted tissue.

APPENDIX A

INTERPLAY OF WAVELENGTH, FLUENCE AND SPOT-SIZE IN FREE-ELECTRON LASER ABLATION OF CORNEA

M. Shane Hutson[1-3*], Borislav Ivanov[1], Aroshan Jayasinghe[1], Gilma Adunas[1], Yaowu Xiao[1], Mingsheng Guo[4], John Kozub[2]

[1]Department of Physics & Astronomy, [2]W.M. Keck Vanderbilt Free-electron Laser Center and [3]Vanderbilt Institute for Integrative Biosystem Research & Education, Vanderbilt University, Nashville, TN 37235, USA
[4] Department of Physics, Fisk University, Nashville, TN 37208, USA

This work was published in *Optics Express*, Vol. 17, Issue 12, pp. 9840-9850 (2009).

A.1 Overview

The research presented in the following work was performed at the W. M. Keck Free-Electron Laser Center, Vanderbilt University, Nashville, TN, in 2008 and early 2009.

I designed and performed all plume imaging experiments, and several of the experiments designed to measure etch depth in cornea. In addition I wrote some of the utility software used with the automated beam-profile measurement apparatus.

A.2 Abstract

Infrared free-electron lasers ablate tissue with high efficiency and low collateral damage when tuned to the 6-μm range. This wavelength-dependence has been hypothesized to arise from a multi-step process following differential absorption by tissue water and proteins. Here, we test this hypothesis at wavelengths for which cornea has matching overall absorption, but drastically different differential absorption. We measure etch depth, collateral damage and plume images and find that the hypothesis is not confirmed. We do find larger etch depths for larger spot sizes – an effect that can lead to an apparent wavelength dependence. Plume imaging at several wavelengths and spot sizes suggests that this effect is due to increased post-pulse ablation at larger spots.

A.3 Introduction

Infrared free-electron lasers (FELs) can ablate soft biological tissues with high efficiency and remarkably little collateral damage. This is particularly true when an FEL is tuned to the 6-μm wavelength range [1]. For some tissues, the optimal wavelength is 6.1 μm [2] – corresponding to the overlapping peaks of the amide I vibrational mode of proteins and the bending mode of

water. For others, it is 6.45 μm [1, 3] – corresponding to the tail of the water bending mode and the peak of the amide II vibrational mode of proteins. For others, it is closer to 6.0 μm [4]. In all tissues examined, both peaks were superior to wavelengths near 3.0 μm – corresponding to the peak of the water OH stretching mode. This last observation is not without controversy. Other lasers operating near 3.0 μm can also ablate soft tissues efficiently and with little collateral damage [5-8]. Nonetheless, the Vanderbilt FEL has been used to carry out eight successful human surgeries [9, 10]; and tabletop lasers in the 6-μm range are under development to translate this success to more widespread surgical use [11, 12].

Our current understanding of this wavelength-dependence is based on the fact that the 6-μm range directly targets protein vibrations [13-15]. Researchers have long hypothesized that such direct excitation could lead to a loss of protein structural integrity [1]. This structural failure should then allow tissue removal to occur at lower energy densities and a smaller pressure head, i.e. more efficiently and with less collateral damage. The hypothetical loss of structural integrity has two main difficulties. First, photon energies in the 6-μm range are quite low (~0.2 eV), so a photochemical mechanism is unlikely. Second, heat diffusion between a tissue's structural collagen fibers and the surrounding water is expected to take place on quite short time scales – just a few ns for the 30-nm diameter fibers in cornea. Thus, an FEL macropulse is much too long (3-5 μs) to confine the deposited energy to its original water or protein compartment, i.e. too long to achieve microscale thermal confinement [16].

On the other hand, the macropulse-width is not the only relevant time scale. Previous studies of FEL ablation considered fluences up to 200× the ablation threshold [1], where tissue removal begins well before the end of a macropulse [17, 18]. In such cases, partial microscale thermal confinement could be achieved during times prior to the onset of vaporization. This idea has been

modeled quantitatively by considering differential absorption by tissue water and collagen fibrils, heat diffusion between the two, and the temperature-dependent chemical kinetics of water vaporization and collagen denaturation [13-15]. This differential-absorption/partial-confinement model suggested a plausible mechanism for the original hypothesis: at high fluence, tissue water can begin explosive vaporization on the 10-100 ns time scale; during this time, partial thermal confinement leads to wavelength-dependent, protein-vs.-water temperature differentials; these in turn lead to wavelength-dependent collagen denaturation – amplified by the exponential dependence of chemical kinetics on -1/*T* [13]. By the time explosive vaporization begins, the wavelength-dependent accumulation of denaturated collagen determines whether the tissue structural matrix is strong and ductile or weak and brittle. In support of this model, recent experiments have confirmed wavelength-dependent denaturation and fragmentation of tissue collagen [19, 20]. This model also successfully predicted that the FEL ablation metrics should be only weakly dependent on the FEL micropulse intensity [13, 21, 22]. The most important remaining prediction is the interplay between the wavelength-dependence and macropulse intensity [15]. At low intensities, the differential heating of water and protein is washed out by heat diffusion – microscale thermal confinement is not achieved prior to vaporization – leading to predicted ablation metrics that are independent of the targeted chromophore. As the intensity increases, partial microscale thermal confinement is achieved and differential heating drives larger and larger protein-water temperature differences – leading to the prediction of an increasingly strong wavelength-dependence. For the geometry of cornea and for wavelengths with similar absorption as at 6.45 μm, the targeted chromophore is predicted to become important above 3×10^6 W/cm^2 [14, 15]. In this report, we test this prediction of a coupled wavelength and intensity dependence and find that it is not confirmed by experiments. Interestingly, we do find a spot-size dependence in the metrics that can masquerade as wavelength dependence.

A.4 Materials and methods

Corneas were obtained from sacrificed pig eyes within 24 hours post-mortem, swabbed with ethanol to remove the epithelial layer, and washed with distilled water to remove any contaminant on the surface. For each tissue sample, a strip of cornea and sclera (approximately 5×1 cm) was affixed over the internal opening of a metal substrate (razor blade) using cyanoacrylate glue applied to the edges of the strip. Special care was taken to ensure uniform tension on the sample and avoid any wrinkling of the surface. Corneal samples were periodically sprayed with saline, with the excess carefully blotted away, to maintain normal hydration. The thickness of the cornea was measured with a micrometer caliper.

A.4.1 Laser parameters

The Vanderbilt Mark-III FEL has a complex pulse structure in which 3-5 μs long macropulses are delivered at 1-30 Hz [23]. Each macropulse is composed of a micropulse train: 1-ps long pulses at a repetition rate of 2.85 GHz. Note that all references to fluence in this report correspond to macropulse fluence. For each experiment, the FEL is tuned to a specific wavelength in the range 2-9 μm (with linewidth $\Delta\lambda/\lambda \sim 2\%$ FWHM). Measurements were conducted at a pulse repetition rate of 30 Hz (except single-pulse plume imaging).

At the experimental end station, the FEL exits an evacuated beam transport system with a $1/e^2$ radius from 5-10 mm (wavelength-dependent) and a Rayleigh range in excess of 10 m. The beam is steered by three 3"-diameter silver-coated mirrors and traverses a large-aperture shutter (Uniblitz VS35S27M1, Vincent Associates, Rochester, NY), a wire-grid polarizer for fine energy control, an adjustable iris aperture, a CaF_2 pickoff window that sends a small fraction of the beam (~10%) to an energy meter (Ophir PE50BB, Ophir-Spiricon, Logan, UT), and a planoconvex lens to focus the beam (CaF_2, nominal f = 10, 15, 25 or 50 cm at λ = 5 μm; all optics from ISP Optics,

Irvington, NY). A second energy meter was placed behind the sample. In some experiments, the wire grid was replaced with a Brewster angle polarizer.

A.4.2 Beam profile measurements

The intensity profile of the FEL beam was measured at multiple locations near the focus using a knife-edge technique. Measurements were made in two orthogonal directions at several points along the beam to calculate the focal plane, minimum beam waist and Rayleigh length. The FEL pulse energy was kept at 0.5 mJ during the profile measurement to avoid damage to the razor blade's edge.

A.4.3 Etch depth measurements

Cornea samples were positioned such that the sample surface was at the FEL focal plane. These samples were generally thinner than the Rayleigh range of the focused beam (except for f = 10 cm). Each measurement consisted of measuring the number of pulses required to perforate the sample – detected by an energy meter placed behind the sample. The pre-perforation pulses were counted and measured by sending a small fraction of every pulse to a calibrated energy meter. Each perforation was conducted at a fresh spot on the sample, with a spot separation of 1 mm in both directions. Five to eight such perforations were measured for each set of laser parameters (wavelength, pulse energy and focused beam radius). The mean etch depth per pulse is the corneal thickness divided by the average number of pulses required for perforation. The results were subjected to nonlinear regression in Origin (OriginLab Corporation, Northampton, MA) and statistical analysis in Mathematica (Wolfram Research, Champaign, IL).

A.4.4 Histology for collateral damage analysis

Samples were mounted as above and most were exposed to FEL macropulses at a rate of 30 Hz while the sample was translated at 0.3 mm/s – resulting in a long, linear crater. For other samples, a linear crater was created by exposure to a fixed number of pulses at one location, translation by approximately half a beam diameter, and repeated exposure, with the cycle repeated dozens of times. Six to eight lines were cut into each cornea, with different macropulse fluence for each line. Ablated samples were fixed, imbedded in paraffin and sectioned at 6-μm intervals perpendicular to the tissue surface and the linear incision. Sections were mounted on 1×3 inch glass slides and stained with hematoxylin and eosin.

The crater morphology and zone of thermal injury were examined by bright-field microscopy. The darker areas along the edges of the crater are regions of thermal collateral damage [22]. The extent of these regions was quantified using ImageJ (NIH, Bethesda, MD). We first thresholded the contiguous dark region along the crater borders and then analyzed its thickness from 10% to 90% of the crater depth. The resulting distributions of collateral damage thickness were characterized in terms of their mean, median and quartile boundaries.

A.4.5 Plume imaging

Samples were mounted as described above, and the pulse energy was adjusted to maintain a constant fluence of 15 J/cm^2. The ablation plume was imaged perpendicular to the FEL beam path using a nitrogen laser (LN1000, Laser Photonics LLC, Lake Mary, FL) coupled to a rhodamine dye module (Laser Photonics LN102) to produce a 4 ns pulse of light at λ = 644 nm. To reduce laser speckle and improve image quality, the laser was coupled into a 1-km long multimode optical fiber. A 25-mm planoconvex lens collimated the output from the fiber to produce a beam that passed in front of, and parallel to, the sample stage. The resulting image was focused onto the

sensor of a color CCD camera (AVT Dolphin F145C, Allied Vision Technologies, Stadtroda, Germany) using a 105-mm zoom lens (Nikkor Telephoto AF, Nikon Co., Tokyo, Japan). A digital delay/pulse generator (SRS DG535, Stanford Research Systems, Sunnyvale, CA) and custom-built synchronization circuit were used to set the delay between the ablation and illumination lasers [22].

A.5 Results

To test the differential-absorption/partial-confinement model, we ablated porcine corneas with the FEL at a variety of wavelengths, spot-sizes and fluence. The chosen wavelengths were 2.77, 3.32, 5.97, 6.26 and 6.45 μm – five wavelengths for which cornea has matching absorption coefficients, but which differentially target protein and water (Table A.1). Among these wavelengths, the model predicts no chromophore-dependence for the ablation metrics at low macropulse intensity – $< 3 \times 10^6$ W/cm^2, equivalent to a fluence of 15 J/cm^2 [15] – and an increasingly strong dependence at high fluence. In the high-fluence regime, wavelengths that target protein are predicted to have higher ablation efficiency and lower collateral damage. The experiments below cover a wide range of fluence, 5 to 250 J/cm^2, and examine the ablation process in terms of etch depth, collateral damage and plume images.

Table A.1: Effective absorption coefficient, α, for FEL irradiation of corneal stroma [a] – including estimates for its water and protein components.[b]

Wavelength (μm)	$1/\alpha_{cornea}$ (μm)	$1/\alpha_{protein}$ (μm)	$1/\alpha_{water}$ (μm)	$\alpha_{protein}/\alpha_{water}$
2.77	5.4	20.1	4.8	0.24
3.32	5.4	7.0	5.2	0.74
5.97	5.2	3.4	5.7	1.7
6.26	5.1	3.0	5.8	2.0
6.45	5.9	1.7	10.1	5.8

[a]Based on a Gaussian-weighted average over the FEL linewidth (FWHM = 2% λ) using spectra from [15].
[b]Assumes a composite corneal spectrum representing 85% water and 15% protein by volume.

A.5.1 Etch depth

As a first test, we measured the mean etch depth per pulse δ as a function of wavelength λ and single-pulse fluence Φ. Even within the matched set of wavelengths, the slope of $\delta(\Phi)$ is highly chromophore-dependent. As shown in Figure A.1a, the slope is much larger for the wavelengths that predominantly target protein modes (5.97, 6.26 and 6.45 μm). This larger slope indicates higher ablation efficiency.

At first glance, the data appear to strongly confirm the model predictions; however, these data were collected using a single focusing lens. The wavelength is thus tightly coupled with the focal spot size ($w = 1/e^2$ radius at the beam waist). To decouple λ and w, we collected additional data with different focal-length lenses. In some instances, we further varied w by placing a variable aperture before the lens. In this second data set, the slope of $\delta(\Phi)$ is highly spot-size-dependent – even for a single wavelength. Results for λ = 2.77 μm are shown in Figure A.1b. At the largest beam radius, this water-targeting wavelength has higher ablation efficiency than any of the protein-targeting wavelengths, but at the smallest beam radius, its efficiency is $1/10^{th}$ as high. For protein-targeting wavelengths, the efficiency also decreases at smaller spot sizes, but in a much less drastic manner. One can see this effect in Figure A.1a. Within the scatter of protein-targeting

data, those points corresponding to the largest, middle and smallest spot sizes are on the corresponding high side, middle and low side of the range (open squares, circles and triangles respectively).

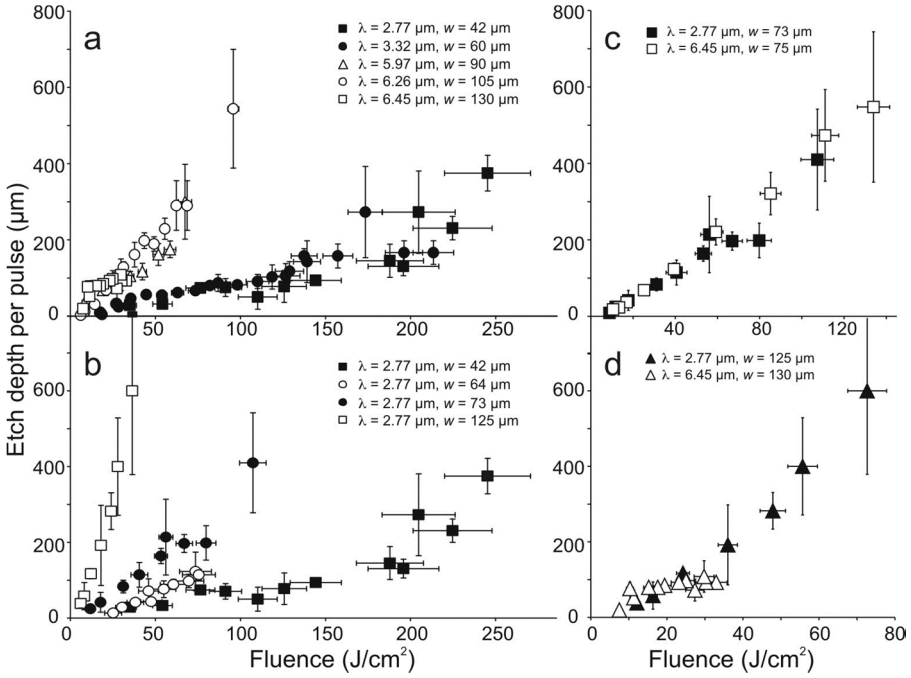

Figure A.1: Wavelength, fluence and spot-size dependence of the mean etch depth per pulse. **a.** Several wavelengths with matched absorption coefficients. Each wavelength was focused with the same lens and thus has a different $1/e^2$ radius at the beam waist (w, noted in the legend). Open (closed) symbols are used for predominantly protein- (water)-targeting wavelengths. **b.** A single wavelength focused with several different lenses to yield different spot-sizes. **c, d.** Two wavelengths with distinct differential absorption, but closely matched spot sizes. Error bars correspond to ± one standard deviation.

These observations raise an important question: how much of the apparent λ-dependence in Figure A.1a can be attributed to a coupled spot-size dependence? As a first test, we directly compare etch-depth measurements at different λ, but closely matched spot sizes. Even for the two wavelengths that appear most different in Figure A.1a, 2.77 and 6.45 μm, measurements of $\delta(\Phi)$ overlap strongly when both wavelengths are focused to w ~ 75 μm (Figure A.1c). An overlap also occurs at larger matched spot sizes (w ~125 μm), but we only have comparable data for $\Phi <$

40 J/cm^2. At the high end of this range, the measurements hint at some wavelength differences. We do not have direct comparisons for w < 70 μm.

As a second test, we used linear regression to estimate the slope, or ablation efficiency, of $\delta(\Phi)$ for each w and λ in Figure A.1 plus several additional data sets (23 total). The efficiencies were then subjected to an analysis of covariance (ANCOVA) to determine whether there is a significant λ-dependence above and beyond the obvious spot-size dependence. ANCOVA was carried out using one factor – whether the wavelength dominantly targets protein or water – and one covariate, either $F(w) = w$ or w^2. This makes the fitted model $a + bF(w) + c^*target$, where $target$ = 0 for protein-targeting wavelengths and $target$ = 1 for water-targeting wavelengths. As expected, we find a highly significant dependence of ablation efficiency on either w or w^2 ($P = 5 \times 10^{-4}$ or 2×10^{-4}). The data do not provide tight enough constraints to decide between these two forms of w-dependence; however, once the variance attributable to either $F(w)$ is removed, there is no remaining dependence on the targeted chromophore (P_{target} = 0.35 when $F(w) = w$; 0.38 when $F(w) = w^2$).

Despite capturing the trends in ablation efficiency, linear regression provides poor fits for those $\delta(\Phi)$ data sets that have obviously negative second derivatives (e.g. λ = 6.45 μm and w = 130 μm in Figure A.1d). To better parameterize all the etch depth data, we used nonlinear regression with a phenomenological Hibst model [24]:

$$\delta(\Phi) = \frac{\Phi_{th}}{\gamma \rho h_{abl}} \ln\left[1 + \gamma\left(\frac{\Phi - \Phi_{th}}{\Phi_{th}}\right)\right] \qquad (1)$$

where ρ is the tissue density (1.062 g/cm^3), Φ_{th} is the threshold fluence, h_{abl} is the heat of ablation and γ varies between 0 and 1. In the original Hibst formulation, $\rho h_{abl}/\Phi_{th} = \mu_a$ was the tissue absorption coefficient and γ was a measure of plume shielding; however, one should not over-

interpret the fitting results [24]; γ is best considered an indicator of whether $\delta(\Phi)$ behaves more like a blow-off model ($\gamma = 1$) or a steady-state model (limit $\gamma \to 0$). In either case, $1/(\rho h_{abl})$ is a measure of ablation efficiency and corresponds to the slope of $\delta(\Phi)$ just above threshold. The fitted parameters are plotted versus spot-size in Figure A.2. As the spot becomes more tightly focused, h_{abl} increases – quite rapidly for $2w < 150$ μm. Note that an increase in h_{abl} corresponds to a decrease in the slope of $\delta(\Phi)$, so this is another way to capture the spot-size dependence evident in Figure A.1. Tighter focus also increases Φ_{th} (Figure A.2b), but there is no obvious trend for γ.

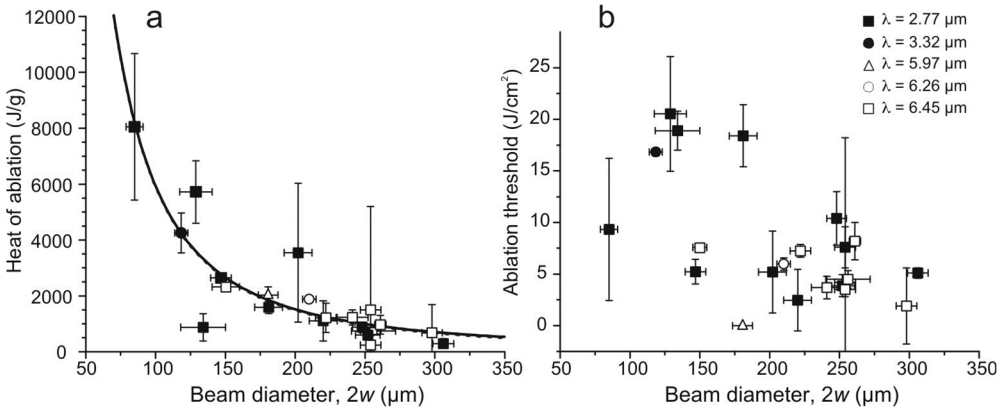

Figure A.2: Wavelength and spot-size dependence for the Hibst model parameters: **a.** heat of ablation; **b.** threshold fluence. Open (closed) symbols are used for predominantly protein-(water)-targeting wavelengths. The error bars denote 95% confidence limits. The two overlapping lines in A correspond to the best fits from ANCOVA with a $1/w^2$ covariate.

The Hibst parameters were also subjected to ANCOVA, but with inverted covariates, either $F(w) = 1/w$ or $1/w^2$. We find a very significant dependence of h_{abl} on $1/w^2$ ($P = 9 \times 10^{-8}$). One could make a similar statement with regard to $1/w$, but that best fit yields an unphysical result – specifically $h_{abl} < 0$ at large spot sizes. In any case, once the variance attributable to spot-size is removed, there is again no remaining dependence on the targeted chromophore ($P_{target} = 0.94$ for $F(w) = 1/w^2$). This result is shown graphically in Figure A.2a, where the best-fit curves for each factor level strongly overlap – so strongly that it is difficult to see the two lines separately ($a = 54 \pm 430$ J/g, b

= 15 ± 1.9 × 10^6 J μm^2/g and c = -34 ± 450 J/g). From these results, we conclude that the apparent λ-dependence in Figure A.1 is really just a proxy for an underlying w-dependence.

Similar ANCOVA for Φ_{th} is much less definitive. It indicates a slightly significant dependence on $1/w^2$ (P = 0.02), and a slightly insignificant dependence on the targeted chromophore (P_{target} = 0.07). In the entire set of etch depth data, this borderline result is the only one with any dependence on the targeted chromophore.

A.5.2 Collateral damage

As a second test, we measured thermomechanical collateral damage after ablating corneas at 2.77 and 6.45 μm, the two matching wavelengths with the largest difference in differential absorption. Noting the significant w-dependence above, we initially limited these experiments to matching 50-μm spot sizes at the tissue surface. The minimum beam waist was still λ-dependent – 36 versus 50 μm at λ = 2.77 or 6.45 μm respectively – so the tissue surface was positioned about 400 μm from the 2.77-μm beam waist. The fluence was thus matched at the tissue surface, but differed by a factor of two when averaged over the tissue thickness.

At either λ, higher fluence led to increased collateral damage (Figure A.3). The increased damage is most notable near the tissue surface and at the invaginations/tears in the crater wall. We measured the thickness of collateral damage, Δ, at each position from 10-90% of the crater depth and compiled a collateral damage distribution for each λ and Φ. The mean, median and quartile boundaries of the Δ-distributions are plotted in Figure A.3c. At low fluence, the mean damage widths are significantly different with 1.4× more damage at λ = 2.77 μm (P = 1 × 10^{-4} at 25 J/cm^2 and P = 3 × 10^{-5} at 50 J/cm^2, two-tailed t-test). As Φ increases, the λ-dependence disappears. This fluence-dependence is opposite to the trends predicted by the differential-absorption/partial-confinement model. Note that the damage levels observed here are certainly larger than those

obtained by other lasers in cornea [25], and by the FEL in softer tissues like brain [1]. We are not evaluating the utility of the FEL for cornea surgery, but using cornea as a model tissue for investigating ablation mechanisms.

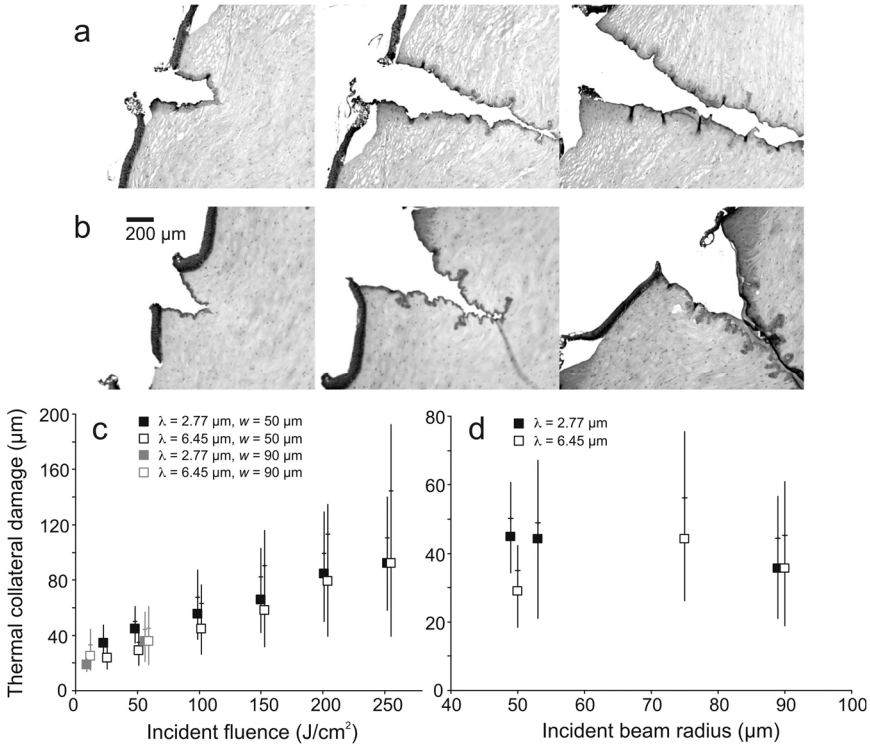

Figure A.3: Wavelength, spot-size and fluence dependence of thermomechanical collateral damage. **a.** Selected histological images after FEL ablation of cornea at λ = 2.77 μm, *w* = 50 μm, and Φ = 50, 100 and 200 J/cm^2 (respectively from left to right). **b.** Similar images after ablation at the same spot size and fluence with λ = 6.45 μm. **c.** Collateral damage versus fluence for matched spot sizes. Most points correspond to *w* = 50 μm. Exceptions are in grey and had *w* = 90 μm. **d.** Collateral damage at matched fluence (50-60 J/cm^2) for different spot sizes. For each set of conditions, the distribution of collateral damage thickness is characterized by its median value (*squares*), mean value (*horizontal dashes*) and 1st to 3rd quartile boundaries (*vertical lines*).

To see if there was any *w*-dependence, we also measured the Δ-distributions for larger 90-μm spots. As shown in Figure A.3c, the damage widths at both spot sizes generally fall along the same trend versus fluence. Interestingly, at the larger spot size, the damage width no longer has a significant λ-dependence at low fluence (P > 0.1 at both 12 and 60 J/cm^2). In Figure A.3d, we

compile the Δ-distributions for several experiments with similar fluence (50-60 J/cm^2), but variable spot sizes. The damage has no clear trend with either λ or *w*.

Importantly, these same histological images confirm a *w*-dependence for the etch depth. Using just three pulses at λ = 2.77 μm, Φ = 60 J/cm^2 and *w* = 50 or 90 μm, the larger spot size yielded craters that were >3× deeper (680 ± 190 versus 180 ± 60 μm). In both cases, the crater width was approximately twice the spot diameter.

A.5.3 Plume imaging

As a final metric and as a way to investigate the observed spot-size effects, we took images of the ablation plume from 300 ns to 1 ms after the start of the FEL pulse. Image sets were collected for λ = 2.77 and 6.45 μm with three different lenses (*f* = 15, 25 and 50 cm) and with the pulse energy adjusted to yield a constant fluence of 15 J/cm^2. In each case, the images revealed a pressure wave followed by a vapor/particulate plume (Figure A.4). The plume was clearly evident by 2-3 μs – well before the end of the FEL macropulse – and dissipated within 100 μs. In a few cases, the 30- and 100-μs images showed a secondary plume from recoil-induced ejection (e.g. 30-μs panel for λ = 6.45 μm and *f* = 50 cm). The images are very similar to those observed from many examples of photothermal ablation – including ablation of water with an FEL; however, water ablation yielded a longer-lasting plume with much more secondary ejection [22].

We find no discernable λ- or *w*-dependence for the particulate content of the initial plume, for the speed of the pressure wave (332 ± 14 m/s) or for the initial expansion rate of the plume (156 ± 13 m/s). The only observable that did vary was the likelihood of secondary ejection. This likelihood increased with spot-size. At Φ = 15 J/cm^2, secondary ejection was always evident for *w* > 100 μm, but was only evident in 1 of 4 experiments with smaller spots.

A.6 Discussion

We have measured the etch depth and collateral damage for FEL ablation of cornea over a range of λ, *w* and Φ. These measurements do not confirm the predictions of the differential-absorption/partial-confinement model. The ablation efficiency, or slope of $\delta(\Phi)$, is predicted to have a strong dependence on the targeted chromophore at high fluence (>15 J/cm^2), but we find no dependence – once one controls for spot-size effects. The chromophore-dependence of collateral damage is similarly predicted to diverge at high fluence, but we find a convergence. Collateral damage actually increases more quickly with increasing fluence at 6.45 μm. Although previous experiments found a strong λ-dependence for collagen denaturation and fragmentation [19, 20], these chemical modifications do not translate here into different ablation metrics. Note that these experiments only contradict predictions based on partial microscale thermal confinement prior to the onset of vaporization [13-15]. Other researchers have previously tested and confirmed predictions based on complete microscale thermal confinement (using shorter pulse lasers and tissues with larger collagen fibers) [26].

Interestingly, the ablation metrics presented here clearly depend on fluence and spot-size. At constant *w*, both etch depth and collateral damage increase with fluence. At constant Φ, etch depth decreases as spot-size decreases, but collateral damage does not change. The fluence dependence is as expected, but the spot-size dependence is a bit surprising. Although similar spot-size effects have been noted in a few instances [27-29], most ablation studies implicitly assume that making constant fluence comparisons eliminates spot-size effects. In the present data, that assumption is clearly not valid.

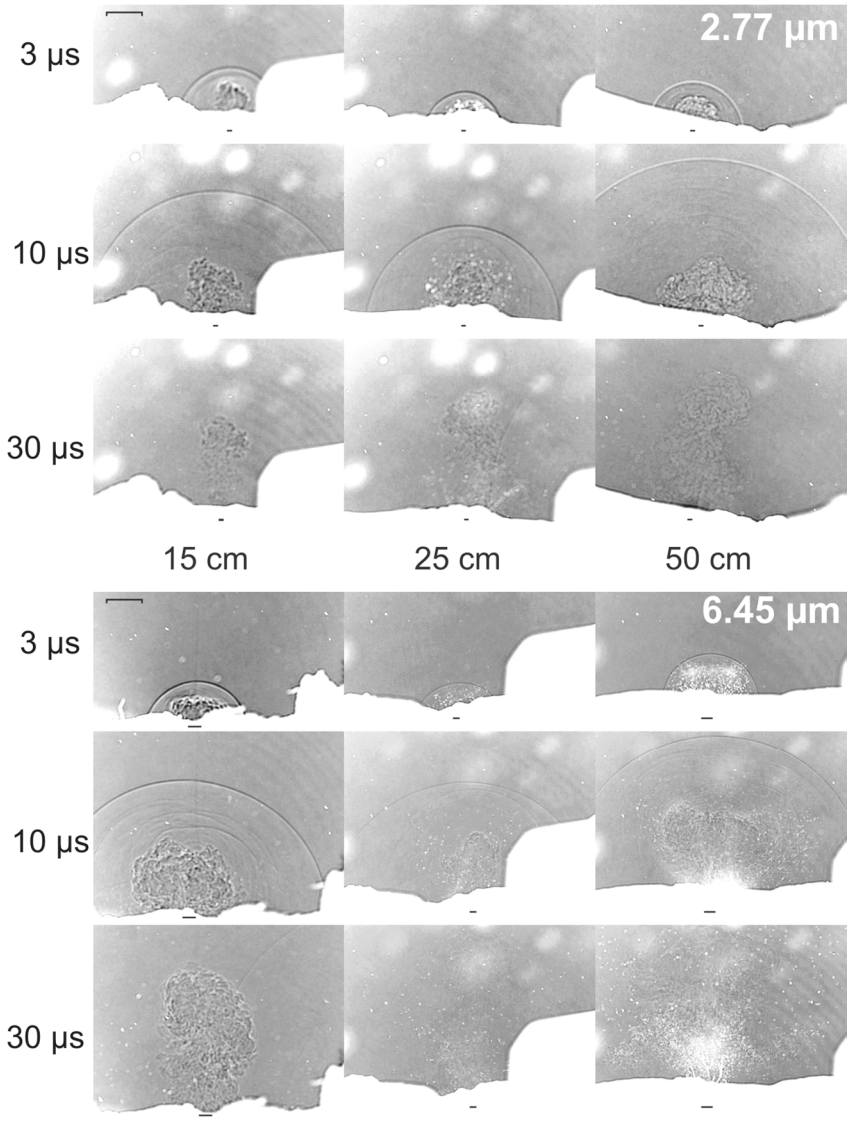

Figure A.4: Bright-field images of the pressure wave and vapor/debris plume during FEL ablation of cornea at Φ = 15 J/cm^2 and λ = 2.77 µm (*top*) or 6.45 µm (*bottom*). Each 3×3 set of images has columns for different focusing lenses (nominal *f* = 15, 25 and 50 cm) and rows for different times after the rising edge of the laser pulse (3, 10 and 30 µs). The scale bar at the top left of each image group represents 1 mm. The horizontal bar at the bottom center of each image denotes the measured beam diameter at the tissue surface.

The data presented here on spot-size dependence are not sufficient to pinpoint an exact mechanism. The literature contains many theoretical and empirical examples of spot-size dependencies in ablation, for example: scattering of more photons out of tightly focused spots [30]; increased plume shielding at larger spots [31, 32]; increased loss of energy density in small

spots due to heat conduction [33];influence of tissue curvature on the pressure head needed to stretch the tissue to tensile failure [34]; and influence of crater aspect ratio on the hydrodynamics of post-pulse ablation [35-37].

We can reasonably eliminate mechanisms A-C: scattering is unlikely to play a large role for mid-IR wavelengths; plume shielding typically decreases ablation efficiency at large spots – opposite to what we observe; and heat diffusion in the radial direction is unlikely to have any impact when tissue removal occurs on times much shorter than the radial thermal diffusion time (<100 μs compared to 10-200 ms for the spot-sizes used here). Mechanism D is also difficult to justify. A larger pressure head should drive larger initial plume velocities; however, we observe plume velocities with no *w*-dependence. As for mechanism E, some models of post-pulse or recoil-induced ablation predict a spot-size dependence opposite to that observed [37], but empirical observations show that larger spot sizes lead to longer post-pulse ablation [24, 35] – which in turn increases ablation efficiency [36]. Our plume images confirm more post-pulse ablation at larger spot sizes; and our crater images show signs of tearing along the crater walls, as often happens when recoil-induced ejection is somewhat constrained by a mechanically strong tissue [38]. Interestingly, two previous FEL ablation experiments reported wavelength-dependent differences in the post-pulse pressure transients [17, 18]. In both cases, the results support the finding here that larger spot sizes lead to more post-pulse ablation. At this point, we consider the primary candidate mechanism to be the hydrodynamics of post-pulse ablation. This effect may be exacerbated by the high aspect ratio craters created here.

Regardless of mechanism, we observe a spot-size and fluence dependence that can conspire to make an apparent wavelength-dependence – particularly when using a single lens and working at a tight beam focus (w < 100 μm). If pulse energy is constant, then longer wavelengths have a

smaller fluence, which leads to similar etch depths, but less long-λ collateral damage. If fluence is constant, then the spot-size effects lead to similar collateral damage, but higher long-λ ablation efficiency. The latter effect is evident in Figure A.1a where wavelength really serves as a proxy for spot size. Note that both combinations lead to better ablation performance at longer wavelengths. These effects could have influenced previous FEL experiments that compared wavelengths at different spot sizes, but there are also FEL experiments that used large, uniform spot sizes by positioning the tissue surface well away from the beam waist [2, 21, 22, 39, 40].

Even with these potential complications, our results confirm that FEL pulses in the 6-μm wavelength range do ablate tissue cleanly and efficiently. We do find conditions under which these FEL wavelengths ablate cornea with less collateral damage than other wavelengths. On the other hand, our results also show that λ = 3.32 or 2.77 μm can ablate tissue just as well, simply by adjusting the spot size. This observation is consistent with the known ablation capabilities of Er:YAG and Er:YSSG lasers at λ = 2.94 and 2.79 μm [5-8]. We do not know if the converse is true, i.e. whether the performance of 6-μm lasers will suffer at more tightly focused spots. We also do not know if these trends will hold in more surgically relevant tissues, particularly mechanically weak tissues like brain. Each of these questions will need further investigation as development proceeds on tabletop replacements for the FEL [11, 12].

A.7 Acknowledgements

The authors thank Prof. Glenn Edwards for reviewing an early version of the manuscript and the staff of the W. M. Keck Vanderbilt Free-electron Laser Center for generously providing beam time and expertise to this project. This work was supported by: grants FA9550-04-1-0045 and FA9620-

00-1-0370 from the DoD Medical FEL Program; NSF/HRD grant No. 0420516 (CREST); and by the NSF Center for Biophotonics, managed by U.C. Davis, CA No. PHY0120999.

A.8 References and links

[1] G. Edwards, R. Logan, M. Copeland, L. Reinisch, J. Davidson, B. Johnson, R. Maciunas, M. Mendenhall, R. Ossoff, J. Tribble, J. Werkhaven, and D. O'Day, Nature **371**, 416-419 (1994).
[2] J. I. Youn, P. Sweet, G. M. Peavy, and V. Venugopalan, Lasers Surg. Med. **38**, 218-228 (2006).
[3] K. M. Joos, J. H. Shen, D. J. Shetlar, and V. A. Casagrande, Lasers Surg. Med. **27**, 191-205 (2000).
[4] R. A. Hill, Q. Ren, D. C. Nguyen, L. H. Liaw, and M. W. Berns, Lasers in Medical Science **13**, 219-226 (1998).
[5] R. Kaufmann, and R. Hibst, Lasers Surg. Med. **19**, 324-330 (1998).
[6] R. Cubeddu, C. Sozzi, P. Taroni, G. Valentini, G. Bottiroli, and A. C. Croce, Lasers in Medical Science **12**, 21-30 (1997).
[7] T. S. Alster, Lasers Surg. Med. **24**, 87-92 (1999).
[8] J. Kiefer, T. Tillein, Q. Ye, R. Klinke, and W. Gstoettner, Otol. Neurotol. **25**, 400-409 (2004).
[9] G. S. Edwards, R. H. Austin, F. E. Carroll, M. L. Copeland, M. E. Couprie, W. E. Gabella, R. F. Haglund, B. A. Hooper, M. S. Hutson, E. D. Jansen, K. M. Joos, D. P. Kiehart, I. Lindau, J. Miao, H. S. Pratisto, J. H. Shen, Y. Tokutake, A. F. G. van der Meer, and A. Xie, Rev. Sci. Instrum. **74**, 3207-3245 (2003).
[10] M. L. Copeland, R. J. Maciunas, and G. S. Edwards, *Neurosurgical Topics: Advanced Techniques in Central Nervous System Metastases*, R. J. Maciunas, ed. (The American Association of Neurological Surgeons, Park Ridge, IL, 1998).
[11] G. S. Edwards, R. D. Pearlstein, M. L. Copeland, M. S. Hutson, A. Latone, A. Spiro, and G. Pasmanik, Opt. Lett. **32**, 1426-1428 (2007).
[12] M. A. Mackanos, D. Simanovskii, K. M. Joos, H. A. Schwettman, and E. D. Jansen, Lasers Surg. Med. **39**, 230-236 (2007).
[13] M. S. Hutson, S. A. Hauger, and G. Edwards, Phys. Rev. E **65**, 061906 (2002).
[14] G. S. Edwards, and M. S. Hutson, J. Synchrotron Radiat. **10**, 354-357 (2003).
[15] M. S. Hutson, and G. S. Edwards, *26th International Free Electron Laser Conference and 11th FEL Users Workshop* (Trieste, Italy, 2003) paper: FRAIS01.
[16] V. Venugopalan, N. S. Nishioka, and B. B. Mikic, Biophys. J. **70**, 2981-2993 (1996).
[17] J. Tribble, D. C. Lamb, L. Reinisch, and G. Edwards, Phys. Rev. E **55**, 7385-7389 (1997).
[18] W. Wagner, A. Sokolow, R. D. Pearlstein, and G. S. Edwards, Appl. Phys. Lett. **94**, 013901 (2009).
[19] Y. W. Xiao, M. S. Guo, K. Parker, and M. S. Hutson, Biophys. J. **91**, 1424-1432 (2006).
[20] Y. Xiao, M. Guo, P. Zhang, G. Shanmugam, P. L. Polavarapu, and M. S. Hutson, Biophys. J. **94**, 1359-1366 (2008).
[21] M. A. Mackanos, J. A. Kozub, and E. D. Jansen, Phys. Med. Biol. **50**, 1871-1883 (2005).
[22] M. A. Mackanos, J. A. Kozub, D. L. Hachey, K. M. Joos, D. L. Ellis, and E. D. Jansen, Phys. Med. Biol. **50**, 1885-1899 (2005).
[23] J. M. J. Madey, J. Appl. Phys. **42**, 1906-1930 (1971).
[24] A. Vogel, and V. Venugopalan, Chem. Rev. **103**, 577-644 (2003).

[25] W. B. Telfair, C. Bekker, H. J. Hoffman, P. R. Yoder, R. E. Nordquist, R. A. Eiferman, and H. H. Zenzie, J. Refract. Surg. **16**, 40-50 (2000).
[26] B. P. Payne, N. S. Nishioka, B. B. Mikic, and V. Venugopalan, Lasers Surg. Med. **23**, 1-6 (1998).
[27] Y. Domankevitz, M. S. Lee, and N. S. Nishioka, Appl. Opt. **32**, 569-573 (1993).
[28] U. S. Sathyam, A. Shearin, and S. A. Prahl, Proc. SPIE-Int. Soc. Opt. Eng. **2391**, 336-344 (1995).
[29] U. S. Sathyam, A. Shearin, E. A. Chasteney, and S. A. Prahl, Lasers Surg. Med. **19**, 397-406 (1996).
[30] R. R. Anderson, and J. A. Parrish, J. Invest. Dermatol. **77**, 13-19 (1981).
[31] B. Wolff-Rottke, J. Ihlemann, H. Schmidt, and A. Scholl, Appl. Phys. A **60**, 13-17 (1994).
[32] M. Eyett, and D. Bauerle Appl. Phys. Lett. **51**, 2054-2055 (1987).
[33] F. Partovi, J. A. Izatt, R. M. Cothren, C. Kittrell, J. E. Thomas, S. Strikwerda, J. R. Kramer, and M. S. Feld Lasers Surg. Med. **7**, 141-154 (1987).
[34] B. Majaron, P. Plestenjak, and M. Lukac, Appl. Phys. B **69**, 71-80 (1999).
[35] A. Vogel, I. Apitz, and V. Venugopalan in *Oscillations, Waves and Interactions*, T. Kurz, U. Parlitz, and U. Kaatze, eds. (Universitätsverlag Göttingen, Göttingen, 2007), pp. 217-258.
[36] I. Apitz, and A. Vogel, Appl. Phys. A **81**, 329-338 (2005).
[37] A. D. Zweig, J. Appl. Phys. **70**, 1684-1691 (1991).
[38] J. P. Cummings, and J. T. Walsh, Appl. Opt. **32**, 494 (1993).
[39] J. I. Youn, P. Sweet, and G. M. Peavy, Lasers Surg. Med. **39**, 332-340 (2007).
[40] J. M. Auerhammer, R. Walker, A. F. G. van der Meer, and B. Jean, Appl. Phys. B **68**, 111-119 (1999).

APPENDIX B

RAMAN-SHIFTED ALEXANDRITE LASER FOR SOFT TISSUE ABLATION IN THE 6- TO 7-μM WAVELENGTH RANGE

John Kozub[1], Borislav Ivanov[1], Aroshan Jayasinghe[1], Ratna Prasad[2], Jin Shen[2], Marc Klosner[3], Donald Heller[3], Marcus Mendenhall[1], David W. Piston[1,4,5], Karen Joos[2], M. Shane Hutson[1,6*]

[1]Department of Physics & Astronomy, Vanderbilt University, Nashville, TN
[2]Vanderbilt Eye Institute, Vanderbilt University, Nashville, TN
[3]Light Age, Inc., 500 Apgar Drive, Somerset, NJ
[4]Department of Molecular Physiology & Biophysics, Vanderbilt University, Nashville, TN
[5]Department of Biomedical Engineering, Vanderbilt University, Nashville, TN
[6]Vanderbilt Institute for Integrative Biosystem Research & Education, Nashville, TN

This work was published in Biomedical Optics Express, Vol. 2, Issue 5, pp. 1275-1281 (2011)

B.1 Overview

I worked on some of the experiments designed to measure the ablation characteristics of the RSA laser on cornea. I also worked on using optical coherence tomography to measure ablation depth in cornea.

B.2 Abstract

Prior work with free-electron lasers (FELs) showed that wavelengths in the 6- to 7-μm range could ablate soft tissues efficiently with little collateral damage; however, FELs proved too costly and too complex for widespread surgical use. Several alternative 6- to 7-μm laser systems have demonstrated the ability to cut soft tissues cleanly, but at rates that were much too low for surgical applications. Here, we present initial results with a Raman-shifted, pulsed alexandrite laser that is tunable from 6-7 μm and cuts soft tissues cleanly – approximately 15 μm of thermal damage surrounding ablation craters in cornea – and does so with volumetric ablation rates of 2-5×10^{-3} mm^3/s. These rates are comparable to those attained in prior successful surgical trials using the FEL for optic nerve sheath fenestration.

B.3 Introduction

Although lasers are in routine use across multiple medical specialties, no laser has yet made a widespread impact in precision neurosurgery. One candidate, mid-infrared (mid-IR) free-electron lasers (FELs), showed much promise and certainly can ablate soft biological tissues with high efficiency and remarkably little collateral damage [1-4]. In fact, work with the Vanderbilt FEL progressed to the successful completion of two FDA trials, encompassing eight human surgeries [5-7]. These surgeries – partial resection of intracranial tumors and fenestration of the optic nerve

in blind eyes scheduled for enucleation – were considered major successes; however, the cost, size and complexity of an FELs' accelerator technology all but eliminates FELs' potential for widespread surgical use.

Recognizing this limitation, researchers have developed and evaluated multiple alternative laser systems. Since the optimal wavelength for FEL ablation was 6.0, 6.1 or 6.45 μm (variable between tissue types and research groups) [1-4], the alternative laser systems have all targeted the 6- to 7-μm wavelength range. Initial trials with picosecond optical parametric oscillators (OPOs) [8] and with Sr vapor lasers [9] both proved unsuccessful because neither had sufficient energy to generate single-pulse, thermally confined ablation. More recent trials have demonstrated the ability to ablate soft tissues with little collateral damage. These include an Er:YAG-pumped OPO system [10] and a Nd:YLF-based system that generates mid-IR light using a combination of stimulated Raman scattering and difference frequency mixing [11]. As noted by Edwards et al, the limitation of these latter two systems is that "the average optical power will need to increase by about *two orders of magnitude* to achieve sufficient ablation rates for human surgery [11]." Here, we present a robust Raman-shifted alexandrite (RSA) laser system with tunable operation across the entire 6- to 7-μm wavelength range, and demonstrate its capability to ablate soft tissues with less than 15 μm of collateral damage while removing tissue at rates comparable to prior human surgeries [5-7].

B.4 Experiments

This RSA laser system consists of a tunable, Q-switched alexandrite laser (101-PAL™, Light Age Inc., Somerset, NJ) that pumps a two-stage Raman convertor (Figure B.1A) [12]. The fundamental output of the alexandrite laser is tuned to operate at wavelengths from 771–785 nm (ω_0 = 12740-

12970 cm^{-1}) and directly pumps a deuterium-filled Raman convertor. In this first convertor, fundamental output of the alexandrite laser interacts with the D-D stretching mode of the deuterium gas (Ω_{D2} = 2991 cm^{-1}) by the nonlinear process of stimulated Raman scattering. This double-pass Raman convertor is designed to optimize production of 1st order Stokes'-shifted output near 1.01 μm (the exact wavelength determined by the tuning of the alexandrite fundamental, $\omega_1 = \omega_0 - \Omega_{D2}$). This nominal 1.01-μm output in turn pumps a hydrogen-filled Raman convertor. In this second convertor, multiple passes are used so that stimulated Raman scattering from the hydrogen gas (Ω_{H2} = 4155 cm^{-1}) terminally produces 2nd order Stokes'-shifted output with a wavelength in the 6- to 7-μm range ($\omega_2 = \omega_1 - 2\Omega_{H2}$). Fig. 1A shows the wavelengths used at each stage to produce output at 6.10 and 6.45 μm, wavelengths corresponding to two strong absorption bands of soft tissues. Line spectra for each of these outputs are shown in Figure B.1B. In typical operation, the alexandrite laser produces 250-mJ fundamental pulses at 10 Hz that are first converted to ~50-mJ pulses of nominally 1.01-μm light and subsequently converted to 1- to 3-mJ pulses in the 6- to 7-μm wavelength range. The alexandrite laser is capable of generating higher pulse energies (> 400 mJ) and higher conversion efficiency can be attained with the deuterium convertor, but we limit the input to the multi-pass hydrogen convertor to avoid damaging its mirrors. Under optimal conditions, the RSA system used here has attained pulse energies up to 4 mJ at a wavelength of 6.1 μm. A second prototype RSA system has attained up to 9 mJ at 6.1 μm. During the nonlinear Raman conversion process, the 50-ns pulsewidth of the alexandrite laser is shortened to 10-20 ns while the spatial mode structure remains smooth and nearly Gaussian.

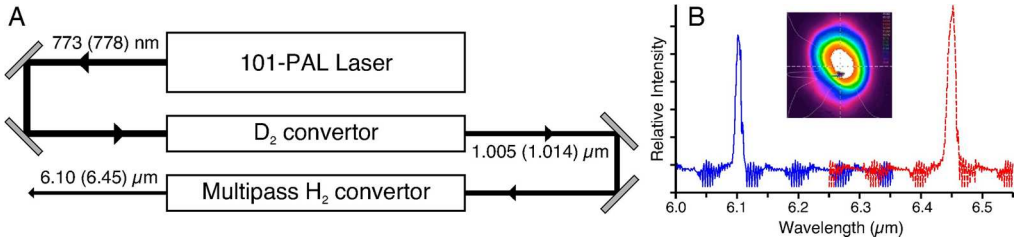

Figure B.1: Laser system schematic and characteristics. **(A)** A tunable alexandrite laser (PAL-101™) pumps a two-stage Raman converter. As examples, alexandrite laser output at 773 or 778 nm undergoes a 1st order Stokes' shift in the deuterium (D_2) convertor to yield 1.005- or 1.014-μm light. This output then undergoes a terminal 2nd order Stokes' shift in the multi-pass hydrogen (H_2) convertor to yield light at 6.10 or 6.45 μm. Tunable output anywhere from 6-7 μm is achieved by tuning the alexandrite laser from 771-785 nm. **(B)** Spectra of the laser system output when tuned to 6.1 μm (*solid, blue*) or 6.45 μm (*dashed, red*). The inset shows a nearly Gaussian beam profile obtained at 6.3 μm; similar profiles are obtained from 6-7 μm.

As shown in Figure B.1, the RSA consists of three modules: an alexandrite pump laser (101-PAL) that employs an oscillator-amplifier configuration; a deuterium convertor; and a hydrogen convertor (all from Light Age). To enhance conversion efficiency, the deuterium convertor is operated in a double-pass configuration and the hydrogen convertor is operated with a high number of passes. This multi-pass configuration is needed to achieve efficient conversion even with a relatively low Raman gain coefficient in the 6- to 7-μm wavelength region. The resonator and beam delivery system use kinematically mounted optical components, providing excellent long-term stability despite a very long optical path length. The laser wavelength is easily tuned via an externally mounted micrometer, and the alignment is fully maintained when scanning the wavelength over the operating range of 6-7 μm.

To ensure consistency in tissue ablation studies, we warm-up the laser for approximately one hour prior to our experiments, allowing all components to become thermally stabilized. After warm-up, we characterize the spatial profile of the beam with burn paper and monitor the time-dependent output with a fast photodiode. We also measure the output energy from the deuterium convertor and the multi-pass convertor using a thermopile-based power meter (30A-P,

Ophir-Spiricon Inc., Logan, UT) and a pyroelectric energy meter (J25, Coherent-Molectron Inc., Santa Clara, CA), respectively. Finally, we verify proper alignment through the multi-pass converter by means of an IR camera (Pyrocam III, Ophir-Spiricon)

For optimal performance of the current multi-pass convertor, the convertor is periodically baked, purged and refilled with hydrogen to eliminate residual water vapor that builds-up in concentration over time. Water vapor has very strong absorption in the 6- to 7-μm wavelength range and even very minute amounts have an observable effect on conversion efficiency – most prominently at mid-IR wavelengths corresponding to water vapor lines. We are developing new multi-pass convertor designs to minimize water vapor contamination. To maintain optimal performance, we also periodically refill the gas in the deuterium convertor.

B.5 Results and discussion

In typical daily operation at 1- to 3-mJ per pulse and with moderate focusing to spot diameters of 180-300 μm, the RSA laser system is capable of ablating soft tissues and soft tissue models at substantial rates. Figure B.2A shows an OCT (optical coherence tomography) image of nine partial thickness craters ablated in a gelatin model. Each crater was ablated using 160 pulses delivered at 10 Hz with a wavelength of 6.1 μm, pulse energy of 1.70 mJ and beam diameter of 300 μm (mean fluence of 0.60 J/cm^2). The average crater depth is 440 μm, corresponding to an average etch depth of 2.8 μm per pulse and an ablation rate of 28 μm/s (or 1.9×10^{-3} mm^3/s volumetrically). Since gelatin models may not fully capture all aspects of the laser-tissue interaction, Figure B.2B shows a similar OCT image after ablation of a goat cornea (still attached to an excised globe). In this case, just 40 pulses at slightly higher pulse energy – 1.85 mJ or a fluence of 0.65 J/cm^2 – ablated craters with an average depth of 163 μm, corresponding to an average etch depth of 4.1

μm per pulse and an ablation rate of 41 μm/s. These craters are not as wide as those in gelatin, so the volumetric ablation rate is only 1.8×10^{-3} mm^3/s. Figure B.2C then shows ablation rates for the RSA laser based on the time required to perforate tissue slices of varying thickness. With slightly tighter focusing (beam diameter of 180 μm), we reached fluences of 2-6 J/cm^2 that ablated cornea at 10-20 μm per pulse (an estimated $2.5\text{-}5.1 \times 10^{-3}$ mm^3/s volumetrically) and brain at 18 μm per pulse (an estimated 4.6×10^{-3} mm^3/s volumetrically). These results are summarized in Table B.1.

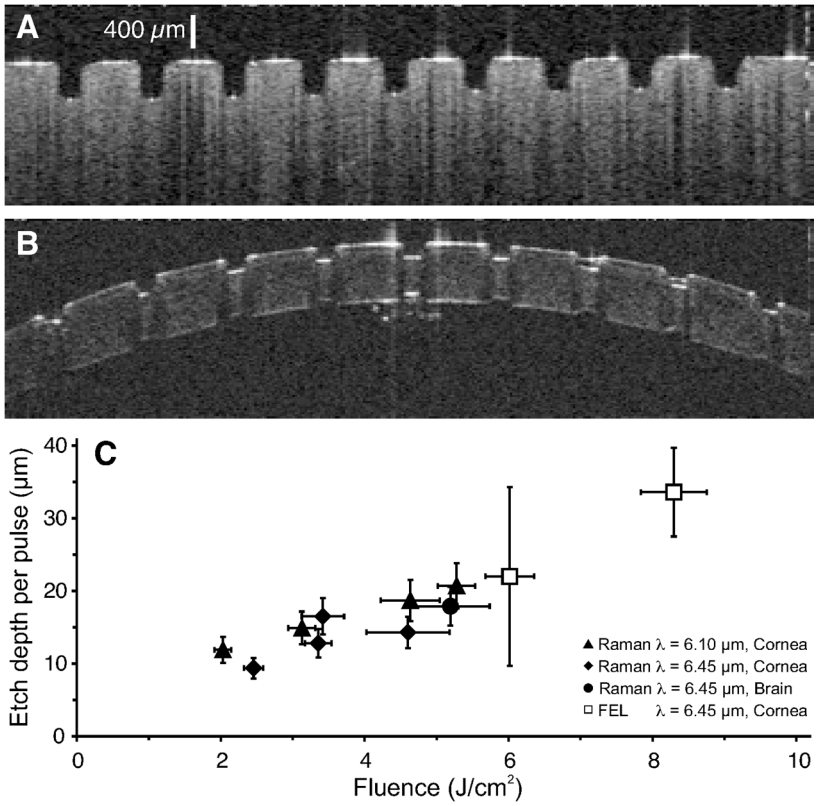

Figure B.2: Etch depths for partial and full thickness craters in soft tissues and soft tissue models. **(A)** OCT image of gelatin (10% wt/wt) ablated at λ = 6.1 μm with 160 pulses per crater (1.70 mJ/pulse at 10 Hz with a 300-μm beam diameter). The average depth of the craters is 440 μm with a standard deviation of ~5%. **(B)** OCT image of goat cornea ablated at λ = 6.1 μm with 40 pulses per crater (1.85 mJ/pulse at 10 Hz with a 300-μm beam diameter). The average depth of the craters is 163 μm. Note that the distortions along the inside surface of the cornea are OCT artifacts. The vertical scale bar applies to both images. **(C)** Mean etch depth per pulse achieved during full thickness ablations of porcine corneas (450- or 850-μm thick) or supported slices of freshly excised canine brain (1-mm thick) using λ = 6.1 or 6.45 μm with 0.5-1.3 mJ/pulse at 10 Hz. Two data points from FEL ablation of cornea are included for comparison.

These ablation rates should be compared to those achievable with other 6- to 7-μm laser sources and with the rates used in previous FEL-based surgeries. The Nd:YLF based system developed by Passat Inc. and Duke University was able to ablate fixed brain tissue at just over 1 μm per pulse [11]; however, the laser's low 0.5-Hz repetition rate yielded an average ablation rate of just 0.64 μm/s or 5.0 x 10^{-6} mm^3/s, volumetrically (based on the stated spot diameter of 100 μm). Edwards et al estimated that surgical relevance would be reached at ablation rates that were two orders of magnitude higher [11]. A 10× improvement in volumetric ablation rate was demonstrated by the Er:YAG-pumped OPO developed at Stanford (Table B.1) [10], but as shown here, the RSA laser is the first FEL alternative in the 6- to 7-μm wavelength range to achieve ablation rates with potential surgical relevance – due to a 400-1000× improvement in the volumetric ablation rate. The volumetric ablation rate is the one that needs to be compared to surgical procedures that require anything besides the drilling of a single small hole. For example, in optic nerve sheath fenestration, a window is cut in the optic nerve sheath by scanning the beam to make an incision along the circumference of a circle (diameter 2-3 mm) that completely incises the sheath (thickness 150-250 μm, depending on species). The unattached circle of nerve sheath is then removed manually. When this procedure was performed using the FEL, the beam diameter was approximately 200 μm and the lasing was completed in 2-3 minutes, so that the average volumetric ablation rate was 1-4 $\times 10^{-3}$ mm^3/s [3, 7, 13]. The present RSA laser can achieve this volumetric ablation rate with free-beam delivery, but may fall just short when fiber-coupling losses are included (as necessary for endoscopic delivery of the beam behind the eye [14, 15]). The other procedure for which FDA trials were conducted with the FEL was partial excision of intracranial tumors. This procedure used higher fluences and ablated tumors at impressively high rates up to 2.0×10^{-2} mm^3/s [5] – placing it just out of reach (factor of ~ 4) of what we have thus far attained using free-beam delivery of the RSA laser.

Table B.1: Ablation characteristics of pulsed laser systems operating in the 6- to 7-μm wavelength range.

Laser	λ μm	E mJ	w μm	f Hz	Tissue	δ μm	$d\delta/dt$ μm/s	dV/dt mm^3/s
RS-DFM-Nd:YLF [11]	6.45	< 2	100	0.5	brain	1.3	0.64	5.0×10^{-6}
Er:YAG / OPO [10]	6.10 6.45	<0.25	60	5	cornea	3.8-4.4	19-22	5.4×10^{-5} 6.2×10^{-5}
RSA	6.10	1.7	300	10	gelatin	2.8	28	1.9×10^{-3}
	6.10	1.85	300	10	cornea	4.1	41	2.9×10^{-3}
	6.10 6.45	0.5-1.3	180	10	cornea	10-20	100-200	2.5×10^{-3} 5.1×10^{-3}
	6.45	1.3	180	10	brain	18	180	4.6×10^{-3}

λ = wavelength, E = pulse energy, w = spot diameter, f = pulse repetition rate, δ = mean etch depth per pulse, $d\delta/dt$ = linear ablation rate and dV/dt = volumetric ablation rate

Improving the ablation rate would be moot if the RSA laser left behind excessive collateral damage, but initial histology of cornea, heart, skin and kidney ablated with the RSA laser shows that ablation is accompanied by only a very thin layer of thermally damaged tissue (Figure B.3). This damaged layer is clearest in cornea, where it is on average 15-μm thick. In the other tissues, the damaged layer is thinner and in some cases not even measureable (e.g. heart or kidney in Fig. 3B,D). These ablations were conducted either with free beam delivery of the laser (Figure B.3A) or with delivery via a hollow-glass waveguide and handheld probe (Figure B.3B-D) [16]. In the case of fiber optic delivery, we currently have transmission losses of ~67% and could only deliver 0.6 mJ/pulse onto the tissue surface; however, this pulse energy is still sufficient to ablate these soft tissues with a single manual pass of the beam (beam diameter approximately 200 μm). We have also used the RSA laser to ablate soft tissues such as retina and optic nerve sheath, for which there are established endoscopic laser procedures [15]. These initial results are promising and will be discussed in depth in subsequent publications.

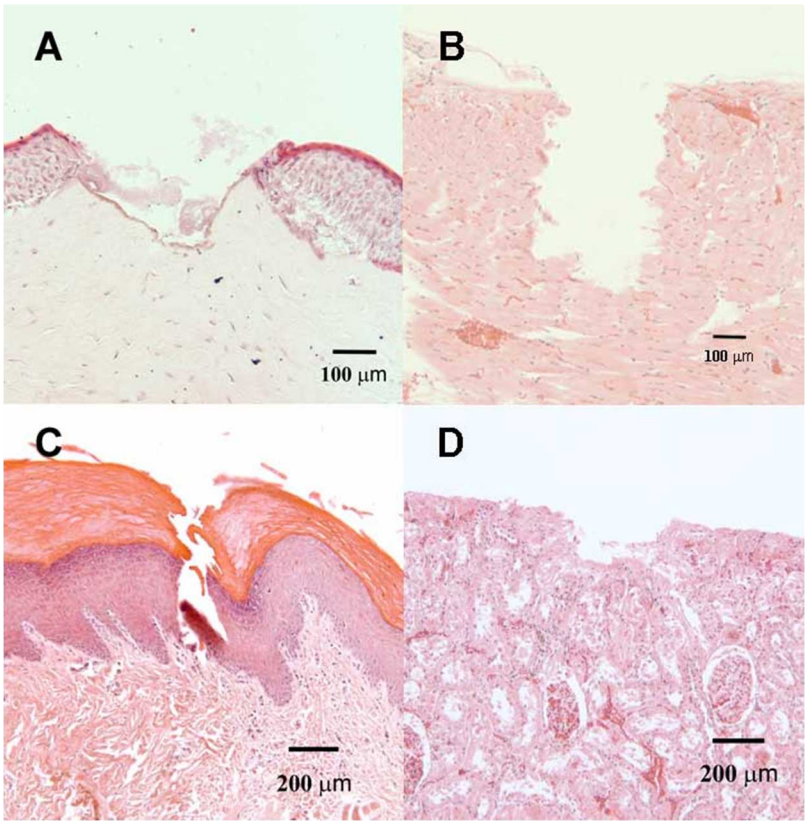

Figure B.3: Histology using H&E stain after RSA laser ablation of excised soft tissues: **(A)** goat cornea, **(B)** rat heart, **(C)** rat skin and **(D)** rat kidney. All ablations were performed at a wavelength of 6.1 μm and a pulse repetition rate of 10 Hz. For (A), the laser was focused onto the cornea surface through air, delivering ~1.9 mJ/pulse to ablate a series of overlapping 10-pulse craters. For (B-D), the laser was delivered through a hollow glass waveguide and handheld probe. This limited delivery to 0.6 mJ/pulse, but allowed the user to manually scan the beam across the tissues as in an actual surgical procedure. Thermal damage is most evident in cornea as the darker region along the crater edge, which is 15-μm thick on average. In the other tissues, thermal damage ranges from minimal to not measureable.

Thus, the RSA laser described here generates pulsed output in the 6- to 7-μm wavelength range that can ablate soft tissues at rates that approach surgical relevance – depending on the chosen procedure and whether endoscopic delivery is necessary. These ablation rates were obtained with typical output pulse energy at multiple times during the laser's first two years of operation. Just as importantly, the incisions produced by this laser are accompanied by very thin regions (< 15 μm) of thermal collateral damage. This combination of robust operation, ablation rates above 10^{-3} mm^3/s and thin regions of collateral damage places the RSA laser in a unique niche with potential

applicability in delicate ophthalmic and neurosurgical applications. This potential should only improve with future increases in pulse energy, repetition rate and fiber-optic coupling efficiency – areas in which development is currently in progress. We are also developing automated control of wavelength and operational settings. Collectively, these system enhancements will yield a laser system that is potentially attractive for use in a variety of surgical applications.

B.6 Acknowledgements

This work supported by: NIH SBIR 2R44RR024070-02A1; Department of Defense STTR W81XWH-08-C-0109; NIH 1R21EY019752-01; NIH Core Grant 2P30EY008126-22; unrestricted departmental grant from Research to Prevent Blindness, Inc., NY; and the Joseph Ellis Family Research Fund.

B.7 References

[1] G. Edwards, R. Logan, M. Copeland, L. Reinisch, J. Davidson, B. Johnson, R. Maciunas, M. Mendenhall, R. Ossoff, J. Tribble, J. Werkhaven, and D. O'Day, Nature **371**, 416-419 (1994).
[2] J. I. Youn, P. Sweet, G. M. Peavy, and V. Venugopalan, Lasers Surg. Med. **38**, 218-228 (2006).
[3] K. M. Joos, L. A. Mawn, J. H. Shen, E. D. Jansen, and V. A. Casagrande, Proc. SPIE-Int. Soc. Opt. Eng. **4611**, 81-85 (2002).
[4] R. A. Hill, Q. Ren, D. C. Nguyen, L. H. Liaw, and M. W. Berns, Lasers in Medical Science **13**, 219-226 (1998).
[5] G. S. Edwards, R. H. Austin, F. E. Carroll, M. L. Copeland, M. E. Couprie, W. E. Gabella, R. F. Haglund, B. A. Hooper, M. S. Hutson, E. D. Jansen, K. M. Joos, D. P. Kiehart, I. Lindau, J. Miao, H. S. Pratisto, J. H. Shen, Y. Tokutake, A. F. G. van der Meer, and A. Xie, Rev. Sci. Instrum. **74**, 3207-3245 (2003).
[6] M. L. Copeland, R. J. Maciunas, and G. S. Edwards, *Neurosurgical Topics: Advanced Techniques in Central Nervous System Metastases*, R. J. Maciunas, ed. (The American Association of Neurological Surgeons, Park Ridge, IL, 1998).
[7] K. M. Joos, L. A. Mawn, J. H. Shen, E. D. Jansen, R. D. Robinson, M. A. Mackanos, J. A. Mavity-Hudson, and V. A. Casagrande, Invest. Ophthalmol. Vis. Sci. **45**, E-Abstract 45 (2004).
[8] G. Edwards, M. S. Hutson, S. Hauger, J. Kozub, J. Shen, C. Shieh, K. Topadze, and K. A. Joos, Proceedings of SPIE **4633**, 194-200 (2002).
[9] M. A. Mackanos, B. Ivanov, A. N. Soldatov, I. Kostadinov, M. H. Mendenhall, D. W. Piston, R. F. Haglund, and E. D. Jansen, Proc. SPIE-Int. Soc. Opt. Eng. **5319**, 201-208 (2003).
[10] M. A. Mackanos, D. Simanovskii, K. M. Joos, H. A. Schwettman, and E. D. Jansen, Lasers Surg. Med. **39**, 230-236 (2007).

[11] G. S. Edwards, R. D. Pearlstein, M. L. Copeland, M. S. Hutson, A. Latone, A. Spiro, and G. Pasmanik, Opt. Lett. **32**, 1426-1428 (2007).
[12] S. Wada, H. Tashiro, Y. Urata, L. Thi Thi, A. Kasai, and K. Toyoda, Appl. Phys. B **57**, 435-439 (1993).
[13] K. M. Joos, L. A. Mawn, J. H. Shen, and V. A. Casagrande, Lasers Surg. Med. **32**, 32-41 (2003).
[14] K. M. Joos, R. J. Shah, R. D. Robinson, and J. H. Shen, Lasers Surg. Med. **38**, 846-851 (2006).
[15] R. J. Shah, J. H. Shen, and K. M. Joos, Lasers Surg. Med. **39**, 589-596 (2007).
[16] J. H. Shen, J. A. Harrington, G. S. Edwards, and K. M. Joos, Appl. Opt. **40**, 583-587 (2001).